DISCRETE ELEMENT ANALYSIS OF THE MECHANICAL RESPONSE OF BOLTED STEEL MESH SUPPORTING UNSTABLE ROCK ON STEEP SLOPES

by

Cong Xu

M.Eng., China University of Geosciences, 2015

B.Eng., China University of Geosciences, 2012

A THESIS SUBMITTED IN PARTIAL FULFILLMENT OF

THE REQUIREMENTS FOR THE DEGREE OF

DOCTOR OF PHILOSOPHY

in

THE COLLEGE OF GRADUATE STUDIES

(Civil Engineering)

THE UNIVERSITY OF BRITISH COLUMBIA

(Okanagan)

Feburary 2020

The following individuals certify that they have read, and recommend to the College of Graduate Studies for acceptance, the dissertation entitled:

DISCRETE ELEMENT ANALYSIS OF THE MECHANICAL RESPONSE OF BOLTED STEEL MESH SUPPORTING UNSTABLE ROCK ON STEEP SLOPES

submitted by Cong Xu in partial fulfillment of the requirements for

the degree of Doctor of Philosophy

in Civil Engineering

Examining Committee:

Dr. Dwayne D. Tannant, School of Engineering, The University of British Columbia
Supervisor

Dr. Shahria Alam, School of Engineering, The University of British Columbia
Supervisory Committee Member

Dr. Ahmad Rteil, School of Engineering, The University of British Columbia
Supervisory Committee Member

Dr. Kevin Golovin, School of Engineering, The University of British Columbia
University Examiner

Dr. John Hadjigeorgiou, Department of Civil & Mineral Engineering, University of Toronto
External Examiner

Abstract

Steel wire mesh pinned by a pattern of bolts with plates is widely used in rock slope stabilization. The bolted steel mesh can hold potentially unstable rocks in place. Typical laboratory tests on steel mesh use rigid frames to fix the mesh perimeters. However, the steel mesh is usually pinned by bolts in the field. Different configurations of bolts will affect how the mesh behaves.

This research aims to develop numerical models to understand the behaviour of bolted steel mesh. Instead of using expensive and time-consuming experimental and field tests, this research takes advantage of the existing experimental results to calibrate steel mesh models using the open-source discrete element method (DEM) code YADE. Several modelling approaches were compared in terms of their mechanical response and computational cost. The particle-based mesh model was finally chosen because this approach can capture the mechanical response of steel mesh with less computational demand.

The influence of different bolt patterns and bolt spacing on the force-displacement response of steel wire mesh was analyzed using a calibrated mesh model. Relationships between the resistance force provided by the mesh and the bolt density at various mesh deformations were developed. A parametric study investigated various factors that affect the mesh behaviour under loads created by an unstable rock using DEM. The results provide a better understanding of the steel mesh response for various bolt arrangements and loading conditions, which can help engineers choose the proper bolt patterns to control the mesh deformation.

The simulation results were used to develop prediction models using the support vector machine (SVM) approach. The prediction models can be used to estimate the performance for bolted steel mesh. Finally, this research analyzed the interaction of the bolted mesh with a sliding and a toppling rock. The results revealed the load transfer and displacement between the rock, mesh and rockbolt plates. The research findings were demonstrated in a design of bolted mesh for a steep rock cut that was experiencing failures.

Lay Summary

Using steel mesh pinned by bolts is popular in rock slope stabilization. Typical laboratory tests on steel mesh do not capture the real mesh behaviour in the field. This research improves the understanding of the behaviour of mesh pinned by rockbolts. Experimental tests are expensive and time-consuming. Thus, an open-source computer program was used to conduct numerical simulations. The results reveal the load and displacement behaviour of steel mesh with bolts. Design curves were developed to help choose a bolt layout to make the mesh more efficient. This research also developed a prediction tool using the machine learning technique. The tool can predict the mesh's load-displacement behaviour when loaded by an unstable rock. Finally, this work presents a case study that applied the research findings to the design of bolted mesh for a steep rock cut.

Preface

All the presented research work was conducted under the supervision of Dr. Dwayne D. Tannant in the School of Engineering at the University of British Columbia's Okanagan campus.

This dissertation is based on my work [J1, J2, C1, C2], for which I was the principal investigator under the supervision of Dr. Dwayne D. Tannant. I was responsible for conducting numerical simulations, writing manuscripts and revisions. Dr. Wenbo Zheng helped revise the content in [J1, J2]. Dr. Kaiyun Liu helped revise the content in [J1].

Chapter 3 contains the work from one journal article [J2] and one conference paper [C2]. Chapter 4 involves the work from one journal article [J2]. Chapter 5 includes the work from one journal article [J1]. Chapter 6 contains the work from one conference paper [C1].

Ethics approval from the UBC Research Ethics Board was not required. The publications related to this research are listed below:

Refereed Journal Articles

[J1] Xu, C., Tannant, D.D., Zheng, W., and Liu, K. 2020. Discrete element method and support vector machine applied to the analysis of steel mesh pinned by rockbolts. International Journal of Rock Mechanics and Mining Sciences. doi:10.1016/j.ijrmms.2019.104163

[J2] Xu, C., Tannant, D.D., and Zheng, W. 2019. Discrete element analysis of the influence of bolt pattern and spacing on the force-displacement response of bolted steel mesh. International Journal for Numerical and Analytical Methods in Geomechanics, **43**(12): 2106–2125. doi:10.1002/nag.2974.

Refereed Conference Proceedings

[C1] Xu, C., and Tannant, D.D. 2018. Investigation of bolted steel mesh to support a sliding rock block using DEM. *In* CIM Convention 2018. Vancouver, Canada. p. 9.

[C2] Xu, C., and Tannant, D.D. 2016. Discrete element modelling of steel wire mesh and rockbolt plate. *In* Proceedings of the 8th International Symposium on Ground Support in Mining and Underground Construction. Luleå University of Technology, Luleå, Sweden. p. 14.

Table of Contents

List of Tables

List of Figures

List of Abbreviations

DEM	Discrete element method
FEM	Finite element method
H	Horizontal bolt spacing
LF	Linear kernel function
PF	Polynomial kernel function
RBF	Radial basis function
SDWM	Stochastically distorted wire model
SVM	Support vector machine
UAV	Unmanned Aerial Vehicle
V	Vertical bolt spacing
YADE	Yet Another Dynamic Engine

Acknowledgements

I wish to express my sincere gratitude to my supervisor Dr. Dwayne D. Tannant. His guidance, support and insight help me overcome difficulties and accomplish my research. I can always be inspired when working with him. His clarity in thinking, professional integrity, and open mind will continue to influence me in my life.

I am deeply grateful to my research committee members, Dr. Shahria Alam and Dr. Ahmad Rteil, for their encouragement and insightful comments on my research. I wish to thank Dr. John Hadjigeorgiou and Dr. Kevin Golovin for being the examiners in my defence. Thanks are owed to the faculty and staff at the School of Engineering for supporting my PhD study. I am also thankful to Mr. Andy Buechi from GeoBrugg for providing steel mesh samples and insightful advice on my research.

I am sincerely thankful to Dr. Xinli Hu, Dr. Peng Zhang and Dr. Kaiyun Liu for their encouragement and guidance on my research. I would like to thank Dr. Wenbo Zheng for his assistance in the research and friendship in daily life. I wish to thank my research group, Dr. Samuel Nunoo, Josephine Morgenroth, Umair Asghar, Kalie Smith, Hamid Daghigh, Christian Desjarlais, David Scott and visiting students and scholars for sharing their expertise with me. I am grateful to my colleagues and friends in UBC, Xian Jin, Zhenlin Tian, Kai Zhang, Jiaming Shi, Xuan Gao, and Zongjie Wang for sharing this wonderful journey.

Special thanks to my dear wife, Yuxin Yang, for her love, accompanying and support during my PhD adventure. I am deeply thankful to my parents, my parents-in-law, my grandpa and grandma, and my family for their understanding, patience and encouragement over all these years.

Dedication

To my loving wife, Yuxin.

Chapter 1: Introduction

1.1 Background and motivation

The failure of rock slopes is a common slope hazard along highways and railways, as well as in civil and mining engineering in mountainous areas. Steel wire mesh has been widely used in rock slope stabilization (Shu et al. 2005b, Giacomini et al. 2012, Justo et al. 2014). The mesh can function as a drapery, whereby its purpose is to deflect the trajectories of rockfalls (Giacomini et al. 2012). When the wire mesh is bolted to the rock surface, as shown in Figure 1.1, it is usually designed to hold potentially unstable rock blocks in place (Blanco-Fernandez et al. 2013).

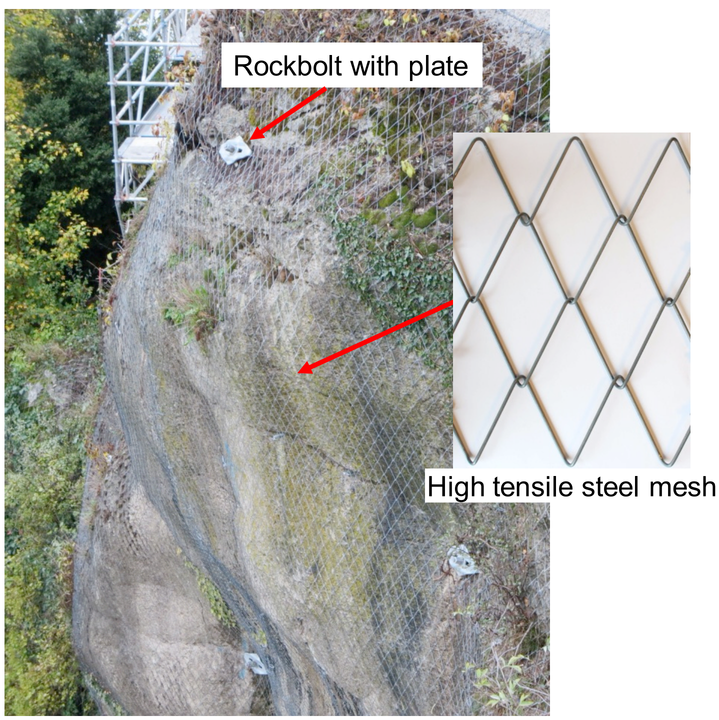

Figure 1.1 Bolted steel wire mesh

Although bolted steel mesh support systems are common, only a few design methods for their use can be found in the literature. The current design methods for bolted steel mesh are based on methods that work best for uniform loading associated with soil slopes (Blanco-Fernandez et al. 2011). These methods rely on limit equilibrium analysis, and the slopes are simplified using vertical slices or several wedges in a shallow layer below the ground surface. One assumption in these methods is that the steel mesh exerts a normal and a shear force/pressure on the slope surface (Da Costa and Sagaseta 2010, Cala et al. 2012, Justo et al. 2014). In order to create these forces/pressures, the steel wire mesh needs to be pre-stressed during the installation of the bolts. However, it is difficult to achieve the proper pretension in the steel mesh in practice, and the tensile forces mobilized in the wires are typically much less than the tensile strength (Blanco-Fernandez et al. 2013).

In terms of rock slopes, the simplification in the current design methods may not be suitable for structurally controlled failure modes such as plane sliding, wedge sliding, and block toppling, which are common for rock slopes (Hoek and Bray 1981, Wyllie and Mah 2004). Unstable rock blocks can move and deform the steel mesh. Mesh deformations can generate complex distributions of tensile forces in the wires, and wires can rupture. The current design methods do not consider mesh deformations and the distribution of tensile forces in the wires. A better design approach must limit the mesh deformations rather than using the ultimate load capacity of the mesh. The reason is that mesh can sustain a large amount of deformation when it reaches its ultimate load capacity. Large mesh deformations may not be acceptable when there is limited space between rock slope and buildings or infrastructure.

The force-displacement response of the steel mesh can be used to estimate the support forces of steel mesh on the unstable rock blocks (Grimod and Giacchetti 2014). Rigid frames are often used to fix the outer boundaries of the steel mesh during laboratory tests to obtain the force-displacement relationship of steel mesh (Bertrand et al. 2008, Castro-Fresno et al. 2008, 2009, Cala et al. 2012, Gobbin et al. 2017). In 2016, a testing standard (ISO 17746) was developed to guide punch tests. However, the fixed outer boundary on a steel mesh is not a realistic boundary condition to represent field loading conditions. In the field, the steel mesh is usually anchored using bolts with two different patterns, pattern A and pattern B, as shown in Figure 1.2. In pattern A, the bolts are aligned with each other in rows and columns. In pattern B, the bolts in alternating rows are offset one half of the separation distance between the bolts. Field tests showed that the steel mesh is more deformable under real flexible boundary conditions compared to laboratory tests in a test frame (Bertolo et al. 2009). Thus, it is necessary to consider the real force-displacement response of steel mesh when designing a bolted steel mesh support system. An ideal bolt arrangement will improve the effectiveness of steel mesh by helping the steel mesh mobilize a resisting load at smaller deformations. Nevertheless, many factors can affect the force-displacement response of steel mesh, which limits the application of this design method.

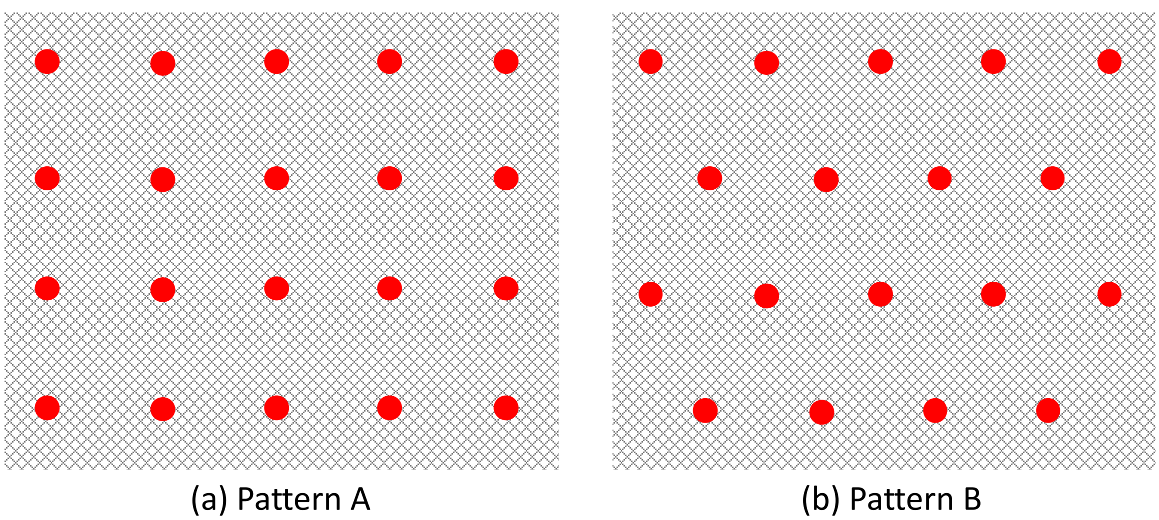

Figure 1.2 Bolt patterns A and B

An alternative approach of expensive physical experiments is to use numerical modelling to investigate different configurations and boundary conditions of bolted steel mesh. While many researchers applied the finite element method (FEM) to model the steel mesh (Sasiharan et al. 2006, Roth and Ranta-Korpi 2007, Castro-Fresno et al. 2008, del Coz Díaz et al. 2009, Gentilini et al. 2013, Escallon et al. 2015), the FEM needs specific algorithms to deal with large deformations and failure of the steel mesh (Bertrand et al. 2012). Although the discrete element method (DEM) is also computationally intensive, the DEM can simulate the motion and large displacements between elements without extra algorithms, making it more intuitive to deal with problems like rock moving and interacting with steel mesh (Xu and Tannant 2018). The double-twisted hexagonal mesh was modelled by placing a particle (ball) at each node and introduced a virtual spring between two particles to capture the tensile behaviour of one steel wire (Nicot et al. 2007, Bertrand et al. 2008, Li and Zhao 2018). Thoeni et al. (2013) improved this approach by adding a more complex stochastic interaction between particles that represented the distorted wires in the mesh. They implemented this method into an open-source DEM code YADE (Šmilauer et al. 2015). Dynamic tests showed that this kind of model can simulate the behaviour of wire mesh and was successfully used to model a drapery system for rockfall protection (Thoeni et al. 2014, 2015) and applied in a reliability-based design for rockfall fences (Bourrier et al. 2015). Cylinder elements were first introduced by Bourrier et al. (2013) and were used to simulate wires in a mesh (Xu and Tannant 2016, Effeindzourou et al. 2017). The cylinder elements are a beam-like element in YADE that can handle tension, bending, and twisting (Effeindzourou et al. 2016). Compared with cylinder elements, the use of particle elements results in a steel mesh model that ignores wire bending.

Combinations of numerical simulations of wire mesh with mathematical optimization methods have been used to analyze the response of rockfall protection for both design and hazard reduction purposes (Bourrier et al. 2015, Toe et al. 2018). This approach can generate metamodels that statistically capture the complex structural response considering various influence factors in a computationally cost-effective way. Some examples used in geotechnical engineering include the response surface method (RSM) (Mollon et al. 2011, Shamekhi and Tannant 2015, Blanco-Fernandez et al. 2016), artificial neural networks (ANN) (Lu and Rosenbaum 2003, Cho 2009), and the support vector machine (SVM) (Zhao 2008, Toe et al. 2018, Liu et al. 2019). The SVM approach (Vapnik 2000) overcomes the limitations of RSM because it can cope with problems beyond nonlinear concave or convex surfaces. The SVM has a regulation parameter to avoid overfitting and finds out the global optimum, which overcomes the limitations of ANN. Toe et al. (2018) used an SVM approach to assess the effectiveness of rockfall barriers for various impact conditions. The success of the support vector machine approach for the study on rockfall barriers motivated the current work with the bolted wire mesh.

1.2 Research objectives

This research aims to develop numerical models to understand the behaviour of bolted steel mesh used to support steep unstable rock slopes. The objectives of this research are to (1) develop numerical models to capture the mechanical response of steel mesh in the laboratory tests, (2) understand the force and displacement relationship of steel mesh with various bolt patterns and spacing, (3) demonstrate the performance of bolted steel mesh when resisting an unstable rock.

1.3 Contribution

This research creates numerical models to demonstrate the response of bolted steel mesh with various bolt arrangements when the mesh is subject to loads from an unstable rock. The developed numerical models using DEM captures the mechanical characteristics of the physical steel mesh. The outcomes from extensive numerical simulations on the interaction of bolted steel mesh and rock block contribute to a better understanding of the mesh behaviour. These results have significant implications for improving the effectiveness of mesh on rock slopes using a proper bolt arrangement.

1.4 Methodology

To achieve the research objectives, extensive numerical simulations were performed on the steel mesh that was subjected to a pseudo-static loading. The tasks and corresponding methodologies in the research are presented as follows.

- The first task was to determine an efficient modelling approach to simulate high-tensile steel mesh. Published results of laboratory tests on high-tensile steel mesh (TECCO G65/3) were collected. Different models for high-tensile steel mesh were developed in the open-source DEM code YADE using particle elements and cylinder elements. Numerical punch tests were performed to compare the force-displacement response and computational cost of these models. The particle-based mesh model was calibrated to match the mesh response under laboratory tensile test and punch test.

- The second task was to analyze the influence of bolt patterns and bolt spacing on the force-displacement relationship of wire mesh. The calibrated mesh model was applied to perform the punch tests on the wire mesh pinned by two commonly used patterns of bolts. This research conducted a series of numerical simulations by varying the horizontal and vertical bolt spacing on the wire mesh. The influences of different bolt patterns and varying ratios of bolt spacing on the effectiveness of steel wire mesh were analyzed.

- The third task was to investigate the displacement and load transfer mechanism of bolted steel mesh when resisting an unstable rock. Discrete element models were created to simulate realistic field scenarios where an unstable rock interacts with the bolted steel mesh. A parametric study was conducted based on DEM simulations. The influence of the factors that affect mesh performance was analyzed.

- The fourth task was to develop a tool to predict mesh performance. A support vector machine was trained to predict the mesh responses using the results from DEM simulations. Three widely used SVM kernel functions were compared. The prediction performances of the obtained SVM models were analyzed.

1.5 Thesis structure

Chapter 1 presents the research background and motivation. The research progress and challenges are described for the bolted steel mesh for slope stabilization. The research objectives and methodologies are also presented.

Chapter 2 presents a literature review on the bolted steel wire mesh for slope stabilization. This chapter summarizes and discusses various rock slope failure mechanisms, experimental and numerical tests on the steel wire mesh and the applications that integrate the mathematical and numerical methods in civil engineering.

Chapter 3 presents the discrete element modelling of high-tensile steel mesh. This chapter compares various modelling approaches for steel mesh in terms of force-displacement response and effectiveness using open-source DEM code YADE. The calibration and validation of the mesh model using the published results of laboratory tensile and punch tests on the wire mesh is discussed.

Chapter 4 presents the influence of bolt pattern and spacing on the behaviour of bolted steel mesh. This chapter compares the force-displacement response of steel mesh pinned different bolt arrangements using numerical simulations. Relationships between the resistance force of steel mesh and bolt density at various mesh deformations are developed.

Chapter 5 presents the use of DEM and SVM to analyze the rock-bolted steel mesh response. Discrete element models are created to simulate realistic field scenarios where an unstable rock interacts with the bolted steel mesh. A parametric study on the factors that affect mesh performance is conducted based on DEM simulations. A tool is developed to predict bolted mesh response on rock slopes.

Chapter 6 presents an investigation on the bolted steel mesh to support a sliding rock and a topping rock. The rock block is simulated by particle elements that are clumped together. The slope face is modelled by triangular facet elements. The calibrated steel mesh model is used to hold the rock block. The effectiveness of the bolted steel mesh and load transfer between the rock, mesh, and bolts is studied.

Chapter 7 presents a case study that shows a design of bolted steel mesh to hold an overhanging rock slope. The design utilizes the research outcomes from previous chapters.

Chapter 8 summaries the research outcomes and discusses the limitations and recommendations for future work.

Chapter 2: Literature review

2.1 Failure of rock slopes

The failure of rock slopes is common in mountainous regions. The rock slopes can be categorized as natural rock slopes and artificial rock slopes. The natural rock slopes are the products of nature, while the artificial rock slopes are created by excavations to make room for transportation, buildings, dams and portals (Goodman and Kieffer 2002). Many factors may cause a rock slope failure, such as weathering, groundwater, rainfall, freeze-thaw cycles, earthquake, and excavations (Frayssines and Hantz 2006, Amini et al. 2009, Zhang et al. 2016). The classical failure mechanisms of rock slopes are planar, wedge, and toppling failures (Hoek and Bray 1981, Wyllie and Mah 2004).

A block of rock can slide as a planar on a single joint dipping out of the slope face (Wyllie and Mah 2004). Unstable rock blocks can also slide on several slip faces, which form a stepped-path failure mechanism (Brideau et al. 2009, Scholtès and Donzé 2015, Tannant et al. 2017). When two joints form a rock wedge, and the intersection of the two joints daylights the slope, a wedge failure may occur (Jiang et al. 2013, Paronuzzi et al. 2016). The wedge failure mechanism can be seen on a much wider range of geological and geometric conditions in the field than the plane failure. A toppling failure of rock slope involves the overturning of rock columns about their fixed bases. Different types of toppling failure, such as block toppling, flexural toppling, and block-flexural toppling, may occur depending on the rock types and development of joints in the rock masses (Liu et al. 2010, Majdi and Amini 2011, Amini et al. 2012). The toppling failure mechanism is more significant on steep slopes than the planar and wedge failure (Goodman and Kieffer 2002).

In the field, it is expected to see more complex failure mechanisms of rock slopes because of the differences in rock types, the discontinuities within the rock masses, and the environments where the rock slopes are. The sliding and toppling failure of rock blocks in a rock slope may happen one after another or at the same time. When the thoroughgoing discontinuities parallel the rock slope surface, a buckling failure of the rock slabs may occur near the toe of the slopes (Cavers 1981, Qin et al. 2001). A ravelling failure can occur if the rock slope is highly weathered or fractured (Goodman and Kieffer 2002). The collapse of overhanging rocks is another common failure mode on steep rock slopes (Makedon and Chatzigogos 2012, Huang et al. 2017). The overhanging rocks are usually caused by erosion in the weaker layers in the rock masses or excavations (Paronuzzi and Serafini 2009, Zhang et al. 2016). The development of the notch at the base of the rocks gradually affects the stability of the rocks, and both toppling and sliding failure may occur. The rock collapse caused by the notch at the base is also commonly seen on coastal cliffs (Matsukura 2001, Muller et al. 2006, Kogure and Matsukura 2010).

2.2 Current design methods for bolted steel mesh

The failure of rock slopes near highways, railways, and buildings may damage this infrastructure and threaten human lives. A bolted steel mesh system is one of the rock slope protection measures to prevent potential rock failures and retain the failed rocks at their original positions. Most bolted mesh design methods were developed for soil slopes. Only two design methods were found specifically for rock slopes. This section summarizes the available design methods for both soil and rock slopes. The design methods described in this section are for the dry slope condition to demonstrate the basic design ideas. The actual design methods can consider other slope conditions, such as groundwater and earthquake.

2.2.1 Design methods for soil slopes

2.2.1.1 Infinite soil slope

One design method is for stabilizing an infinite soil slope (Da Costa and Sagaseta 2010). The slope is considered as an infinite slope if the ratio between the slope thickness and slope height is small. The method assumes that the soil slides along a plane that is parallel to the slope surface. The method divides the slope into several vertical soil slices, as shown in Figure 2.1. The forces at the upstream and downstream sides of the soil slice are assumed to be equal; thus, they are not considered. A limit equilibrium analysis is performed for each soil slice based on the Mohr-Coulomb failure criterion at the sliding plane. This method assumes that the support of the bolted steel mesh is equivalent to a normal stress p and a shear stress t. The relationship between p and t can be expressed as $t = p \cdot \tan\delta$. The δ is the interface friction angle between the soil surface and mesh. The p can be obtained by solving the force equilibrium equations for the soil slice. The values of p and t can be used to choose a proper mesh type to stabilize the slope.

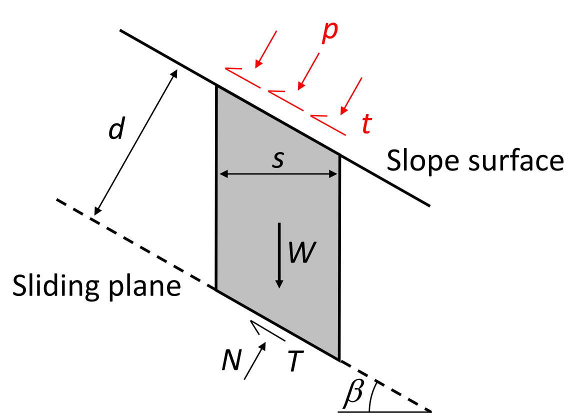

Figure 2.1 Force equilibrium on a soil slice in an infinite slope

2.2.1.2 Finite soil slope, method A

Another design method is for the finite soil slopes proposed by Da Costa and Sagaseta (2010). A slope can be considered as finite if the ratio between the thickness of the unstable layer and the slope height is not small enough. This method divides the unstable layer into several wedges, as shown in Figure 2.2a. The size of the wedges depends on the bolt spacing on the slope. The reaction of the mesh is assumed as a normal pressure p acting on each wedge.

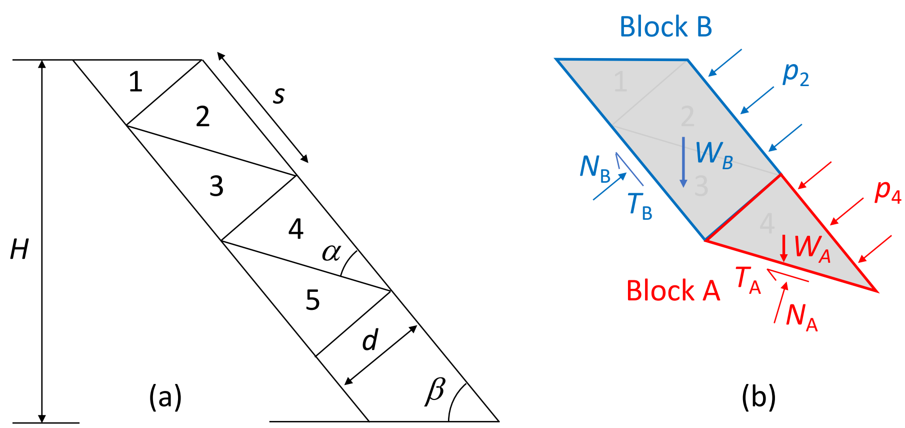

Figure 2.2 (a) Slope discretized into wedges and (b) force equilibrium on wedges

A series of limit equilibrium analysis is performed on every wedge from the crest to the toe in the slope. In every calculation step, two blocks are involved in the analysis: a lower block A sliding along an angle of α and an upper block B sliding on a plane that is parallel with the slope surface. For example, in Figure 2.2b, block A is wedge 4, and block B consists of wedge 1 to 3. The normal pressure on block B is already known from previous calculation steps, which is p_2. Therefore, the value of the normal pressure p_4 can be obtained by the limit equilibrium analysis on block A and block B based on the Mohr-Coulomb failure criterion at the sliding planes. The calculated maximum normal pressure is suggested in the design as the support from the mesh.

2.2.1.3 Finite soil slope, method B

The third design method (IberoTalud and Universidad de Cantabria 2005) is also applied to the slope with a finite height. The method divides the unstable layer into an upper block and a lower wedge, as shown in Figure 2.3. The method assumes that the effect of the mesh is equivalent to a normal pressure *p* and a shear pressure *t*. Different from the design method for infinite soil slopes, the value of *t* is unknown. The Mohr-Coulomb failure criterion at the sliding planes is applied in the limit equilibrium analysis on the two blocks. The value of *p* is calculated by solving the force equilibrium equations, and *p* is a function of the angle α. The p_{max} value is then used to choose a proper mesh to stabilize the slope.

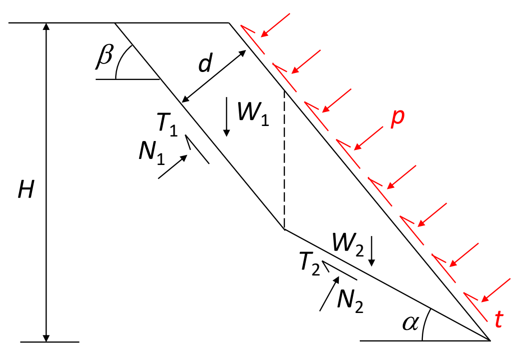

Figure 2.3 Force equilibrium on a slope divided into an upper block and a lower wedge

2.2.1.4 Soil slope between two rows of bolts

A fourth design method is proposed by the manufacturer Geobrugg, and it assumes that the slope fails between two rows of bolts, and the failure body consists of an upper block and a lower wedge (Cala et al. 2012), as shown in Figure 2.4. The method assumes that the mesh exerts a force *P* whose direction is the same as the bolting angle Ψ and a force *Z,* which is parallel with the slope surface. The *P* represents the stabilizing force on the ground, and the *Z* represents the tensile force on the mesh that is transferred to the bolts. It assumes that both P and Z are only acting on the lower wedge. The value of Z is determined by the mesh shear tests. The value of P is obtained by solving the force equilibrium equations on the two bodies based on the Mohr-Coulomb failure criterion at the sliding planes, and P is a function of the angle α. Then a proper mesh is chosen based on the maximum value of P.

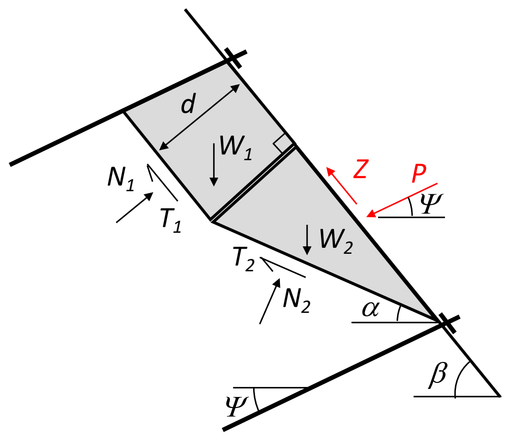

Figure 2.4 Force equilibrium on a block and a wedge between two rows of bolts

From the above design methods, the assumption that the mesh exerts a normal and a shear pressure/force on the slope surface is widely used but may not be appropriate to represent the support of steel mesh. The reason is that it is difficult to achieve a proper pretension in the mesh wires during the installation to provide such load on the slope. The support of mesh gradually increases as the mesh deformation increases. Also, a wedge-shaped failure mode is not a realistic assumption for soil slopes.

2.2.2 Design methods for rock slopes

For a bolted steel mesh system on a rock slope, the rockbolts are used to stabilize the rock blocks and also contribute to the stability of the whole rock slope. The steel mesh is used to hold the loose rocks between rockbolts on the slope. Two design methods were proposed for rock slopes by the mesh manufacturers, as described in the next two subsections.

2.2.2.1 Sliding rock between two rows of bolts

The first design method for rock slope is proposed by the manufacturer Maccaferri. The method assumes that the unstable rocks slide along the most critical joint between two rows of bolts (Grimod and Giacchetti 2014, Maccaferri 2019), as shown in Figure 2.5a. The mesh works only if the unstable rocks start to push against it. Thus the mesh is considered passive support. As shown in Figure 2.5a, the unstable rocks deform the mesh with an unbalanced force F along the sliding direction α. The upper half mesh profile has an angle of ρ to the original slope surface. The wire mesh generates a resistance force M which is perpendicular to the slope face and a tensile force T in the wire mesh. Both M and T are obtained by force equilibrium analysis. Then, the expected mesh bulge Z is obtained using the force-displacement curve of the wire mesh under the punch tests, as shown in Figure 2.5b. The proper design needs to satisfy the following conditions: (1) the tensile force T should be less than the maximum allowable tensile force in the mesh, (2) the mesh bulge Z should be less than the acceptable mesh deformation based on the specific site condition.

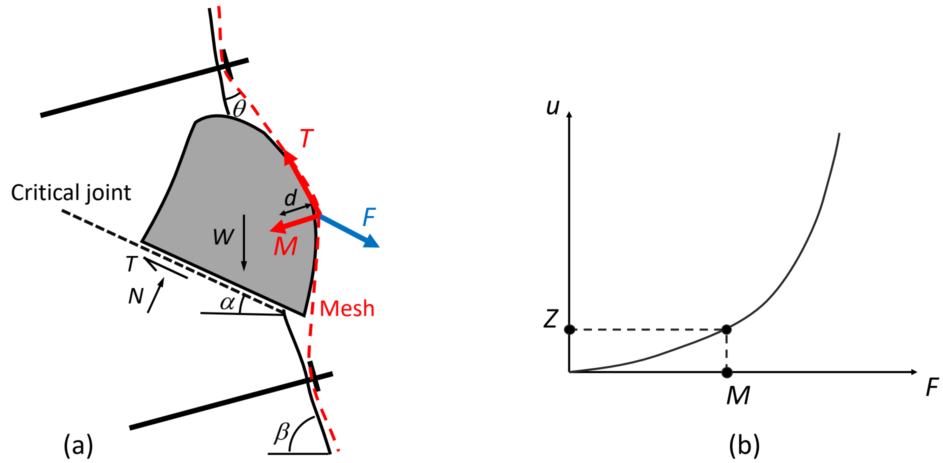

Figure 2.5 (a) Force equilibrium analysis for sliding rocks between two rows of bolts and (b) force-displacement curve of mesh from punch tests

However, rigid frames are often used to fix the outer boundaries of the steel mesh during laboratory the punch tests. In the field, the mesh is pinned by bolts. Many factors can affect the force-displacement response of steel mesh, which limits the application of this design method.

2.2.2.2 Support on a rock boulder

Another design method is for a single rock block protection is proposed by the manufacturer Geobrugg (Geobrugg AG 2017). The rock between the two bolts is assumed to be unstable, as shown in Figure 2.6. The unstable rock fails along a most critical joint whose dip angle is α. The unstable rock is supported by the mesh on its surface, and the bolts surrounding it whose job is to tension the mesh. The bolt below the rock is assumed to take the majority of the loads. The mesh provides a support force M to stabilize the rock block. The direction of M depends on the mesh geometry with respect to the slope and the force transferred through the mesh to the top and bottom bolts (T_1 and T_2). The T_1 and T_2 are the two components of M. The ratio between T_2 and T_1 is determined based on the contact condition between the rock and mesh. The value of M is obtained by the force equilibrium analysis based on the Mohr-Coulomb failure criterion at the sliding plane.

The value of T_1 and T_2 are then obtained by the decomposition of M. The T_1 and T_2 should be less than the mesh tensile strength.

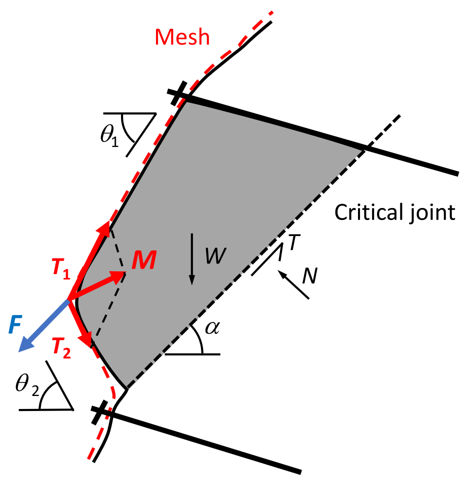

Figure 2.6 Force equilibrium analysis on a single rock between two rows of bolts

In this method, the values of T_1 and T_2 depend on the assumed ratio between these two forces. The ratio has a large influence on the magnitudes of T_1 and T_2. The magnitudes of T_1 and T_2 are also affected by the rock geometry and interaction between the rock and mesh.

2.3 Experimental tests on wire mesh

The knowledge of the mechanical response of the wire mesh is important no matter what kind of design method is used. Various laboratory tests and field tests have been carried out to investigate the characteristics of wire mesh, such as the tensile strength, the resistant capacity in the direction which is perpendicular to the mesh, the friction between the wire mesh and rocks, and dynamic response of wire mesh.

2.3.1 Laboratory tests

The tensile tests and punch tests are the two widely used small-scale laboratory tests on the wire meshes. The tensile tests stretch the mesh sheet by holding its two opposite sides to examine the mesh tensile strength, while the punch tests apply a load in a direction that is perpendicular to the mesh sheet to examine the resistant capacity of the wire mesh. A variety of mesh types have been tested by these two methods, such as the double-twisted wire mesh (Sasiharan et al. 2006, Bertrand et al. 2008), the high-tensile steel wire mesh (Castro-Fresno 2000, Cala et al. 2012, Justo et al. 2014), the chain-link wire net (Escallon et al. 2015), the omega mesh (Bertrand et al. 2012), the cable net (Sasiharan et al. 2006, Castro-Fresno et al. 2009), and the wire ring net (Xu et al. 2018). In 2016, two international test standards (International Organization for Standardization 2016a, 2016b) were developed to guide the tensile tests and punch tests. These two kinds of tests provide the fundamental force-displacement relationships of the wire meshes, which is necessary for the design of the bolted mesh system. The results from the mesh tensile and punch tests have been extensively used to calibrate and validate numerical mesh models (Bertrand et al. 2008, del Coz Díaz et al. 2009, Thoeni et al. 2013, von Boetticher and Volkwein 2019, Xu et al. 2019).

Despite the tensile strength and resistant capacity of the mesh, the interaction between the slope surface and mesh is another important factor in the design of bolted steel mesh systems (Da Costa and Sagaseta 2010). Gratchev et al. (2015) designed and conducted a series of laboratory tilt tests on different kinds of meshes to investigate the interface friction between the mesh and irregularly shaped rocks. They found that the interlocking effect usually occurs when the mesh interacts with the rocks with irregular shapes. The tangential resistance force between the mesh and rock increases as the slope angle increases. A friction angle of 25° to 30° between the rock surface and mesh was suggested in the design.

In terms of the protection from the rockfall impact, the mesh response in the impact loading is significant in the designs of rockfall draperies, rockfall attenuators, and rockfall fences/barriers, as well as in the design of bolted mesh system. Various rockfall impact laboratory tests have been conducted on different types and sizes of meshes (Buzzi et al. 2012, 2015, Gentilini et al. 2013, Qi et al. 2018, Gao et al. 2018). These tests are usually carried out by dropping a block to hit the mesh panel. The results from the rockfall impact tests show that the mesh's capability to capture the rock and absorb energy is influenced by the mesh stiffness, the mesh geometries, the block sizes and the impact speed.

2.3.2 Field tests

Different from the laboratory tests, the field tests are usually carried out on real slopes, which can obtain a more realistic mesh behaviour in the field than in the laboratory. For the bolted mesh system, the mesh is pinned by a pattern of bolts/anchors in the field tests, whereas the laboratory tests commonly use rigid frames to fix the mesh boundaries. Bertolo et al. (2009) conducted a series of full-scale field tests on the bolted mesh and found that the mesh deformation is generally larger in the field tests than that in the laboratory tests. Thus, it is necessary to consider the real force-displacement relationship of steel mesh into the design.

The field tests also help better understand the load transfer mechanism between the unstable rock, mesh, bolts (Shu et al. 2005b, Flum and Roduner 2010, Cala et al. 2013a), as well as the external loads like the snow (Shu et al. 2005a). This is quite useful when a design concept needs to be explained and verified (Cala et al. 2013b). The results from the field tests can also be used to examine whether an assumption in a design method is appropriate. For example, Blanco-Fernandez et al. (2013) found that the stress in the mesh wires are very small after installation comparing to the tensile strength of the wire, and the whole bolted mesh systems are barely pre-stressed by the measurements in three field tests. They argued that it is questionable to assume that the mesh exerts an active force to the ground in the current design methods.

For rockfall protection, the field tests are widely used to better understand the performance of rockfall draperies and fences. Giacomini et al. (2012) conducted a series of rockfall tests on a rock slope above a mining portal to investigate the influence of a mesh drapery system on rockfall hazard mitigation. They released different sizes of concrete blocks from the top of the slope underneath the mesh drapery. The results show that the mesh drapery can decrease the length of the impact zone and can reduce the energy of the blocks when they hit the portal. For the rockfall fences, the field tests were performed by releasing the concrete blocks from the top of a slope to hit the rockfall fences (Gottardi and Govoni 2010, Bertrand et al. 2012, Tran et al. 2013, Xu et al. 2018). These tests aim to examine the capability of rockfall fences to dissipate the high impact energy and to study the influence factors on the fence performance and ultimately to improve the fence design.

2.4 Numerical simulations of wire mesh

Numerical modelling is an alternative approach comparing to expensive and time-consuming physical experiments. The experimental test results are usually used to calibrate the mesh models. After calibration, the mesh models can capture the mechanical characteristics of the real mesh.

The numerical approach can provide a better insight into the relationship between the force and displacement in wire mesh and rock bolts, which are hard to obtain from experimental tests. The numerical approach is more capable of investigating the influence of different parameters for optimizing the design, such as bolt pattern, bolt spacing, and mesh type. The finite element method (FEM) and the discrete element method (DEM) are the most popular numerical approaches in modelling the wire mesh.

2.4.1 Finite element method

The finite element method (FEM) is widely used to model the wire mesh. A variety of FEM computer programs have been applied by different researchers, among which the ABAQUS is the most popular one (Sasiharan et al. 2006, Spadari et al. 2012, Gentilini et al. 2012, 2013, Escallon et al. 2013, 2015, de Miranda et al. 2015). The other FEM software used to simulate the wire meshes are the ANSYS (Castro-Fresno et al. 2008, del Coz Díaz et al. 2009, Blanco-Fernandez et al. 2016), FARO (Volkwein 2005, Roth and Ranta-Korpi 2007), and LS-DYNA (Tran et al. 2013). Different approaches have been developed to simulate the mesh using different elements in FEM, such as the truss element, beam element, link element, and membrane element.

The finite element simulations are usually performed to reproduce the experimental tests on the wire meshes. The FEM mesh models can be used to simulate both quasi-static tests like the tensile tests (del Coz Díaz et al. 2009, Escallon et al. 2015) and punch tests (Castro-Fresno et al. 2008), and dynamic tests like the rockfall impact tests (Cazzani et al. 2002, Spadari et al. 2012, Tran et al. 2013, de Miranda et al. 2015, Mentani et al. 2018) and rockburst tests (Roth and Ranta-Korpi 2007). The FEM needs to integrate specific algorithms to simulate large displacements and motion.

The numerical test results are then compared to the experimental test results to obtain an ideal mesh model that can capture the mechanical response of the physical wire mesh.

The calibrated mesh models are effective tools to examine and design the flexible structures for slope protection, such as the draperies, rockfall fences and bolted meshes (Roth and Ranta-Korpi 2007, Gentilini et al. 2013). For example, Sasiharan et al. (2006) analyzed the effect of the mesh weight, the friction interface between the rock and the mesh, and the accumulation of debris on the performance of the draped wire mesh and cable net system; Castro-Fresno et al. (2008) investigated the force-displacement relationship and mesh resistance capability for different mesh sizes in the cable net system; Spadari et al. (2012) analyzed the influence of block sizes, impact speeds and wire mesh geometries on the bullet effect of rockfall fences; de Miranda et al. (2015) and Escallon et al. (2013, 2015) evaluated the capability of rockfall fences to dissipate the high rockfall impact energy.

However, FEM is based on continuum mechanics theory, so it is difficult to deal with problems like steel mesh interacting with rocks, large displacement in the mesh and rupture of mesh wires. Specific algorithms are required, which makes FEM computational demanding.

2.4.2 Discrete element method

The discrete element method (DEM) works well for modelling discontinuous materials and can easily simulate large displacement and failures between elements. A DEM model can simulate the behaviour of steel mesh interacting with loose rocks where the mesh may sustain large deformation and mesh wires may break during the loading.

Bertrand et al. (2008) developed a mesh model using particle elements in the discrete element code, PFC3D, to simulate the double-twisted hexagonal wire mesh. This approach simulates the wire mesh by setting one particle at each node in the mesh. The mesh wire is represented by a virtual spring which connects two particles at each end. The virtual spring only captures the tensile behaviour of the wire, which is obtained from the tensile tests of a single mesh wire. However, this approach ignores the distortion of wires and the loose connections where wires bend around each other and the mesh model behaves stiffer than real mesh. Thoeni et al. (2013) proposed an algorithm to overcome this problem by modifying the force-displacement relationship of the mesh wire that is assigned in the model. The improved approach has been implemented into the open-source DEM code, YADE (Šmilauer et al. 2015). The limitations of this approach are that no physical wires are simulated, and the springs in the mesh model can only handle tension. The compression, bending and twisting in mesh wires are not simulated.

The steel mesh can also be modelled by the cylinder elements in YADE (Xu and Tannant 2016, Effeindzourou et al. 2017, Albaba et al. 2017). The cylinder element was first introduced by Bourrier et al. (2013), and it is a deformable beam-like element that can handle tension, bending, and twisting (Effeindzourou et al. 2016). One mesh wire is simulated by either a cylinder element or multiple connected cylinder elements. Compared to the use of particles, more elements are required to create a model by using cylinders.

Besides PFC3D and YADE, various software packages have also been used to model the wire mesh. Baek (2018) applied the beam structural elements to simulate welded wire mesh using 3DEC. Coulibaly et al. (2019) developed a DEM software, GENEROCK, which is dedicated to modelling and simulations of rockfall ring nets. YADE is the only open-source software package that has been used for modelling steel mesh. The advantages of using YADE are (1) it is easier to examine the source code to better understand the algorithm; (2) the code can be modified to achieve specific needs; (3) developers and researchers keep adding new elements and new features into the software package.

The discrete element simulations were also conducted to reproduce the experimental tests to compare with the experiment results and to calibrate the mesh models (Bertrand et al. 2012, Thoeni et al. 2014, Baek 2018). The calibrated models were then applied to study the influence factors that affect the mesh performance and to improve the design of the flexible protection systems (Bourrier et al. 2015, Li and Zhao 2018, Xu et al. 2019).

2.5 Integrated mathematical and numerical methods as design tools

The collaboration of numerical simulations and mathematical methods has become popular as a novel design tool in civil engineering applications in recent years. Compared to the limit equilibrium method, this approach can generate metamodels that statistically capture the complex structural response considering various influence factors in a computationally cost-effective way. The mathematical methods that have been applied in geotechnical applications include the reliability approach (Bourrier et al. 2015, Mentani et al. 2016), the response surface method (RSM) (Mollon et al. 2011, Shamekhi and Tannant 2015, Blanco-Fernandez et al. 2016), artificial neural networks (ANN) (Lu and Rosenbaum 2003, Cho 2009), and the support vector machine (SVM) (Zhao 2008, Toe et al. 2018, Liu et al. 2019). The SVM approach (Vapnik 2000) overcomes the limitations of RSM and ANN because it can cope with problems beyond nonlinear concave or convex surfaces, and the results of SVM can be expressed in an explicit form (Zhao 2008). The integrated mathematical and numerical methods have been successfully applied in the design of rockfall fences/barriers (Bourrier et al. 2015, Mentani et al. 2016, Toe et al. 2018) and bolted steel mesh for soil slopes (Blanco-Fernandez et al. 2016).

2.6 Summary

The current design methods of the bolted steel mesh system mainly focus on stabilizing shallow soil slopes or heavily weathered rock slopes. These design methods assume that the mesh is appropriately pretensioned after installation. However, the stress in the mesh wires was found to be lower compared to their tensile strength in the field, which limits the application of the current design methods. The majority of the laboratory tests of wire mesh were performed in fixed frames, while the mesh is usually pinned by a pattern of bolts on the slope surface. The knowledge of the mechanical response of bolted mesh is significant no matter what kind of design method is used. The field tests are ideal to obtain the realistic behaviour of bolted mesh on the slope, but they are expensive and time-consuming. Alternatively, the numerical simulations can take advantage of the results from experimental tests to calibrate the mesh models and then provide a better insight into the behaviour of bolted mesh considering various influence factors. Compared to FEM, DEM is more suitable to model the behaviour of steel mesh interacting with the rock where the mesh may sustain large deformation and mesh wires may break during the loading. The application of mathematical methods can further utilize the results from numerical simulations to provide metamodels for the mesh performance analysis.

Chapter 3: Discrete element modelling of high-tensile steel wire mesh

3.1 Overview

As an alternative approach to expensive and time-consuming physical experiments, numerical modelling can be used to investigate different configurations and boundary conditions of bolted steel mesh. The purpose of this chapter is to determine a proper numerical model that can realistically and efficiently simulate the steel wire mesh. This chapter presents three approaches to simulate the steel wire mesh using the open-source DEM code YADE (Šmilauer et al. 2015). Although the demonstrated mesh type is TECCO G65/3 high-tensile steel wire mesh, these simulation methods can also simulate other types of steel mesh, such as the double-twisted mesh. The mesh models were compared in terms of their mechanical response and computational cost. The chosen steel mesh model was calibrated and validated with published tensile and punch test results on TECCO G65/3 steel mesh (Castro-Fresno 2000, Cala et al. 2012).

3.2 Mechanical properties of high-tensile steel wire mesh

The 3 mm diameter wires in the TECCO G65/3 steel wire mesh create a pattern of rhombohedral 83 × 143 mm openings, as shown in Figure 3.1. The ultimate tensile strength of a single wire in this mesh is approximately 1.77 GPa (12.5 kN). The weight of the mesh is 1.65 kg/m^2 (Geobrugg 2014). Each wire in the mesh is bent into a zig-zag pattern. Each bend in one direction hooks with the wire immediately above it, and each bend in the opposite direction with the wire below it. The wires form a diamond shape opening with a ratio of 1.72 between the longitudinal (143 mm) and transverse dimensions (83 mm). The wires in the mesh have loose contact at each bend. The longitudinal direction is the stiffest direction in the steel mesh, whereas the transverse direction is much more deformable.

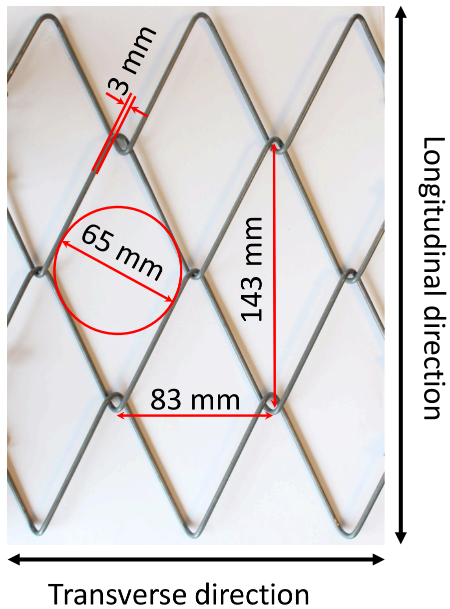

Figure 3.1 TECCO G65/3 high-tensile steel wire mesh

3.3 YADE discrete element modelling

3.3.1 A brief introduction on YADE DEM modelling

The discrete element method (DEM) simulates dynamic and deformable objects using an assembly of discrete elements (Cundall and Strack 1979). The method was implemented in the open-source software YADE by Šmilauer et al. (2015). The classical discrete elements are spherical particle elements and triangular facet elements. Researchers have been continuously developing new discrete elements in YADE, such as cylinder elements (Bourrier et al. 2013), pfacet element (Effeindzourou et al. 2016), and polyhedral elements (Eliáš 2014).

The discrete elements can interact with each other via contact forces that are generated by their relative motions and their contact relationships (contact laws). The motion of the elements is controlled by the equations of Newton's second law. The contact laws (constitutive laws) determine the force acting on the discrete elements when they interact with each other. In a typical step cycle in YADE simulation, as shown in Figure 3.2, the resultant force on each discrete element from the previous step first resets to zero (named "ForceResetter"); then, the position of each element is detected to determine collision between elements (named "SortCollider"); next, new interactions are created and forces are calculated based on the contact law and other external conditions like gravity or boundary conditions (named "InteractionLoop"); finally, the velocity and position of each element are updated by solving the equations of Newton's second law (named "Newton").

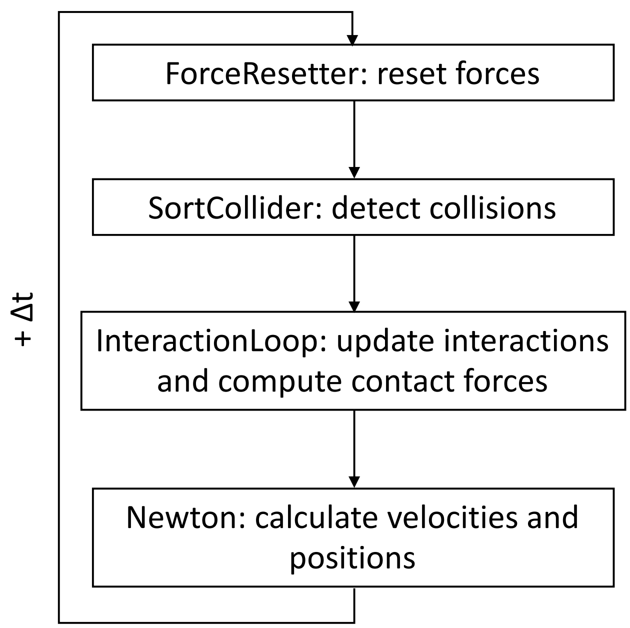

Figure 3.2 One step cycle in YADE simulation

3.3.2 Particle and facet element

The classical frictional contact interaction between two elements is shown in Figure 3.3. If the distance between the centres of two particles (l) is smaller than the sum of their radius ($l < R_1 + R_2$), these particles will contact each other. The contact force F between these particles is generated by the relative displacement and overlap of the two particles. The contact force F consists of a normal contact force F_n and a shear contact force F_s, defined as:

$$F_n = k_n u_n \tag{3.1}$$

$$\Delta F_s = k_s \Delta u_s \tag{3.2}$$

$$k_n = \frac{2E_1R_1E_2R_2}{E_1R_1 + E_2R_2} \tag{3.3}$$

$$k_s = \alpha k_n \tag{3.4}$$

where k_n and k_s are the contact stiffness associated with normal force and shear force, u_n is the relative normal displacement (or overlap) between two particles, u_s is the relative shear displacement, E_1 and E_2 are Young's modulus of the two particles, R_1 and R_2 are the radii of the two particles.

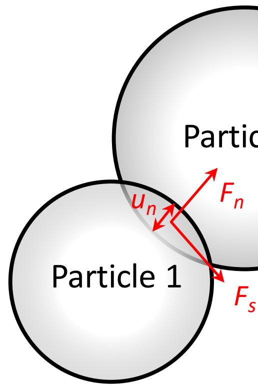

Figure 3.3 Particle-particle interaction

Slip will occur in the tangential direction if

$$|F_s| \geq |F_n| \tan \varphi \tag{3.5}$$

where φ is the friction angle between the particles. Figure 3.4 shows a plot of the basic contact law in the normal and tangential directions.

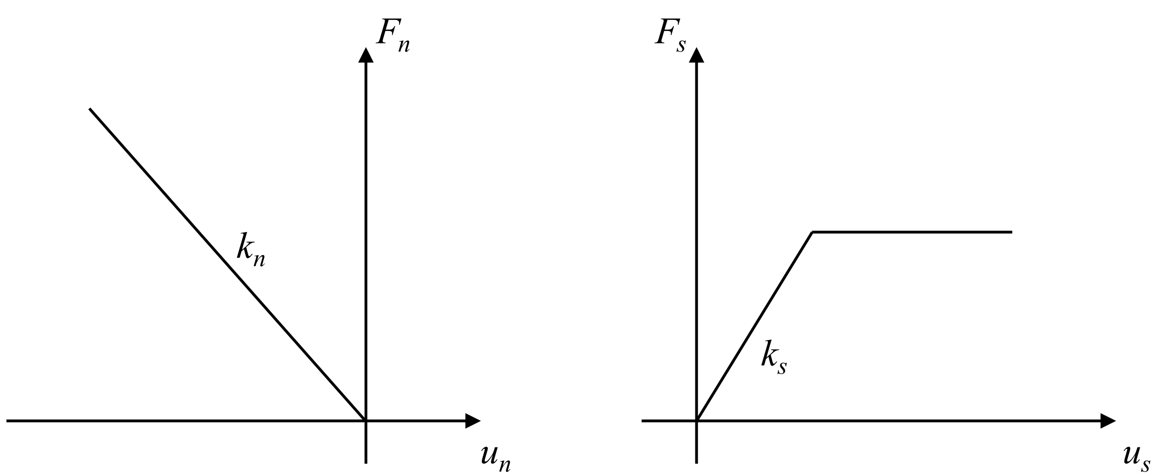

Figure 3.4 Schematic plots of the contact law between two particles

A cohesive frictional contact can bond two particles together. In this situation, a bending moment M_b and a twisting moment M_t will be generated between them. The M_b and M_t are defined as:

$$M_b = k_b \Omega_{12}^b \tag{3.6}$$

$$M_t = k_t \Omega_{12}^t \tag{3.7}$$

where k_b and k_t are the contact stiffness for bending moment and twisting moment, Ω_{12}^b and Ω_{12}^t are the bending and twisting components of relative rotation.

The elastic limits are defined by:

$$F_n \leq \sigma_n^l A \tag{3.8}$$

$$F_s \leq F_n \tan\phi + \sigma_s^l A \tag{3.9}$$

$$M_b \leq \frac{\sigma_n^l I_b}{R} \tag{3.10}$$

$$M_t \leq \frac{\sigma_s^l I_t}{R} \tag{3.11}$$

where σ_n^l and σ_s^l are the tensile and shear strengths, A is the reference surface area, R is the minimum radius of the two spheres, $I_b = \pi R_c^4/4$ and $I_t = \pi R_c^4/8$ are the reference polar and bending moments of inertia.

The interaction between a particle and a triangle facet element is shown in Figure 3.5. If the distance between a particle and a facet is smaller than the radius of the particle, then a contact force F will be generated at the contact point based on the relative displacement and overlap between the particle and the facet. F has a normal component F_n and a tangential component F_s. The Equations (3.1) – (3.5) are also applied in the particle-facet contact.

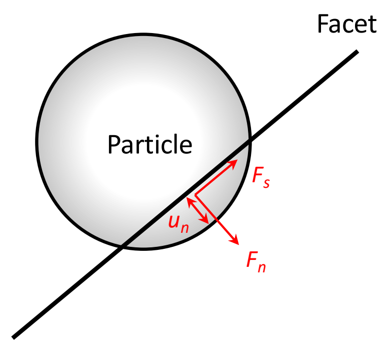

Figure 3.5 Particle-facet interaction

3.3.3 Cylinder element

The cylinder element was first introduced by Bourrier et al. (2013). A cylinder element consists of two spherical particles connected by a cylinder. A cylinder element corresponds geometrically to the Minkowski sum of a polyline and a sphere (Figure 3.6). A cylinder element behaves like a classical discrete element. One cylinder can deform in the axial direction, but it cannot bend. Two or more cylinders can be connected at one particle, which is often called a node.

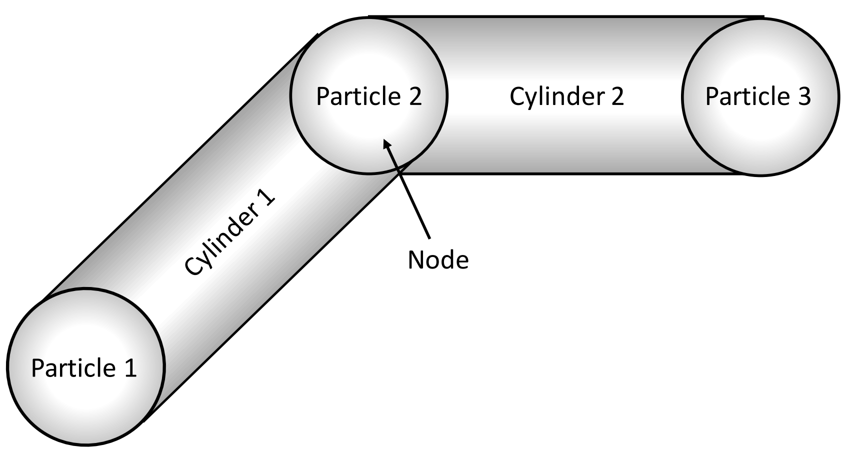

Figure 3.6 Cylinder elements connected at a node

A beam-like constitutive law was developed for the cylinder elements (Bourrier et al. 2013). A cylinder can rotate and twist at the node, thus by using multiple cylinders connected by nodes, a model of steel wire can be created that allows the wire to both elongate and bend. The axial deformation of the cylinder is defined by the positions of the two nodes at each end. Two or more connected cylinder elements behave like a beam, whose constitutive behaviour contains tensile and shear forces, as well as bending and twisting moments. The node that connects two cylinders behaves like a virtual rotational spring, as shown in Figure 3.7. The mass of a cylinder element is lumped at its nodes.

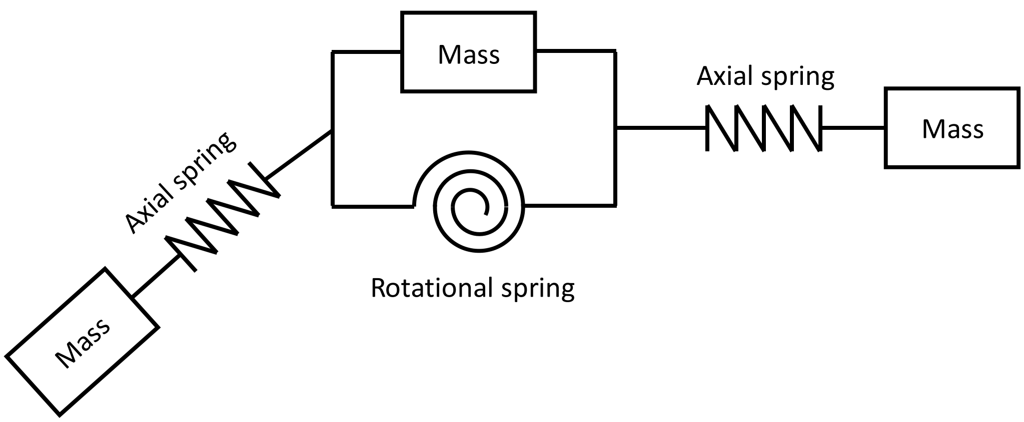

Figure 3.7 Beam-like constitutive law for cylinder elements

For a single cylinder element, the contact stiffnesses are defined as:

$$k_n = \frac{E_n A}{L} \tag{3.12}$$

$$k_t = \frac{G_t I_t}{L} \tag{3.13}$$

$$k_s = \frac{12E_b I_b}{L^3} \tag{3.14}$$

$$k_b = \frac{E_b I_b}{L} \tag{3.15}$$

where E_n is the tensile or compressive modulus, E_b is the bending modulus, G_t is the shear modulus associated with a twisting moment, L is the distance between the centre of two spheres, A is the reference surface area.

The elastic limit of the cylinder elements is defined by a tensile force limit F_n and shear force limit F_s which are determined by Equations (3.8) and (3.9). These limits are related to the tensile strength σ_n^l and shear strength σ_s^l that allow the cylinder elements to model elastic perfectly plastic beams.

The formulation allows the model to capture particle-cylinder interaction and cylinder-cylinder interaction (Figure 3.8). In the particle-cylinder interaction model, a virtual particle within the cylinder is generated at the contact point (Figure 3.8a). The virtual particle has the same radius as the cylinder, and the position of the virtual particle is at the projection of the contact point between the particle and the cylinder on the segment connecting the cylinder nodes. The particle-cylinder interaction turns into the classical particle-particle interaction. In the cylinder-cylinder interaction model, two virtual particles for each cylinder are generated at the contact point (Figure 3.8b). Similarly, cylinder-cylinder interaction can be turned into a particle-particle interaction. In YADE, the material properties assigned to the particles in cylinder elements control the behaviour of the cylinder while the material properties assigned to the cylinder control the interaction between unconnected cylinder elements.

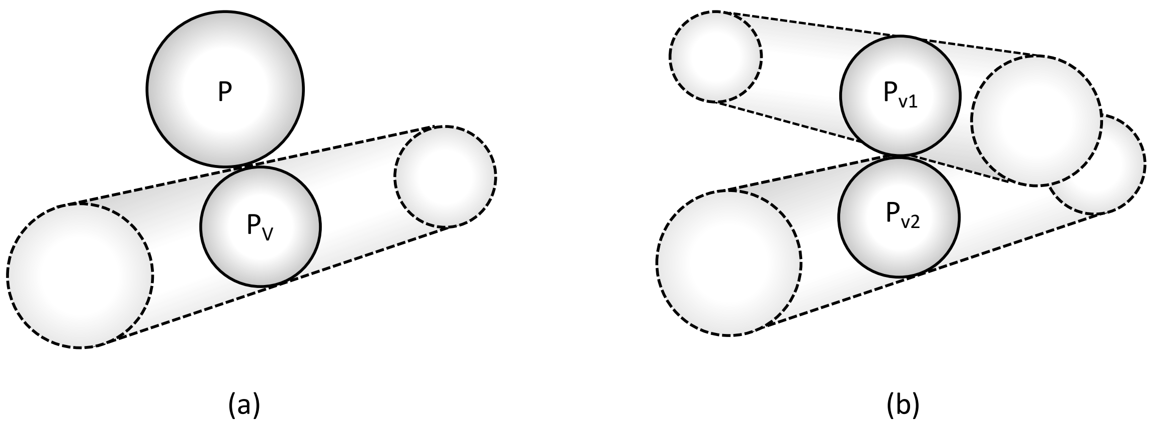

Figure 3.8 Contact interaction for (a) particle-cylinder and (b) cylinder-cylinder, showing virtual particles

3.4 Steel mesh simulated by cylinder elements with a beam-like constitutive law

One approach to simulate steel mesh in YADE is to use the cylinder element with the beam-like constitutive law, which was proposed by Xu and Tannant (2016). A length of the wire is represented by a cylinder connecting two nodes (particles). The properties assigned to the cylinder elements are listed in Table 3.1 to simulate a TECCO G65/3 steel wire mesh. The diameter of a cylinder element is set to 3 mm to represent a 3 mm diameter wire. The Young's modulus and tensile strength come from testing results of the wire, while other parameters are assumed based on engineering experience. The beam-like constitutive law was assigned to the spherical particles in the cylinder element to capture the mechanical characteristics of a wire (internal connection in a cylinder). A frictional contact was assigned to the cylinders to simulate the interaction between different wires.

Table 3.1 Parameters of cylinder elements used to represent steel wire in TECCO G65/3 mesh

Property	Particles	Cylinders
Young's modulus E (GPa)	200	200
k_s/k_n	0	0.2
Density ρ (kg/m^3)	7850	7850
φ (°)	25	25
Tensile strength σ_t (GPa)	1.77	na
Shear strength σ_s (GPa)	1.77	na

An example of a cylinder element to simulate a steel wire with 100 mm length and 3 mm diameter is used to demonstrate the calculation of the contact stiffnesses in the cylinder element using the values Table 3.1. From Equations (3.12) and (3.14), the normal stiffness k_n is 1.4×10^7 N/m, and the shear stiffness k_s is 9.5×10^3 N/m. The contact stiffnesses of a cylinder element depend on its length and cross-sectional dimension.

For the contact between two cylinders to represent the interaction between two wires, the normal stiffness k_n is 3×10^8 N/m, and the shear stiffness k_s is 6×10^7 N/m using Equations (3.3) and (3.4)

3.4.1 Single wire loaded in tension

Published tensile test results (Cala et al. 2012) for a 100 mm length of wire with a diameter of 3 mm gave a failure load of 12.9 kN with a maximum elongation of about 2% to 2.5%. This test was modelled with one cylinder element. The bottom end of the steel wire model was fixed and a vertical velocity was applied to the upper end of the wire. Figure 3.9 shows the force-displacement curve for the model. The steel wire modelled by the cylinder element shows a linear elastic relationship. The connection between the cylinder and one of the spheres broke at a load of 12.9 kN, consistent with the ultimate tensile strength of the wire. The stiffness of the wire was 14 kN/mm, which corresponds to a wire Young's modulus of 200 GPa. The maximum elongation of the wire was 0.9 mm or a strain of 0.9%, which is about 50% less than the maximum elongation of the actual wire at rupture. This is to be expected since the wire model only captures the elastic response of the wire and in its current configuration did not simulate the plastic yield of the steel immediately preceding rupture.

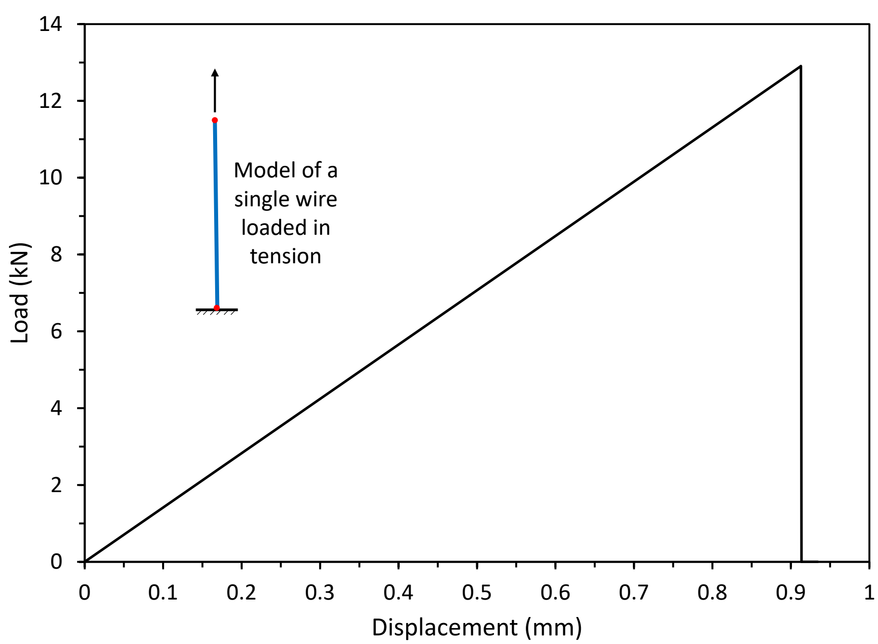

Figure 3.9 Tensile test of a wire model made from one cylinder

3.4.2 Single wire loaded in bending

A model of a wire consisting of five cylinders, each 20 mm long, connected to six nodes was constructed to test the bending behaviour of the wire model. The model represents a 100 mm length of 3 mm diameter wire. One end of the horizontal model was fixed, while a vertical load, *P*, was applied to the other end. Figure 3.10 shows the bending curve of the wire under forces of 30, 50, and 70 N. Also plotted are the analytical shapes of the deformed wire, assuming it behaves as an elastic cylindrical beam. The figure shows that the wire model can deform in a similar manner to an elastic beam, although the modelled deformations are slightly more than the analytical solution. The difference is that the wire is assumed to be homogenous and isotropic in the analytical model, while the numerical model used only five connected cylinders to represent the wire.

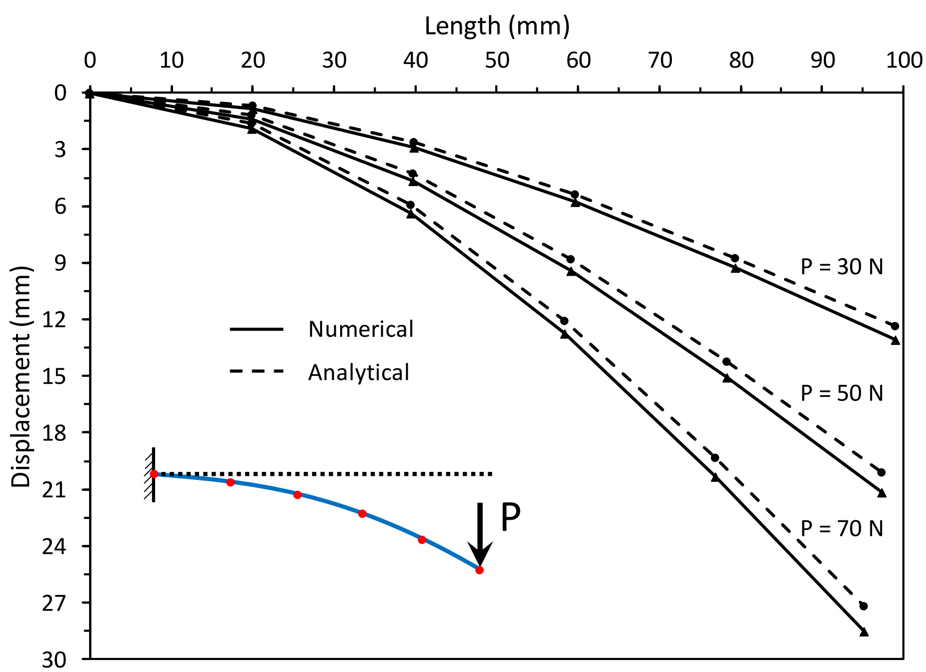

Figure 3.10 Bending test of a wire model made from five cylinders

3.4.3 Numerical models of wire mesh

Using the cylinder elements, a model of wire mesh can be constructed by connecting the spheres and cylinders to match the geometry of the mesh. The cylinders have a 3 mm diameter. Multiple connected cylinder elements are used to capture the bend geometry, where one wire in a mesh bends around another wire. In 3D, the wire has both a bend and a slight twist at this section of the mesh. Figure 3.11 shows a close-up view of the YADE model of two bent wires within a mesh. According to the sensitivity analysis from Bourrier et al. (2013), using two connected cylinder elements can roughly match the bending behaviour of a cantilever beam, while five cylinders are ideal as demonstrated in Figure 3.10. Because of the restriction on the wire length where two wires bend around each other, three cylinders are used at each wire bend (Figure 3.11). However, the difference between using three cylinders and more than three cylinders will be minor. The straight wire sections in the mesh are modelled by one cylinder element because these wires mainly carry the tensile force when loading the mesh.

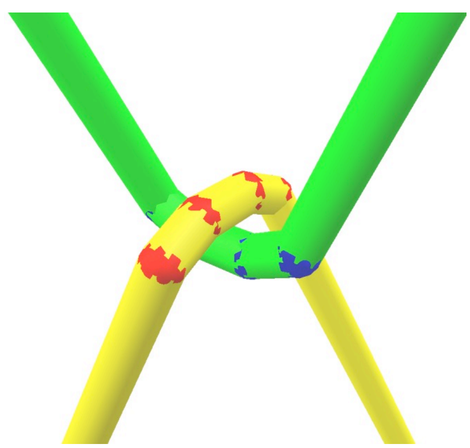

Figure 3.11 Model of two wires bent around each other

The generation of the wire mesh is based on the following steps. First, one wire is generated by following the zig-zag pattern applicable to the geometry of the specific mesh type. Then, a second wire is created, which hooks with the first wire to form the rhomboidal pattern. This step is repeated to create a large area of wire mesh. This modelling approach needs 3010 elements (cylinders plus spheres) to create a 1×1 m^2 TECCO G65/3 steel wire mesh.

A series of numerical simulations were performed to measure the capability of YADE discrete element models to capture key load-deformation behaviours of wire mesh. A model of a small section of mesh was loaded in different directions and with different constraints on the boundaries of the mesh. Two models were loaded in the longitudinal (or stiff) direction, and a third model was loaded in the transverse direction.

3.4.3.1 Longitudinal loading with mesh edges laterally constrained

A numerical model was configured such that the mesh was loaded in the longitudinal direction (vertically) at the top with the bottom of the mesh fixed into position. The loads were applied to the uppermost spheres in each of the two top wire bends. The bottom of the mesh was fixed by fixing the lower-most spheres in each of the two bottom wire bends. Both lateral edges of the mesh were constrained such that they could only move vertically. This was accomplished by restricting the motion of spheres in each of the two wires on both edges of the mesh to vertical motion. The vertical force versus vertical displacement for this model is shown in Figure 3.12. The inset in this figure shows the geometry of the mesh at a specific stage of the loading. The boundary conditions on the model combined with the geometric configuration of the two wires created a stiff load-displacement response. The mesh retained the rhombohedral pattern and only deformed a small amount before a large tensile force was developed in the wires, and a wire broke. The peak tensile force in the mesh was 40 kN, and this occurred at a displacement of 4.2 mm. This load capacity arose from the tensile strength of four wires inclined with respect to the longitudinal loading direction. If the forces are assumed to be carried by a simpler 2D geometry matching the wire orientations in the mesh, the predicted peak load would be:

$$F_{mesh} = 4 \times 12.9 \times \cos\frac{49°}{2} = 47 \text{ kN} \tag{3.16}$$

This value is higher than the predicted load of 40 kN because the mesh wires carry higher loads near the bends, i.e., the wires break at the bends.

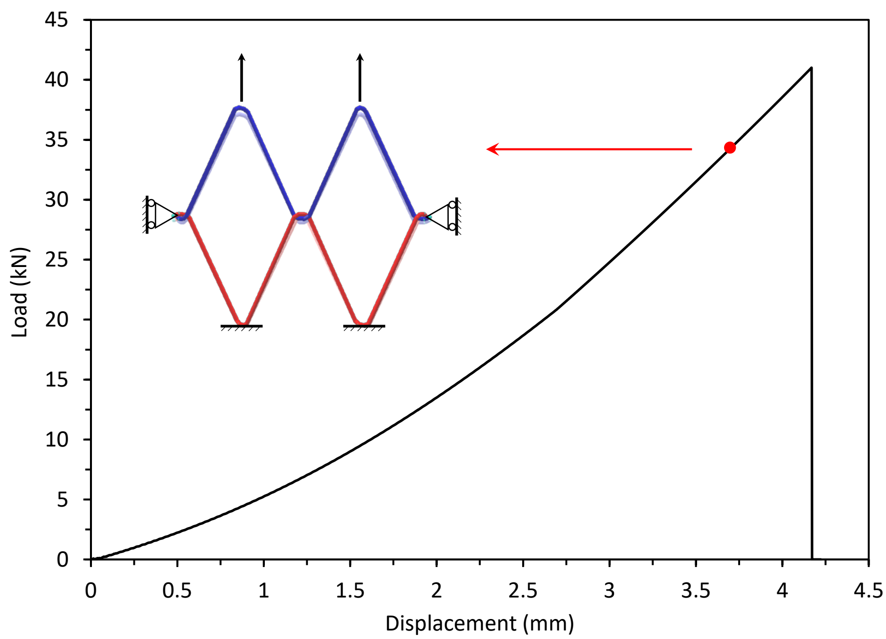

Figure 3.12 Vertical loading with sides only allowed to slide vertically

3.4.3.2 Longitudinal loading with mesh edges unconstrained

The numerical model shown in Section 3.4.3.1 was modified such that both lateral edges of the mesh were unconstrained and thus were free to move in any direction. The load applied to the top of the mesh was in the longitudinal or vertical direction only, and the loading points were free to move laterally as the mesh deformed (as they were in the model in Section 3.4.3.1). Freeing the lateral boundaries of the mesh permits much more deformation. The vertical force versus vertical displacement for this model is shown in Figure 3.13. The inset in this figure shows the geometry of the mesh at the beginning of the test, and later, when the deformation reached 8.5 mm. The much higher longitudinal displacement occurs because the mesh can deform in the transverse direction.

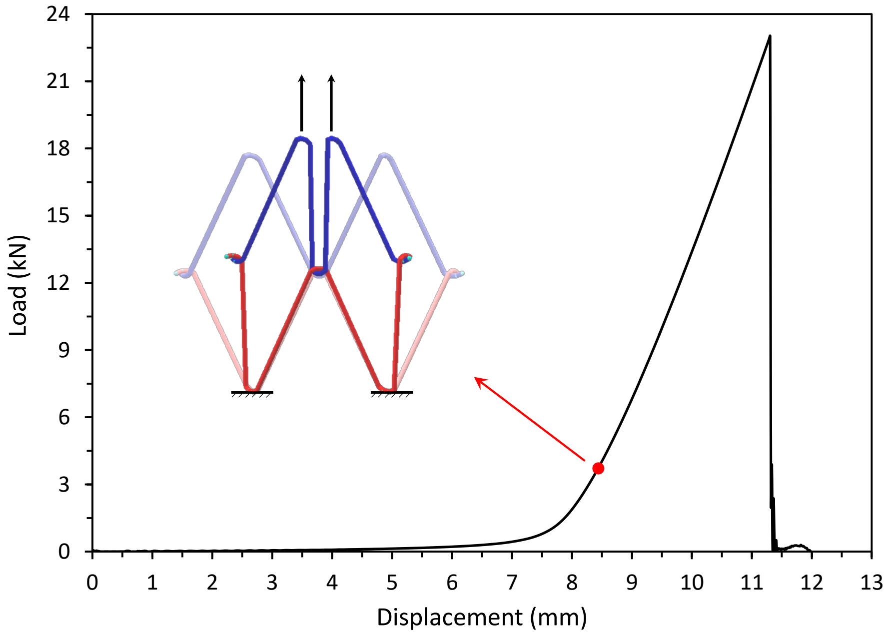

Figure 3.13 Vertical loading with sides free

In this test, both lateral edges were free and both lateral ends of the blue wires were allowed to slip out slowly from the hook during the test. There were only two wires working after that. So at failure, the load carried by the mesh is assumed to be twice the load capacity of a single wire 25.8 kN. This value is also higher than the numerical results of 23.5 kN because the mesh wires carry higher loads near the bends, i.e., the wires break at the bends.

3.4.3.3 Transverse loading with mesh top and bottom unconstrained

The numerical model presented earlier was modified again, such that loading was applied in the transverse or horizontal direction. The wires at one side of the mesh were fixed while the loading was applied to the opposite side. The other edges of the mesh were free to deform in any direction. The horizontal force versus horizontal displacement for this model is shown in Figure 3.14. The inset in this figure shows the geometry of the mesh at the beginning of the test and later when the elongation reached 150 mm. With this model configuration, the wires could simply straighten out at the bends allowing for very large displacements at small loads. After the wires deformed enough to become aligned nearly parallel with each other and the loading direction, the load carried by the wires rapidly increased until the point of failure. At failure, the load carried by the mesh was approximate twice the load capacity of a single wire.

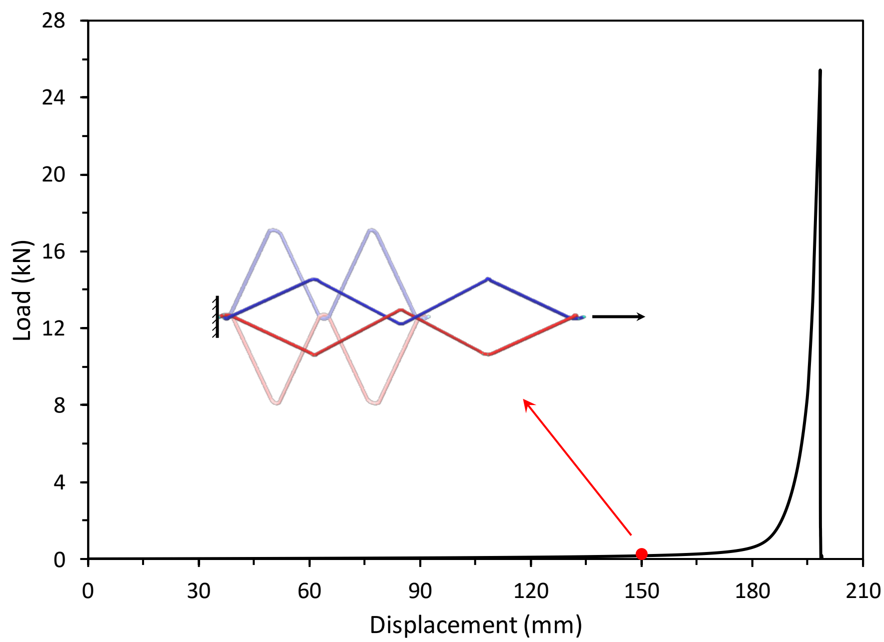

Figure 3.14 Horizontal loading with top and bottom free

3.4.3.4 Load-displacement response for mesh loaded by a rockbolt plate

A wire mesh model loaded by a rockbolt plate was created to examine the force-displacement response of the plate and the deformed shape and failure mechanism of the mesh. The model is shown in Figure 3.15. An array of connected particle elements was used to simulate the plate. The parameters of these particles are shown in Table 3.2. As these particles were clumped together, the plate in this model was rigid. The mesh was fixed around its outer perimeter. The plate was centred 20 mm below the mesh and loaded in a direction perpendicular to the mesh. Gravity was not applied in the model.

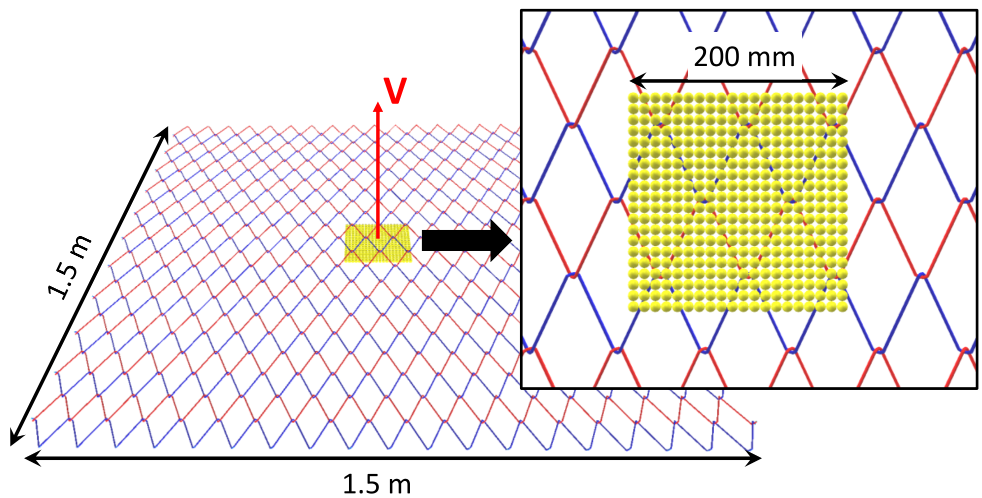

Figure 3.15 Mesh model fixed around the perimeter loaded by a simulated rockbolt plate in the centre

Table 3.2 Parameters of particle elements used to represent rockbolt plate

Property	Particle elements
Radius r (mm)	5
Young's modulus E (GPa)	200
k_s/k_n	0.3
Density ρ (kg/m^3)	7850
Friction angle φ (°)	25

The force versus the displacement for the rockbolt plate is shown in Figure 3.16. For the first 60 mm of plate movement, there was essentially no resistance by the mesh. After a plate displacement of 60 mm, the force gradually increased. When the plate displacement reached approximately 260 mm, some steel wires near the rockbolt plate broke, resulting in a sudden force decrease from 75 kN to 18 kN. The upper inset figure shows the deformation of the mesh and broken steel wires at this stage of loading. The force on the plate recovered somewhat with further displacement as the loads were transferred to other wires in the mesh. When the plate displacement reached about 288 mm, the force decreased dramatically again. As can be seen from the lower inset figure, more wires were broken resulting in substantial damage to the mesh.

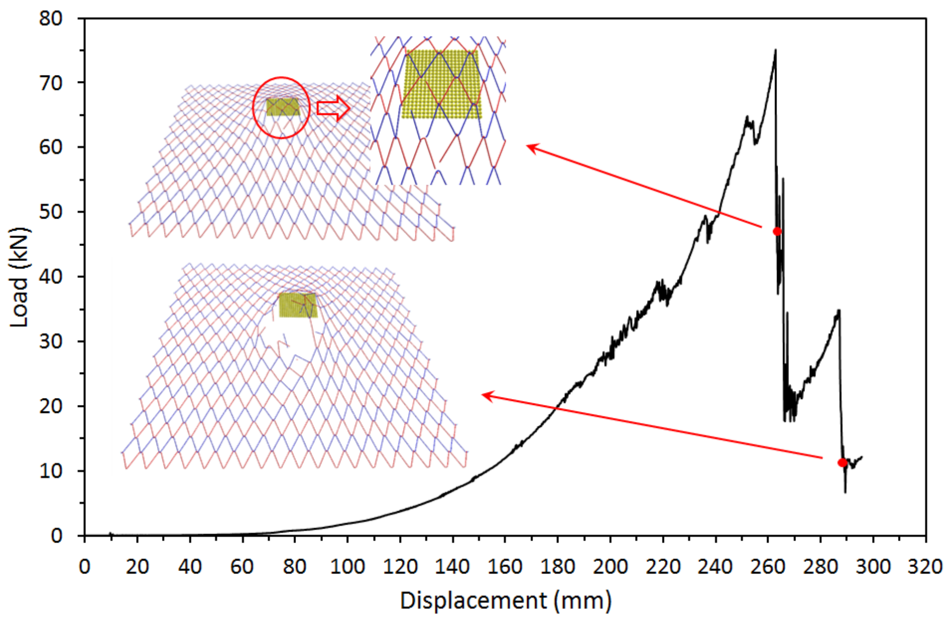

Figure 3.16 Load-displacement response of the plate and deformation/failure pattern of the mesh

Although this mesh model can simulate the large differences in the strength and stiffness of mesh loaded in the longitudinal versus the transverse direction, as well as the deformed shape and failure mechanism of the mesh, it has two limitations.

(1) The cylinder elements only allow for elastic elongation, so the wire model currently does not account for plastic deformation of the wire. From the single wire tensile test, the model has about 50% loss in the wire elongation compared to a real steel wire. This results in a mesh model that is much stiffer than the physical mesh.

(2) A large mesh model requires a large number of elements. This will become computational demanding. A powerful workstation may be needed to run this model to simulate a full-scale phenomenon where various bolt patterns and spacing are involved.

3.5 Steel mesh simulated by stochastically distorted wire model

There are other two modelling approaches in YADE to simulate steel wire mesh that can model the global mechanical response of the mesh and are also more efficient than the above modelling approach.

3.5.1 Particle-based approach

The particle-based approach was first proposed by Bertrand et al. (2008) to simulate a double-twisted wire mesh. For modelling a TECCO G65/3 mesh, this approach sets particles where the wires bend around each other, as shown in Figure 3.17. There are 187 particles per square metre in the model. The diameter of these particles is set to 0.011 m, which is the same as the thickness of the mesh panel when including the bend in the wires. The weight of the wire mesh was assumed to be distributed to every particle equally (1.65 kg/m^2/187 = 8.8 g per particle).

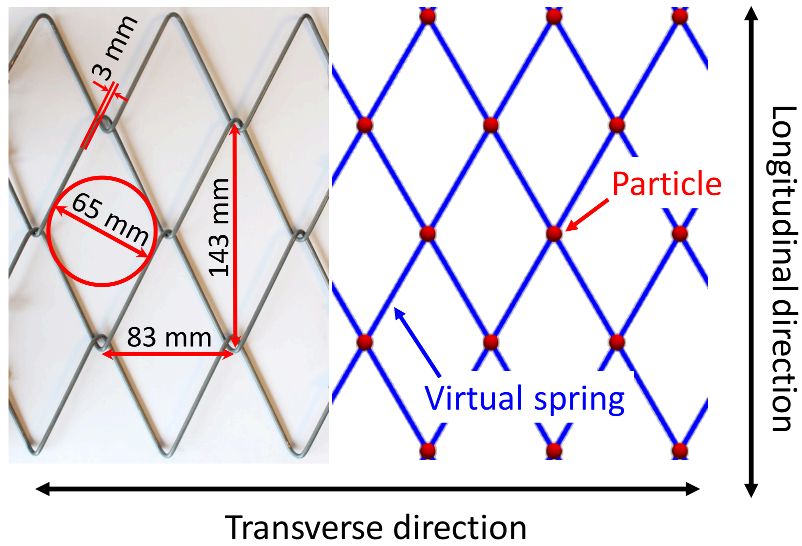

Figure 3.17 Particle-based mesh model

In the steel mesh model, there is no physical contact between the particles. Instead, the interaction between particles is captured by a virtual spring used to represent the steel wire between the particles. The force-displacement relationship of the virtual spring is defined by the stress-strain curve, length and diameter of the steel wire. Figure 3.18 shows the stress-strain curve that is used in the modelling. It is a nonlinear piecewise curve that is adopted from the results of wire tensile tests by Effeindzourou et al. (2017). In the tensile tests, the wire samples are 100 mm long and 3 mm diameter. Five points are chosen to capture the linear, yield and necking stages of the wire. These points are used in the simulation.

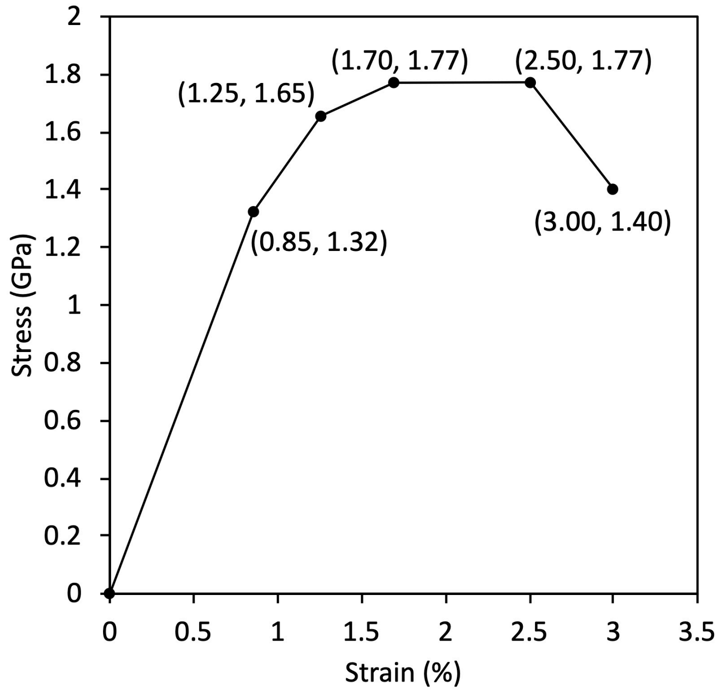

Figure 3.18 Stress-strain curve of steel wire used in the simulation

In the modelling, an algorithm converts the assigned stress-strain relationship to a force-displacement relationship based on the wire length and diameter. The force-displacement relationship is then applied to the virtual springs in the mesh model to simulate the tensile behaviour of the wires. The length and diameter of the simulated wire between two nodes are 83 mm and 3 mm, respectively. Figure 3.19 shows the tensile behaviour of this simulated wire in a numerical tensile test. The simulated wire has a nonlinear force-displacement response.

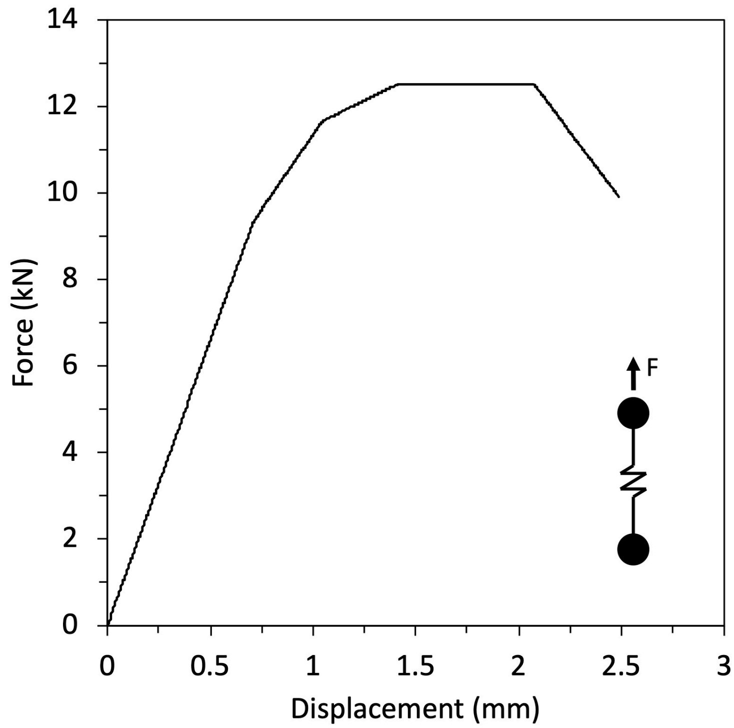

Figure 3.19 Force-displacement relationship for an 83 mm long, 3 mm diameter wire model

However, only using the curve in Figure 3.19 will make the mesh model stiffer than the real mesh. The real mesh has a loose connection at the nodes where two wires bend around. The wires may slip during the loading. In the model, four simulated wires are directly connected at one node. Thoeni et al. (2013) proposed a method to make the mesh model less stiff that allows the model to capture the global mechanical behaviour of the mesh. The method is to modify the force-displacement relationship that is assigned to the simulated wires. The modified force-displacement relationship is called the stochastically distorted wire model (SDWM), as shown in Figure 3.20.

Two shift parameters (λ_u, λ_F) are introduced to modify the curve. The parameter λ_u ($0 \leq \lambda_u \leq 1$) defines the horizontal shift distance in the curve, and the parameter λ_F ($0 \leq \lambda_F \leq 1$) defines the stiffness of the wire in the shifted area. F_l is the elastic limit. The length of a single wire (L) is limited by

$$L_0 < L < L_0(1 + \lambda_u \tilde{n}) \tag{3.17}$$

where L_0 is the initial distance between two interacted particles and $\tilde{n}$ is a random number between 0 and 1 that obeys a triangular distribution. The parameter $\tilde{n}$ accounts for randomly distributed variations in the mesh wires.

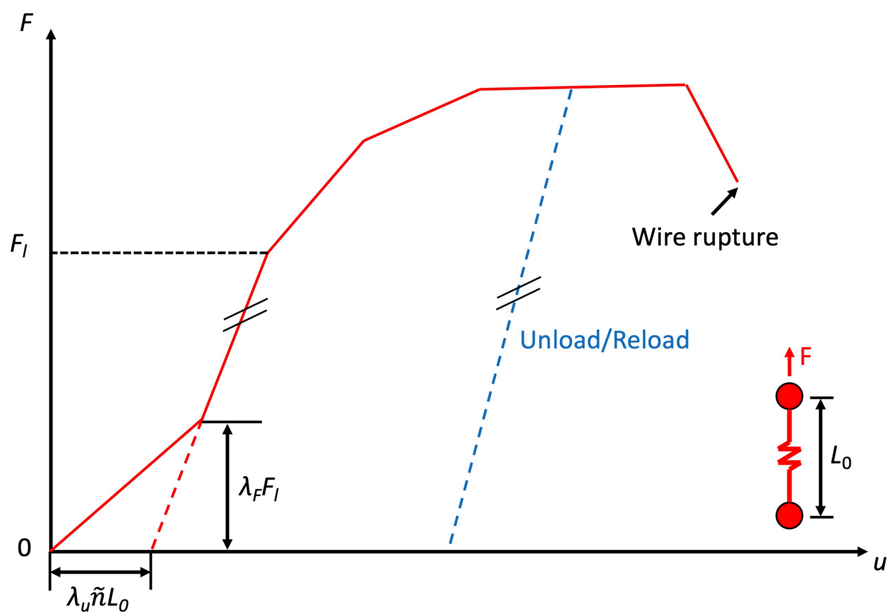

Figure 3.20 Force-displacement relationship in stochastically distorted wire model (SDWM)

In addition, the SDWM allows the unloading and reloading of a wire by setting the corresponding stiffness equal to the initial elastic stiffness. The wire model can rupture when the axial displacement reaches the elongation limit.

When creating the mesh model, the 'mesh wires' are randomly distributed in the model. This means different wires may have slightly different force-displacement relationships because of the random $\tilde{n}$. According to Thoeni et al. (2013), this parameter has a triangular distribution with 0 for the smallest, 0.5 for the most probable, and 1 for the largest value. For example, when setting the $\lambda_u = 0.2$, the average shift distance of the curves for the mesh wires is about 10% of the initial wire length. The randomness can be controlled by an integer seed factor. Using the same seed factor will always generate the same mesh model.

Figure 3.21 shows the influence of λ_u and λ_F on the force-displacement relationship of the simulated wires by a series of tensile tests. In Figure 3.21a, λ_u is set to 0.2, 0.6, and 1 while λ_F is kept as 0.5. As λ_u increases, the mesh wire needs to have a larger displacement to mobilize the force. A larger value of λ_u will make the simulated wires more deformable, which results in a more flexible mesh. If $\lambda_u = 0$, no modification is made to the original force-displacement curve. In Figure 3.21b, λ_u is kept as 0.5 while λ_F is set to 0, 0.5 and 1. Increasing the value of λ_F will not change the elongation of the simulated wire, but will change its initial stiffness. A larger λ_F results in a stiffer wire. When $\lambda_F = 0$, the simulated wire will be activated until its elongation is over $\lambda_u \tilde{n}\, L_0$. The influence of λ_u and λ_F presented here is for the behaviour of a single wire in the mesh model. It is necessary to investigate their influence on the global mechanical response of the mesh and determine the proper values for λ_u and λ_F to make the mesh model capture the behaviour of the physical mesh. These are presented in the mesh calibration in Section 3.5.4.1

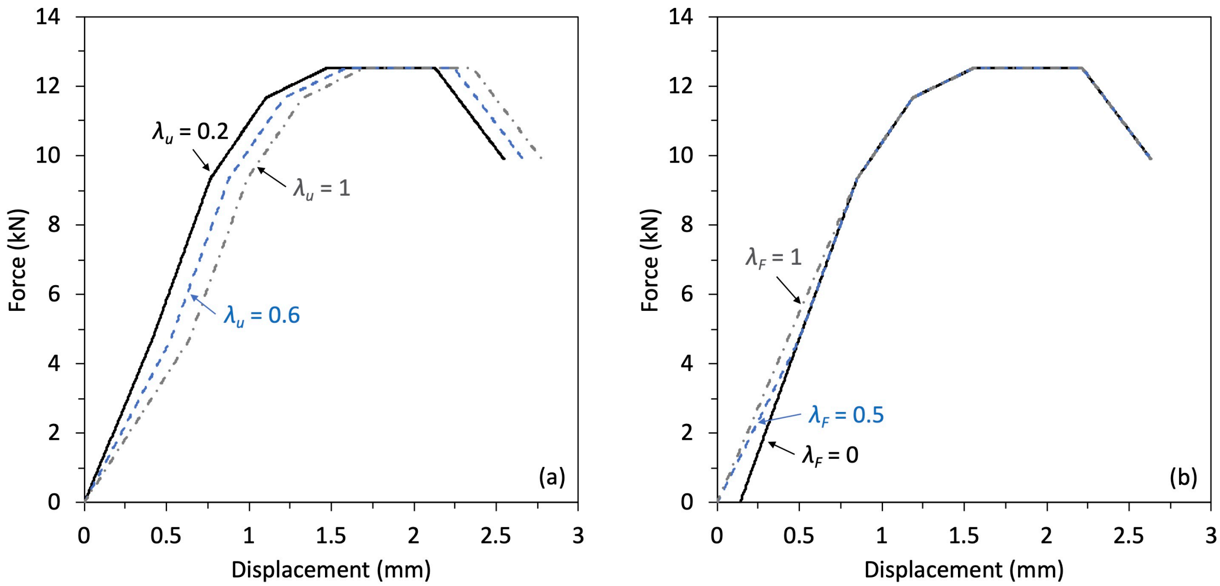

Figure 3.21 Influence of λ_u and λ_F on the force-displacement relationship of simulated wire

The wire model only considers the tensile behaviour, which means there is no compressive resistance between particles. This assumption is reasonable because the wire mesh is in tension when loaded by the rocks. Another limitation of this approach is that the wire bending is not captured in the model. However, bending does not exist in the longitudinal direction for the high-tensile steel mesh because of its special form factor. The mesh wires are only hooked at their turns allowing the mesh to fold easily. The bending in the mesh only exists in its transverse direction, but the influence of bending resistance is minor when considering the wire diameter is only 3 mm. Unlike the mesh model presented in Section 3.4, this particle-based approach cannot simulate the different stiffnesses of mesh in the longitudinal and transverse directions. However, the SDWM in the particle-based approach modifies the force-displacement relationship of the wires to give the mesh model a similar mechanical behaviour as real mesh. To some extent, the difference in the mesh stiffnesses and bending in the longitudinal and transverse directions are implicitly embedded in the model.

3.5.2 Simplified cylinder-based approach

The cylinder elements can also adopt the contact law of a stochastically distorted wire model (SDWM). As a simplified version of the modelling approach using cylinder elements, the simplified cylinder-based modelling approach uses the cylinder elements to simulate steel wire mesh by connecting four cylinder elements at each node where the wires bend around each other (Effeindzourou et al. 2017). The mesh model matches the geometry of the physical steel mesh, as shown in Figure 3.22. This simplified modelling approach assumes the nodes and cylinders are in the same plane. The eccentricities caused by folding the wires are not considered in the model. Instead, the diameter of these cylinders is set to 6 mm, which is twice as the physical wire diameter. These simplifications allow the mesh model to be more efficient to simulate the effect of the geometry of the wire mesh. In this modelling approach, the SDWM is applied in the mesh model to capture the mechanical response of the steel wire mesh.

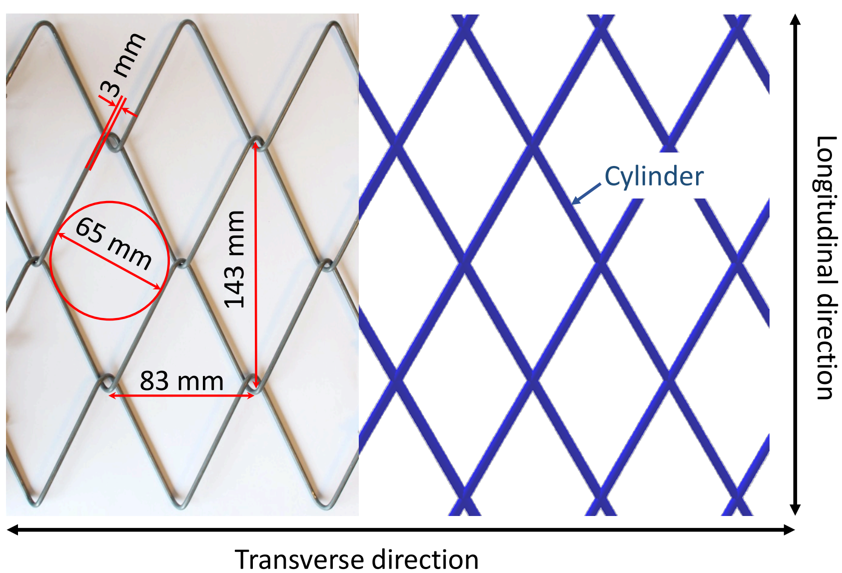

Figure 3.22 Steel mesh model by connected cylinder elements

3.5.3 Comparison between two modelling approaches using SDWM

Numerical punch tests were conducted to compare the performance of the above two modelling approaches for simulating steel wire mesh in terms of the mechanical response of mesh and computational cost. Two 3 × 3 m mesh models were generated by the particle-based approach and cylinder-based approach, respectively. The mesh models had the same mesh geometry, as shown in Figure 3.23a. There are 1613 elements in the particle-based mesh model and 4721 elements in the cylinder-based mesh model. The elements at each boundary of the mesh model were fixed in all directions. The original force-displacement curve of the 3 mm diameter wire in Figure 3.19 was applied in the two mesh models to facilitate the comparison to avoid the uncertain randomness by using the shifted curve.

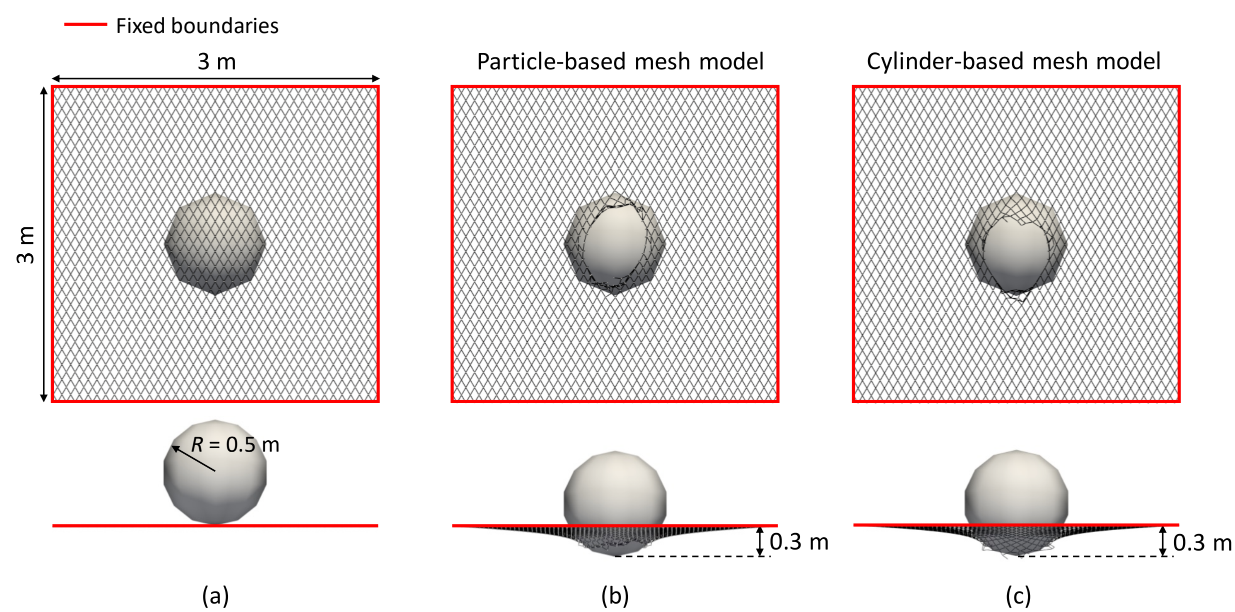

Figure 3.23 DEM punch test geometries (a) at the beginning (b) particle-based mesh model after failure (c) cylinder-based model after failure

A spherical block with a 0.5 m radius was created at the centre of each mesh model using one particle element to load the mesh. For both tests, the frictional contact law was applied between the mesh model and the spherical loading block. The contact parameters were set to $k_n = 1 \times 10^7$ N/m, $k_s/k_n = 0.15$, and $\phi = 25°$. The time step was set to 2×10^{-5} s. During the simulations, a velocity of 0.1 m/s was set to the spherical block to load the mesh. The simulations were stopped when the displacement of the spherical block was over 0.3 m. The force and displacement of the spherical block were recorded during the tests.

Figure 3.23b and c show the mesh geometries when the tests were stopped for the particle-based model and cylinder-based model, respectively. Both mesh models experienced failure of mesh wires from the centre of the mesh when the tests ended. Figure 3.24 shows the force-displacement curves on the spherical block for both tests. The responses of the mesh models are almost identical before the force drops around 260 mm. The force gradually increases exponentially as the displacement increases. This is expected because both models adopted the same force-displacement curve for one single wire. The force suddenly drops at around 260 mm because mesh wires rupture. Both mesh models were able to capture the phenomenon in which the mesh still could resist the block after some wires rupture. The differences after wires rupture were caused by the difference in how the meshes were modelled and how the wires broke in the mesh.

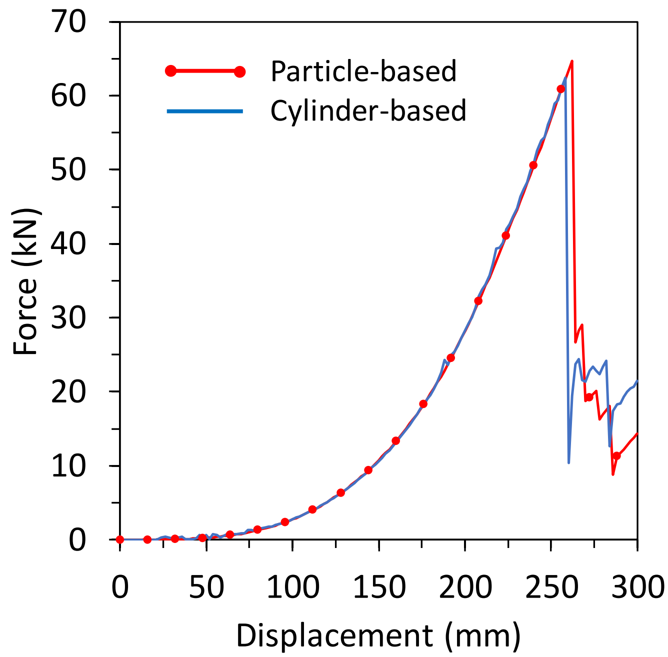

Figure 3.24 Comparison between force-displacement curves using particle-based versus cylinder-based approaches

It is important to understand the computational cost to choose a more efficient modelling approach because the mechanical response of the two mesh models was similar. In order to facilitate the comparison of the efficiency of two approaches, both models were tested on the same computer with a quad-core Intel Core i5-6300HQ CPU with 2.3 GHz and 4 GB ram. The settings in both models were also the same, such as the loading velocity (0.1 m/s), fixed time step (2×10^{-5} s) and the number of time steps (150,000 steps).

Figure 3.25 shows the computational time for the two mesh models and the proportion of each algorithm phase. The time to complete the modelling for the cylinder-based model was about 2.7 times than the particle-based model (417s versus 152s). This is due to the number of elements in the cylinder-based model is more than the particle-based model (4721 versus 1613). The proportions of relative time cost in different calculation phases are similar in both models. The only differences were that the cylinder-based model took more time in the interaction analysis phase compared to the particle-based model (71% versus 62%), whereas the particle-based model took more time in solving equations of Newton's second law than the cylinder-based model (32% versus 23%).

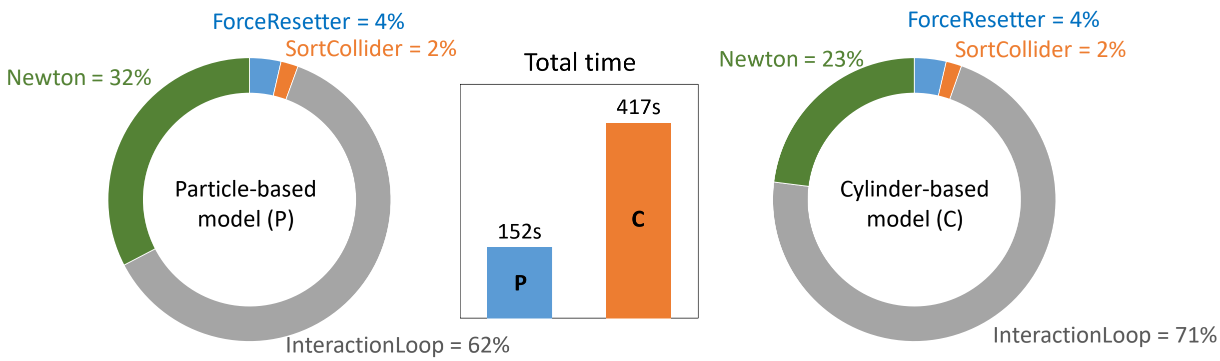

Figure 3.25 Comparison of computational time for different phases in DEM simulation

Both particle-based and cylinder-based mesh models can provide a similar mechanical response of steel mesh in terms of interacting with other objects whose size is larger than the aperture opening size in the mesh. Although the cylinder-based mesh model can simulate a more realistic interaction between the mesh and other objects because the "wires" actually exist in the model, the difference is negligible if the mesh is interacting with a large object, such as a large rock block. However, the cylinder-based approach is more computationally intensive compared to the particle-based mesh model because more elements are needed to generate the same mesh area. For the above reasons, the particle-based mesh model was chosen for the rest of the research.

3.5.4 Calibration and validation of the steel mesh model

The particle-based mesh model was calibrated and validated with published tensile and punch test results on TECCO G65/3 steel mesh (Castro-Fresno 2000, Cala et al. 2012). As mentioned in Section 3.5.1, the parameters λ_u and λ_F need to be calibrated to match the mechanical response of the physical mesh.

3.5.4.1 Calibration with laboratory tensile tests

The data from laboratory tensile tests by Cala et al. (2012) were used to calibrate the two shift parameters (λ_u, λ_F) in the wire mesh model. The tensile tests were performed on a 1.08 × 1.00 m section of mesh that was loaded in the longitudinal direction. The lateral boundaries of the mesh could slide along the test frame. The size of the numerical wire mesh model and the boundary conditions were the same as the laboratory experiments. Figure 3.26 shows the numerical tensile model configuration. During the simulation, a constant velocity of 0.01 m/s was applied to the particles at the upper boundary of the model. The time step was set to 2×10^{-5}. This setting allows the mesh model to deform gradually and fulfills a quasi-static loading process. The simulation process was stopped when the first wire in the model breaks.

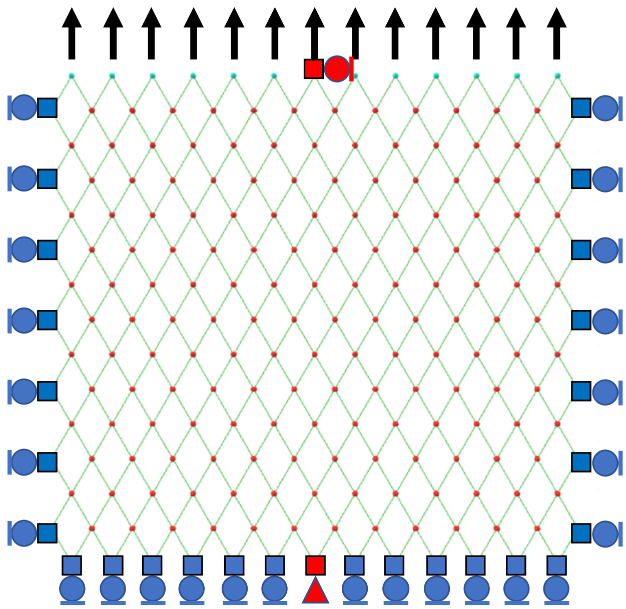

Figure 3.26 Numerical tensile test boundary conditions

To assess the influence of the shift parameters (λ_u, λ_F) on the response of the steel mesh model, a series of simulations was conducted using various combinations of λ_u (0.06, 0.08, 0.1, 0.12, 0.14) and λ_F (0.2, 0.4, 0.6, 0.8, 1.0). The range of λ_u is limited to 0 to 0.14 because a λ_u larger than 0.15 will cause a mesh model deformation much larger than the real mesh. There are 25 possible combinations of λ_u and λ_F, and the simulations were repeated ten times for each combination to account for the response variability associated with the stochastic model. The values of the parameter $\tilde{n}$ were randomly generated between 0 and 1 in these simulations. To examine the effect of the shift parameters, the displacement at failure and the peak force of the steel mesh were recorded. These are shown in Figure 3.27.

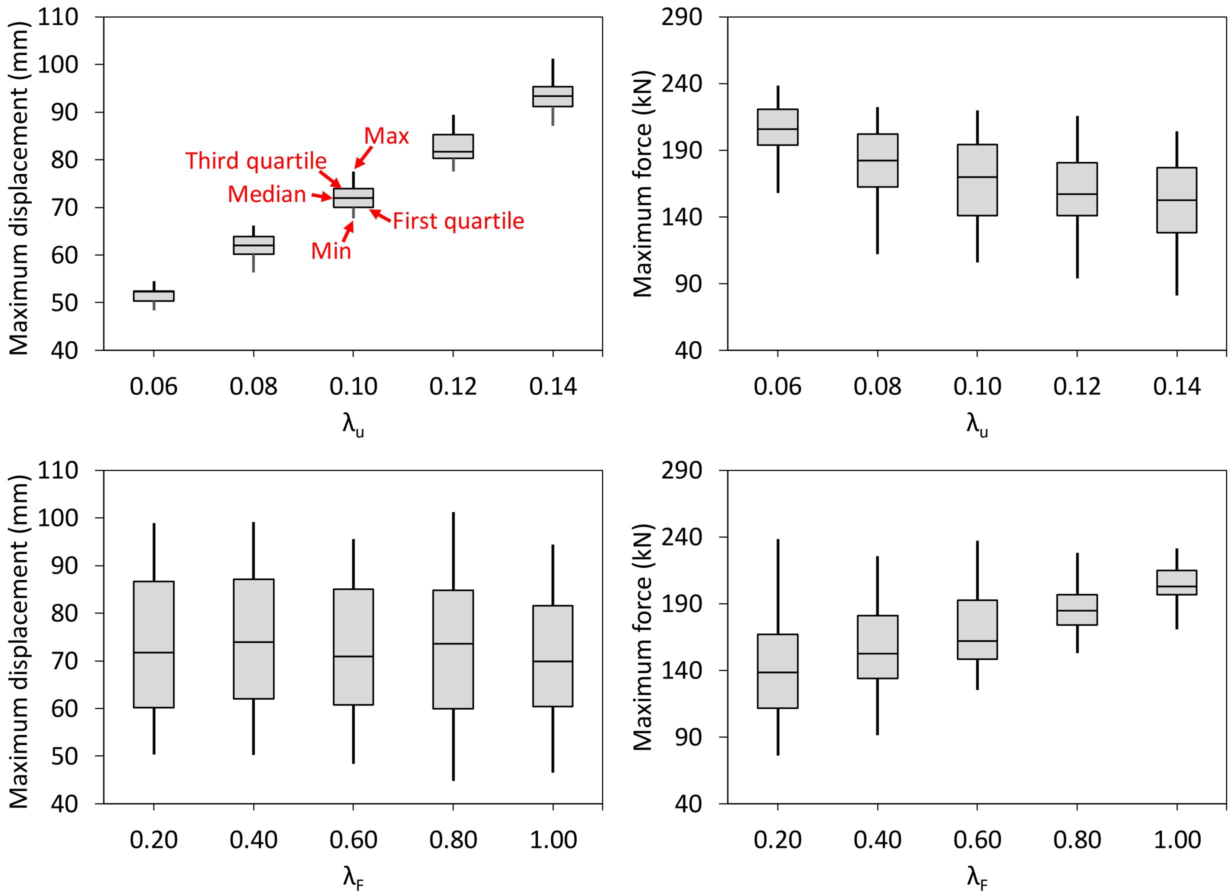

Figure 3.27 Box plots showing the effect of λ_u and λ_F on the maximum displacement and force

The influence of λ_u on the maximum displacement is significant, and the maximum displacement increases as the value of λ_u increases. The parameter λ_u also has a slight effect on the maximum force; the force decreases as λ_u increases. Although λ_F does not affect the displacement when the steel mesh model fails, the average peak force increases as the value of λ_F increases.

In the experimental tensile tests on the mesh, the peak load was approximately 168 kN, and the maximum elongation was approximately 60 mm when the mesh failed (Cala et al. 2012). From the statistical analysis in Figure 3.27, a set of parameters to match the experimental tests was determined as $\lambda_u = 0.08$ and $\lambda_F = 0.8$.

The set of λ_u and λ_F was used in 10 numerical simulations with the parameter $\tilde{n}$ randomly generated in the model. Figure 3.28 shows the mean values and standard deviations of the force-displacement response from 10 numerical tensile simulations. Figure 3.28 also shows the force-displacement relationship of steel mesh from three experimental tensile tests. The force-displacement response of the mesh model is close to the experimental data, but it is more linear.

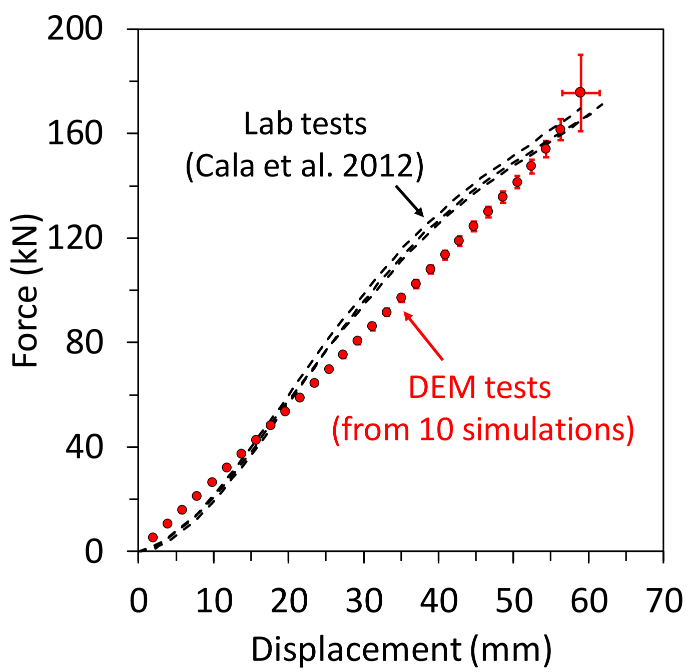

Figure 3.28 Calibration results of wire mesh DEM model with laboratory tensile tests

3.5.4.2 Validation with laboratory punch tests

In the field, the mesh is usually loaded in a direction roughly normal to the mesh panel. Therefore, it is necessary to investigate whether the linear tensile response in the mesh model will affect the response when it is loaded in the direction normal to the mesh panel. For this purpose, this study used laboratory punch tests conducted by Castro Fresno (2000) and compared the force-displacement response of the steel mesh.

As described by Castro Fresno (2000), the punching tests used two rigid steel frames bolted together. The mesh size used in the punch tests is 1 × 1 m. The mesh was fixed and held by the friction between the two frames and the shear stress on the bolts to restrict mesh movement during the tests.

A ‘spike plate P33’ (330 × 190 mm) was placed in the centre of the mesh. A hydraulic cylinder was used to load the spike plate in the direction perpendicular to the mesh plane. The loading forced the mesh to deform until some wires ruptured. During the tests, the load applied by the jack and the displacement of the mesh were recorded simultaneously.

The numerical model is shown in Figure 3.29. The steel mesh model is 1.08 × 1.00 m, and all the particles on boundaries were set to be fixed. A model of a ‘spike plate’ (330 × 190 mm) was created by rigid facet elements and was placed in the centre of the mesh to deform the mesh a constant velocity v in a direction perpendicular to the mesh plane. The simulation stopped when the first ‘wire’ in the model ruptured. The interaction between the steel mesh and spike plate was controlled by the normal stiffness k_n, the ratio between shear stiffness and normal stiffness k_s/k_n, and the friction angle ϕ. Different v, k_n, k_s/k_n, and ϕ values were tested to investigate their influence on the response of the mesh model. The other settings were kept identical when changing the target variables.

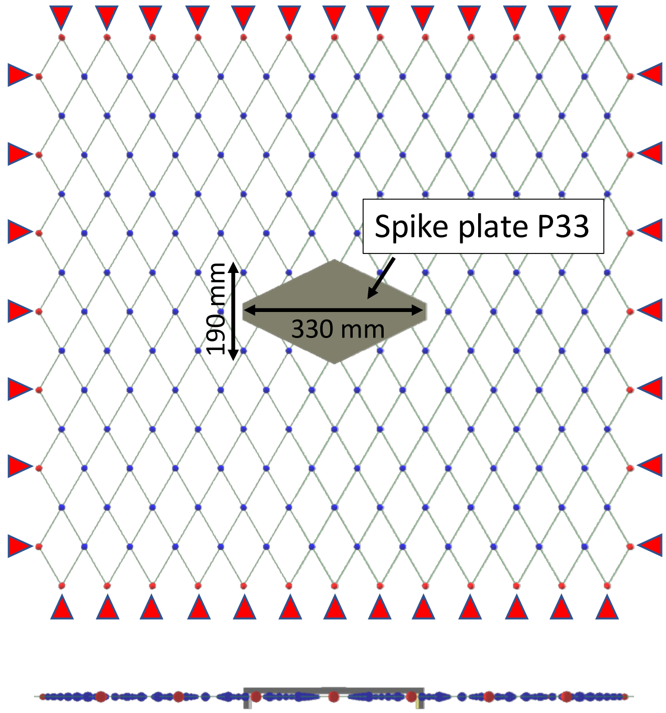

Figure 3.29 Numerical punch test in the direction perpendicular to the wire mesh

As shown in Figure 3.30a, c and d, the v, k_s/k_n and ϕ were found to have a minimal effect on the modelling results. A high k_n may cause mesh particles to vibrate in the model, which causes the fluctuation in the force-displacement response of steel mesh (blue curve in Figure 3.30b). In contrast, a low k_n may let particles passing through facet, which results in a soft mesh response (red curve in Figure 3.30b).

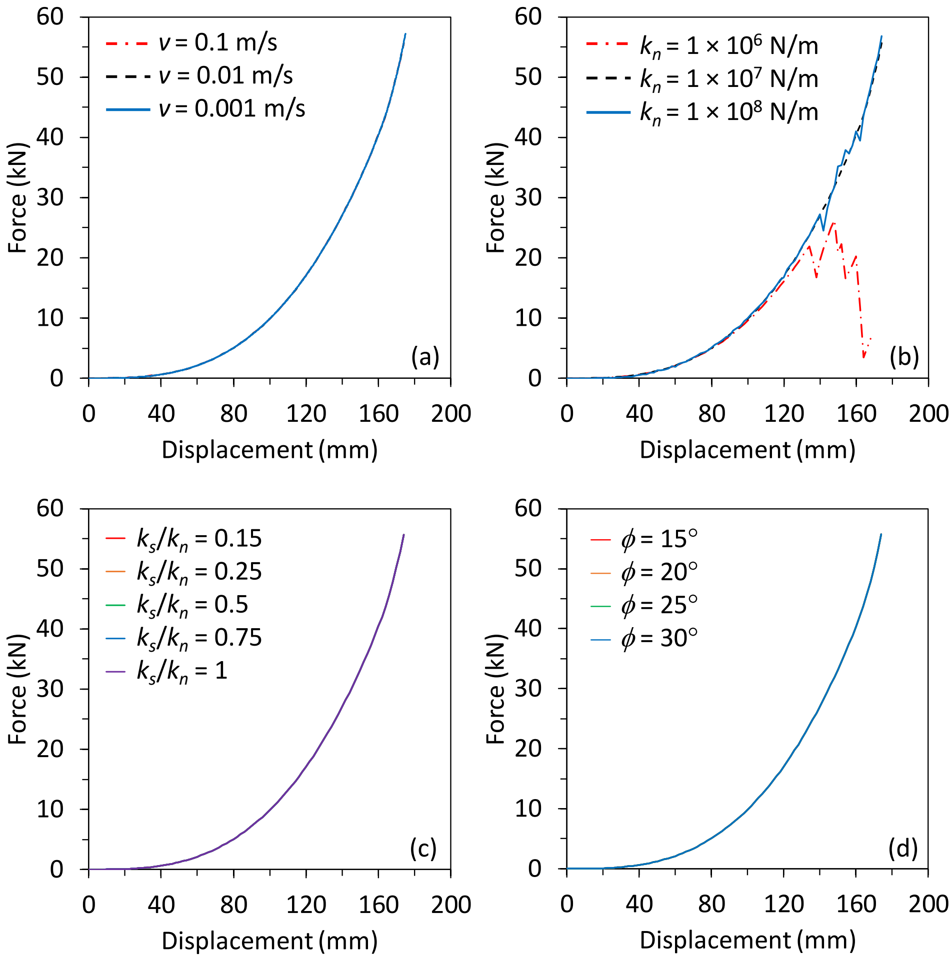

Figure 3.30 Influence of v, k_n, k_s/k_n, and ϕ on the force-displacement response of mesh model

The following parameters were found to work well: $v = 0.01$ m/s, $k_n = 1 \times 10^7$ N/m, $k_s/k_n = 0.15$, and $\phi = 30°$. A friction angle of 30° is higher than the friction angle for a smooth steel-steel contact. However, the selected friction angle accounts for the uneven surface of the spike plate that impedes the slip of wires beneath the plate. Similar parameters were used by Thoeni et al. (2013, 2014).

The force-displacement curves from three experimental and three DEM tests are shown in Figure 3.31. The simulation stopped when the first 'wire' in the model ruptured. In the laboratory tests, the mesh was already slightly stretched before the tests started because of the weight of the mesh and the loading devices, and the load on the mesh was approximately 1.6 kN when the tests began

(Castro-Fresno 2000). To facilitate a comparison with the laboratory test data, the start points of the force-displacement curves from the numerical tests shown in Figure 3.31 were set to when the force applied by the spike plate was 1.6 kN. The response of the mesh model generally matches the response of the steel mesh in the punch tests. The response of the numerical model becomes stiffer than the real mesh after about 100 mm deformation. The mesh model results in a peak load and a peak displacement that is roughly 20% small than what was observed in the laboratory tests. These differences largely occur after wires begin to rupture. This thesis focuses on the mesh behaviour up to the point of the first wire rupture, and thus the mesh model does a good job of capturing the force-displacement response of the mesh.

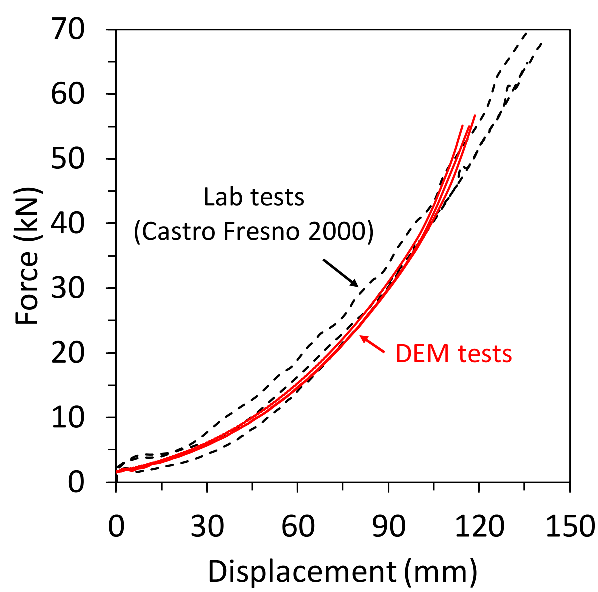

Figure 3.31 Load-displacement response of steel mesh from DEM and laboratory punch tests

There are a few possible reasons for the differences between the numerical and laboratory results in Figure 3.31. The mesh model is stiffer than the physical mesh in the transverse direction. The physical mesh has a loose connection at each node where two wires bend around. In the mesh model, four virtual springs are connected at each node. It is difficult for this mesh model to capture the large difference in the mesh stiffness in both directions. Another reason is that the mesh may slide in the laboratory tests, while the mesh boundaries are all fixed in the modelling. The third reason is that the simulated loading plate is rigid. The rigid loading plate in the numerical simulations also makes the force-displacement response in the model stiffer than the physical tests.

The numerical modelling captures the failure location of mesh wires in the laboratory tests, as shown in Figure 3.32. In both tests, the mesh wire fails close to the right side of the loading plate. In Figure 3.32a, the load is applied to the six particles that contact with the loading plate, and then the load is transferred to the mesh boundaries through the aligned mesh wires. The mesh wires that are aligned to the particles underneath the left and right corners of the loading plate carry the largest load. The wire next to the right side of the loading plate reaches its ultimate strength and ruptures first. The wire rupture causes a load redistribution in the mesh. The numerical simulation demonstrates the load transfer mechanism for the laboratory tests. As can be seen in Figure 3.32b, the wire ruptured at a wire bend because of stress concentration at the bends. In the modelling, the wire rupture is represented by removing the virtual link where the wire fails.

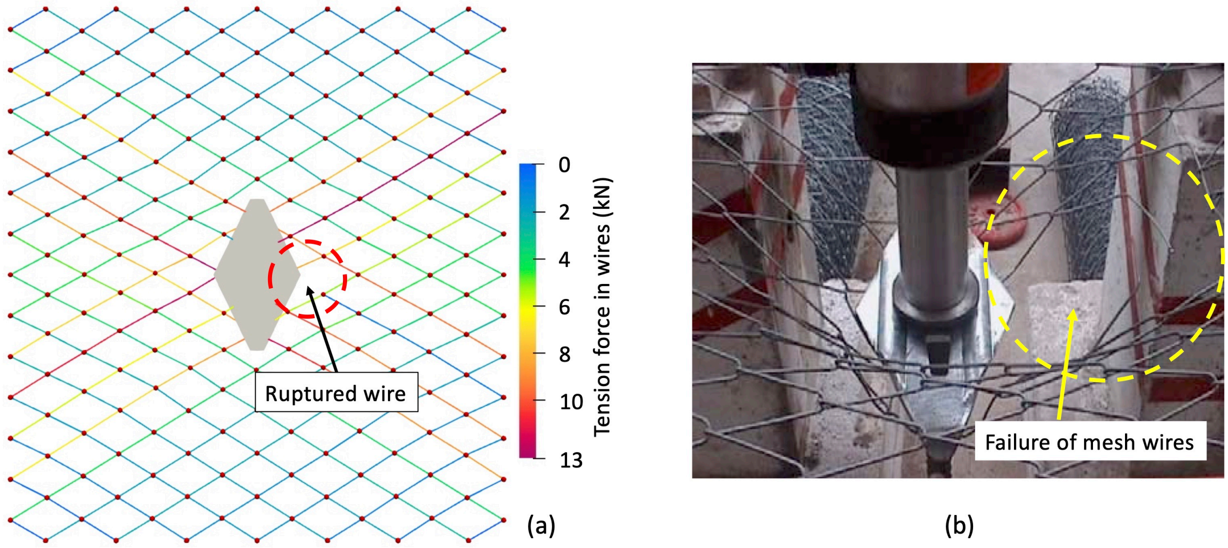

Figure 3.32 Comparison between DEM punch test and laboratory test (a) tensile force distribution in wires showing ruptured wire in DEM simulation; (b) failure of mesh wires in the laboratory test after Castro Fresno (2000) (used under Creative Commons Attribution 3.0 Spain)

It is worth noting that when simulating the interaction between the mesh and rockbolt plate, the plate only interacts with the particles at each node. In the lab tests, the plate interacts with both physical mesh wires and the nodes in the mesh. The mesh wires may experience bending during the loading. Although the bending of wires is not simulated, the mesh model can simulate the mechanical response of physical mesh in the punch tests, including force-displacement response and mesh failure mechanism. Therefore, the bending of mesh wires has a minor influence on the global mesh behaviour.

3.6 Summary

This chapter presents three modelling approaches in the open-source discrete element software YADE to simulate the steel wire mesh. One approach used connected cylinder elements to model a steel wire in the mesh. A beam-like contact law was applied in the model. The spherical particles between each cylinder element act like an elbow and thus allow the wire model to bend. Simple models of wire and small sections of wire mesh were created to show that the models can represent the behaviour of the high-tensile wire and the wire mesh. The wire model currently only simulates the elastic behaviour of the wire and does not account for the plastic deformation. If the problem to be modelled is primarily concerned with the elastic response of the mesh and the complex load transfer mechanisms and deformations of hooked bent wires oriented in different directions, the mesh model does a good job at capturing the phenomena. However, the simulated elongation of a single wire is estimated to be 50% less than the real wire, which will result in a stiffer response when modelling a steel mesh. Also, this modelling approach is computationally intensive. Nevertheless, the proposed mesh model can simulate the large differences in the strength and stiffness of mesh loaded in the longitudinal versus the transverse direction. A rockbolt plate loading test was conducted to show the deformed shape and failure mechanism of the mesh.

The other two modelling approaches, named particle-based approach and simplified cylinder-based approach, applied the stochastically distorted wire model to simulate the steel wire mesh. These two approaches have fewer elements to create the same mesh size compared to the detailed cylinder-based approach. Numerical simulations were conducted to compare the modelling performance in terms of their mechanical response and computational cost for the two modelling approaches. The particle-based modelling approach was found to be less computationally intensive than the cylinder-based approach and can provide an equivalent result on the mechanical response of steel mesh when the mesh interacts with other objects. The particle-based modelling approach was chosen to perform the simulations for the remainder of the thesis.

The particle-based mesh model was then calibrated and validated using the published results from the experimental tensile and punch tests. Although the bending resistance of wires is not considered in the model, using the stress-strain relationship of the wire and calibration of 'shift parameters' allows the mesh model to capture the tensile and punching behaviour of the physical steel mesh. The mesh models of tensile tests behaved more linearly than the steel mesh in the experimental tests. However, the response of the mesh models had a good match with experimental punch tests when the loading is perpendicular to the mesh panel, which is consistent with the common loading direction in the field.

Chapter 4: Discrete element analysis of the influence of bolt pattern and spacing on the force-displacement response of bolted steel mesh

4.1 Overview

Steel wire mesh is usually held by a pattern of bolts to stabilize a rock slope. Knowledge of the force-displacement response of steel mesh is essential in the design of this support system. Laboratory tests have been used to test mesh that is held to rigid steel frames. These testing conditions differ from how steel mesh is held in the field by bolts. The response of steel mesh in the laboratory or the field is affected by how the mesh is held or pinned to the rock due to the different boundary conditions. The existing laboratory test data may underestimate the deformation and overestimate the load-bearing capacity of the steel mesh. This chapter focuses on the response of the high-tensile steel mesh held by commonly used bolt patterns. The mesh calibrated to the properties of TECCO G65/3 in Section 3.5.4 was used for all simulations.

Section 4.2 presents the simulated steel mesh response for a model of the fixed frame punch test based on the recent ISO 17746 mesh testing standard. The results from this simulation were compared with simulations of mesh pinned by bolts at two different patterns. This comparison is presented to justify the need to better represent the field response of mesh by simulating the presence of bolts and not a fixed, rigid boundary.

Section 4.3 and Section 4.4 show the effect of bolt spacing on the response of steel wire mesh at deformations below 0.5 m held by bolt pattern A and pattern B, respectively. The purpose is to analyze the effectiveness of the steel mesh with various ratios between vertical and horizontal bolt spacing for different bolt patterns.

Section 4.5 compares the effectiveness of high-tensile steel mesh with bolt pattern A and pattern B. In addition, relationships between the resistance force of steel mesh and bolt density at various mesh deformations were established to help guide the design of bolted steel mesh.

4.2 DEM punch tests on steel mesh with various boundary conditions

4.2.1 DEM models for punch tests

Three different numerical models of mesh were constructed. Model 1 consisted of a fixed boundary model built from 1612 particles to represent the ISO 17746 test standard, in which a 3×3 m^2 area of the mesh was tested (Figure 4.1a). The particles along the outer boundary were fixed to simulate the effect of the steel frame used in the ISO 17746 standard.

Model 1 was compared with two different numerical punch test models of steel mesh held by simulated rockbolt plates. Model 2 used bolt pattern A and Model 3 used bolt pattern B, as shown in Figure 4.1b and Figure 4.1c, respectively. For a comparison with Model 1 results, the horizontal (H) and vertical (V) spacing of the bolts was set to 3×3 m for pattern A, and 3×1.5 m for pattern B. The vertical spacing of bolts V is the distance between adjacent rows of bolts, as shown in Figure 4.1.

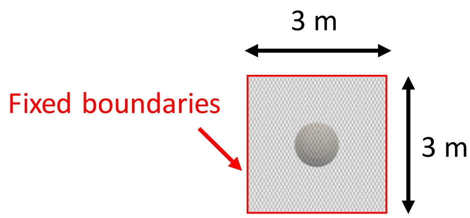

(a) Model 1 (fixed boundaries)

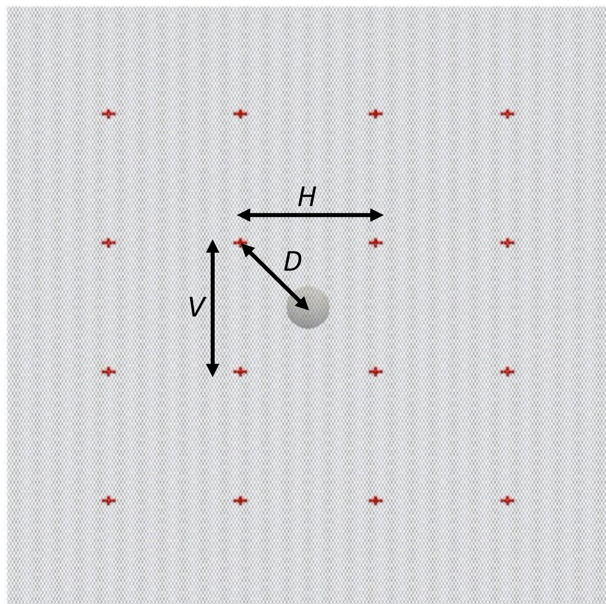

(b) Model 2 (pinned by Pattern A)

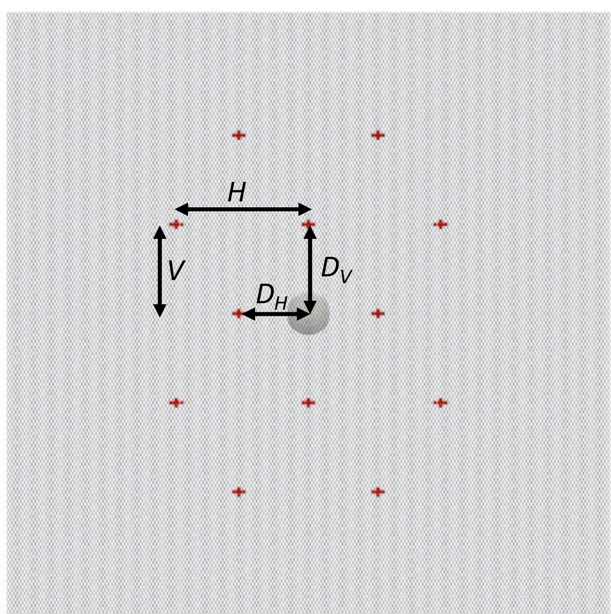

(c) Model 3 (pinned by Pattern B)

Figure 4.1 Numerical models of punch tests

Models 2 and 3 were constructed from 33391 particles to simulate a 14 × 14 m^2 area of mesh with free boundaries. The effect of plates on bolts holding the mesh was modelled by fixing the movement of six particles in all directions that would have been in direct contact with 330 × 190 mm spike plates. This simplification may make the mesh model stiffer than the real mesh. The size of the particles that represent the plates was exaggerated to show their locations in Figure 4.1. There were 16 and 12 simulated plates for each bolt pattern, respectively. It is difficult to set the same number of bolts for each model because of the different bolt patterns. The number of bolts only has a minor influence on the deformation response.

For all models, a simulated hemispherical punching device was used to load the mesh. The device was constructed from triangle facet elements. The device has a radius of curvature 1.2 m and a diameter of 1 m projected on a plane (Figure 4.2). The punch device was placed in the centre of the mesh. The interaction between the steel mesh and the punch device used the same stiffness and friction angle parameters used in Section 3.5.4.2.

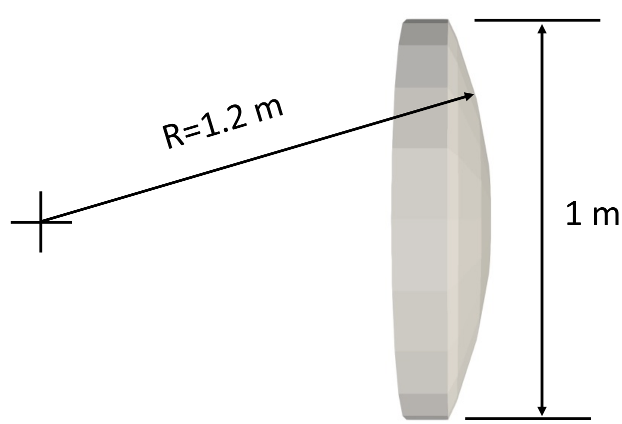

Figure 4.2 Numerical model of the punch device

A constant velocity was applied to the punching device to load the steel mesh in a direction perpendicular to the mesh panel until the first wire in the mesh model failed. The combination of the velocity and time step ensures a stable simulation process with quasi-static loading. Typically, 50,000 calculation cycles were required to move the punching device 0.5 m.

The maximum loads plotted in the force-displacement curve correspond to the point at which the first wire in the model breaks. The mesh may be able to carry higher loads with subsequent displacement of the punching device, but this was not simulated.

4.2.2 Results of DEM punch tests with different boundary conditions

The force-displacement responses of steel mesh determined using the three different models are shown in Figure 4.3. Model 1 gave the highest peak load (160 kN). The maximum force carried by the mesh decreases to 65 kN and 87 kN for Models 2 and 3, respectively. The first wire to break for the fixed boundary test occurred at the edge of the punching device. In contrast, the first wire to break in the pinned mesh occurred at a simulated rockbolt plate for all models presented in this chapter.

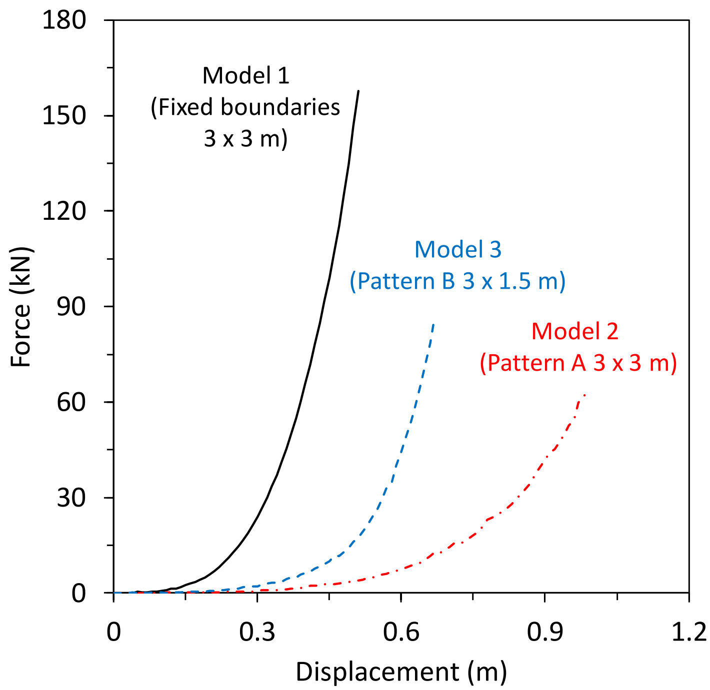

Figure 4.3 Force-displacement responses of steel mesh for the three models

The force-displacement response of the punching device became more deformable when the mesh was pinned compared to a fixed outer boundary. The mesh in the centre of Model 1 was able to deform 0.5 m. For Model 2 and Model 3, the maximum deformation of the steel mesh in the centre was 0.99 m and 0.66 m, respectively. The testing boundary conditions significantly influence the response of steel mesh. The laboratory and field tests on the double-twisted wire mesh also show the same trend (Bertolo et al. 2009, Grimod and Giacchetti 2014). It should be noted that the mesh in Model 3 is stiffer than Model 2. The reason is that the distance from the nearest bolts to the centre of the punch device in Model 3 is smaller than Model 2 (1.5 m vs. 2.1 m).

It is important to recognize the number of wires that carry loads when interpreting laboratory test data. Tests with fixed boundary conditions, varying mesh areas, and varying sizes of the punching device can result in far more wires carrying the loads than under field conditions with mesh held by bolts. The laboratory data may indicate that larger mesh areas create higher load capacities, but this does not reflect the reality of how mesh carries the load in the field. The results from punch tests with a fixed frame will likely underestimate the deformation and overestimate the load capacity of the steel mesh in the field.

For reasons above, the remainder of this chapter focuses on mesh supported by bolts because these results are more applicable to field conditions. The mesh's force-displacement response is sensitive to how it is pinned to the rock surface. The influence of bolt pattern, bolt spacing, and the ratio of the vertical to horizontal bolt spacing is presented in the next three sections.

4.3 Effect of bolt spacing with bolt pattern A

A full factorial design approach (Montgomery 2017) to numerical modelling was used to develop a series of simulations by varying the horizontal and vertical bolt spacing from 2 to 4 m in 0.5 m intervals for pattern A. The force-displacement curves for all combinations of bolt spacing are shown in Figure 4.4. The mesh resistance force increases in an exponential manner with mesh displacement. The peak force that the mesh can carry is approximately 50 to 70 kN, and the peak is not very sensitive to the bolt spacing. The peak force is fundamentally a function of the number of wires running from the punching device to adjacent plates. By contrast, a larger bolt spacing will result in a larger maximum displacement.

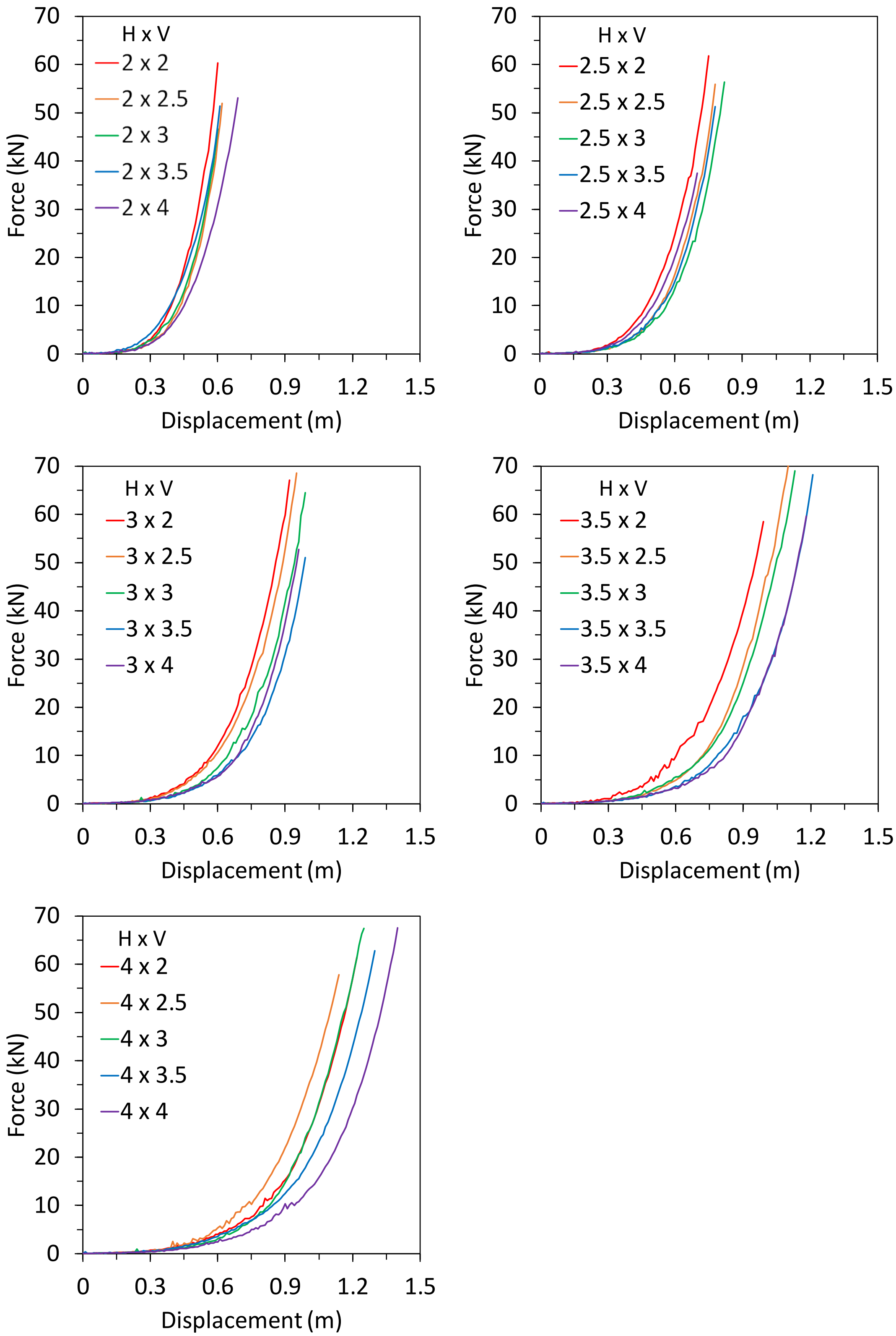

Figure 4.4 Force-displacement response of steel mesh with bolt pattern A

The data plotted in Figure 4.5 were truncated at a maximum displacement of 0.5 m. The reason for truncating these curves is that the focus of this chapter is on assessing the mobilization of resistance force by the steel mesh at deformations less than 0.5 m, which are more likely to be of relevance in engineering practice.

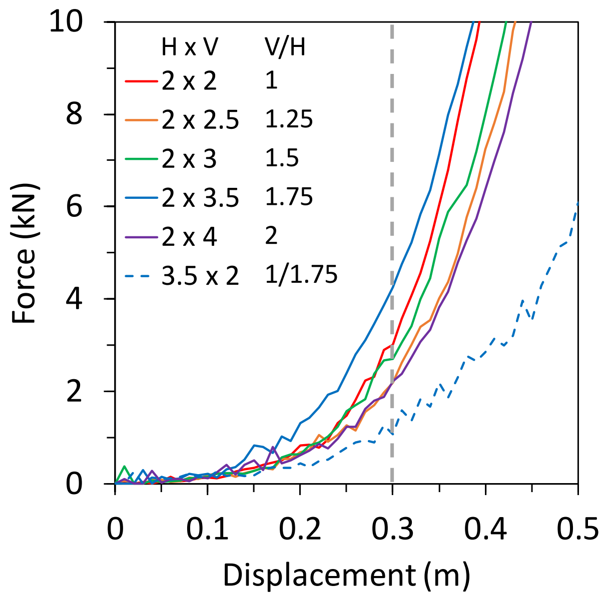

Figure 4.5 Effect of vertical and horizontal bolt spacing on the force-displacement response of mesh with bolt pattern A

Figure 4.5 shows the results when the vertical spacing of the bolts increases from 2 to 4 m with a constant 2 m horizontal spacing. For comparison purposes, an extra curve was added to Figure 4.5 to show the response of steel mesh with bolt horizontal spacing of 3.5 m and vertical spacing of 2.0 m (which is a reverse of the 2 × 3.5 m arrangement). Figure 4.5 shows that the mobilization of force takes the least deformation with a 2 × 3.5 m bolt spacing compared to the other cases. If the horizontal spacing is 3.5 m with a vertical spacing of 2.0 m, the displacement of the mesh for a mobilized load resistance of 4 kN increases from 0.29 to 0.46 m.

A 0.3 m displacement of the mesh was selected as a design threshold based on practical considerations in the field. The force mobilized perpendicular to the mesh when the mesh is displaced 0.3 m is denoted as $F_{0.3}$ and is generically called the mesh resistance force. The tensile force in the wires when $F_{0.3}$ occurs are well below the maximum allowable tensile force (12.5 kN) for all bolt spacings, as shown in the force distribution in mesh wires in Figure 4.7 and Figure 4.8.

Figure 4.6 shows the relationship between the V/H ratio and $F_{0.3}$. The mesh can carry the load more efficiently if the load from the punch device is transmitted along wires that are aligned directly between the punch device and the bolts. The distance from the centre of the punch device to the nearest four bolts is denoted as D, as shown in Figure 4.1. This geometry occurs when the nearest two rows of bolts carry the load with a V/H bolting ratio of 1.72 (equal to the mesh opening aspect ratio), as shown in Figure 4.7a. For a wider horizontal spacing, a V/H that is close to 0.58 results in an arrangement where there are mesh wires that run directly from the punching device to the bolts located two rows above and below the punch device (Figure 4.7b) and these bolts also carry a portion of the load.

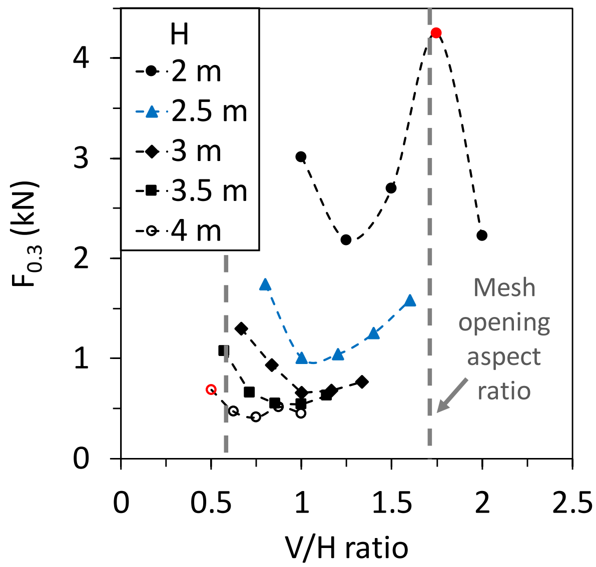

Figure 4.6 Effect of *V*/*H* ratio on $F_{0.3}$ for bolt pattern A

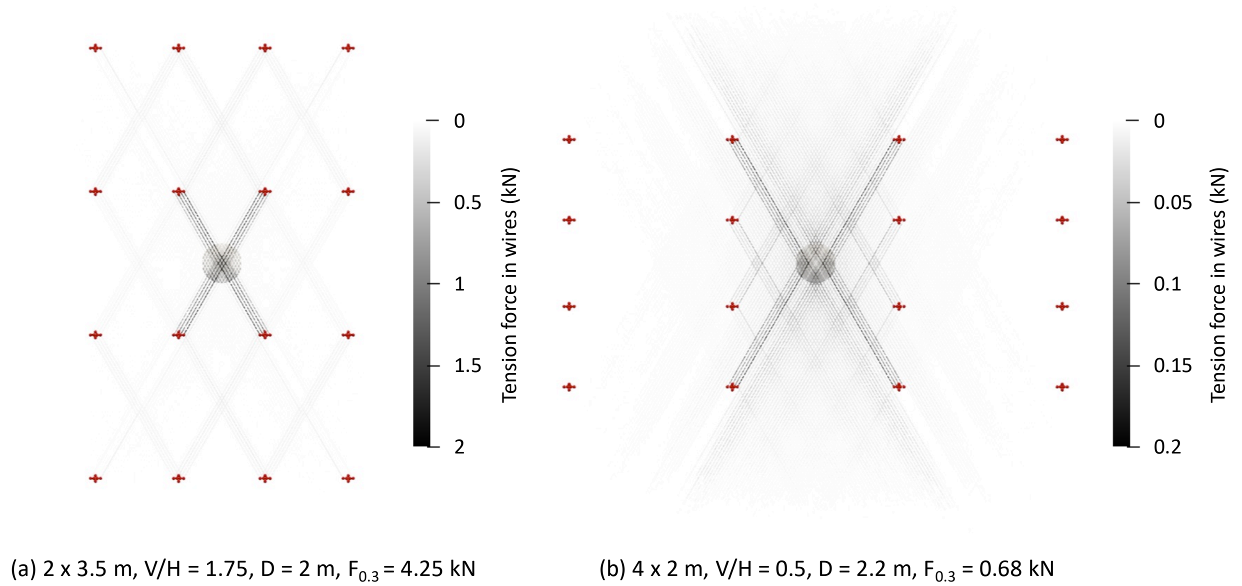

Figure 4.7 Force distribution in wires for bolt pattern A for (a) *V*/*H* = 1.75 and (b) *V*/*H* = 0.5 at 0.3 m displacement of the punch device

To further illustrate the load transfer mechanisms, Figure 4.8 shows the force distribution in the wires when the punch device moved 0.3 m for a horizontal bolt spacing of 2.5 m and different *V*/*H* ratios. As the *V*/*H* ratio decreases from 1.6 to 1 (Figure 4.8a to c), $F_{0.3}$ decreases even though the number of bolts that carry the load increases. With a further decrease in V/H to 0.8, the mobilization resistance force increases because the nearest bolt is closer to the punch device, and the bolts located two rows above and below the punch device begin to carry a substantial portion of the load (Figure 4.8d).

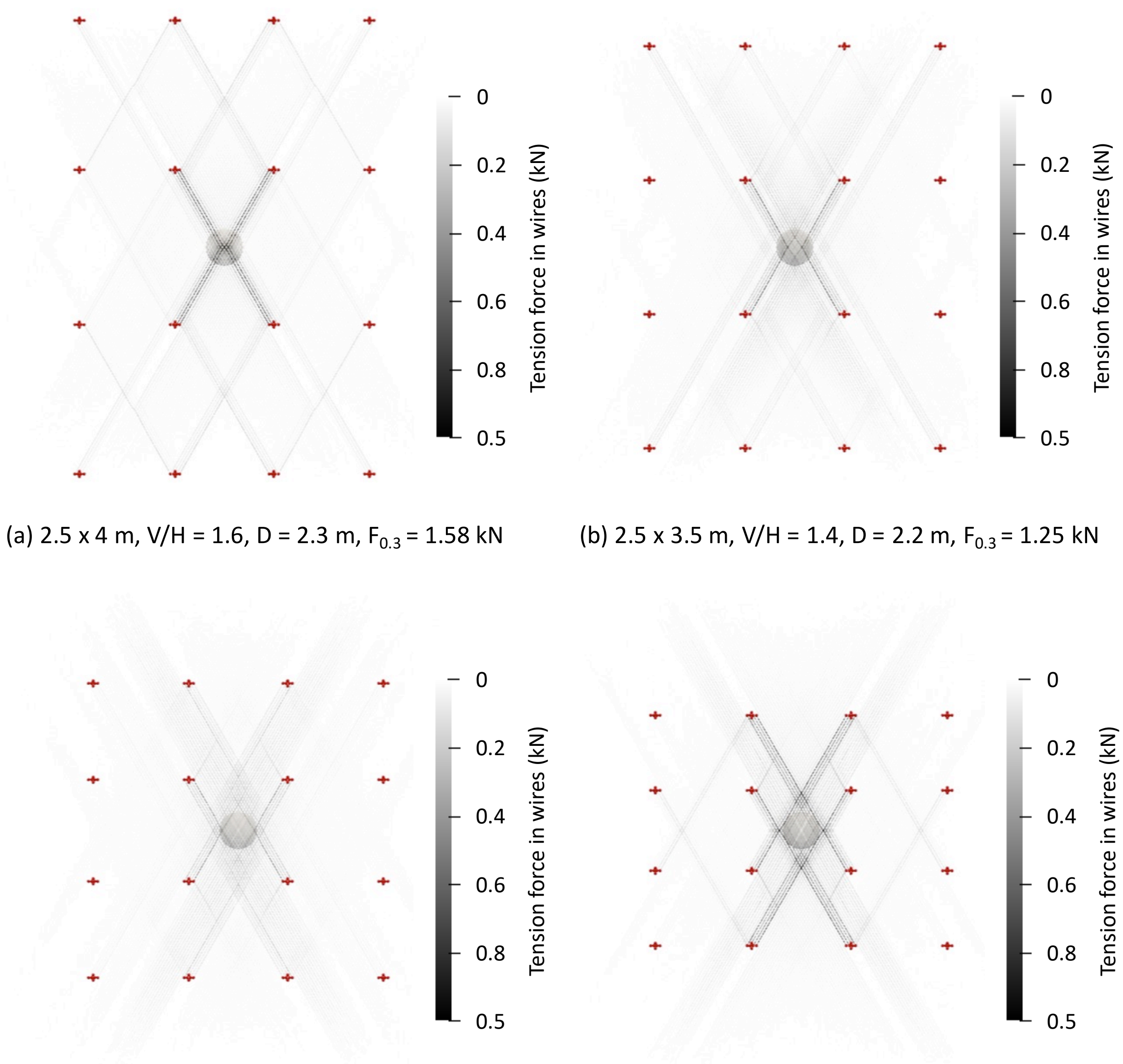

(a) 2.5 x 4 m, V/H = 1.6, D = 2.3 m, $F_{0.3}$ = 1.58 kN

(b) 2.5 x 3.5 m, V/H = 1.4, D = 2.2 m, $F_{0.3}$ = 1.25 kN

(c) 2.5 x 2.5 m, V/H = 1, D = 1.8 m, $F_{0.3}$ = 1.04 kN

(d) 2.5 x 2 m, V/H = 0.8, D = 1.6 m, $F_{0.3}$ = 1.74 kN

Figure 4.8 Force distribution in wires for bolt pattern A with a horizontal bolt spacing of 2.5 m and different *V*/*H* ratios at 0.3 m displacement of the punch device

Figure 4.9 shows the influence of distance from the nearest bolt to the punch device on the mesh resistance force when the displacement of the punch device is 0.3 m. The mesh resistance force shows a decreasing trend as the bolt-to-load distance increases. However, $F_{0.3}$ is larger when the *V*/*H* ratio is close to the mesh opening aspect ratio compared to other *V*/*H* ratios at a similar bolt-to-load distance. Although $F_{0.3}$ for the three cases plotted within the blue ellipse in Figure 4.9 is high, the bolt densities are also higher than the cases with a *V*/*H* ratio close to the mesh opening geometry plotted within the red ellipse. Therefore, the bolted steel mesh is more effective when the bolt spacing with pattern A matches the mesh opening aspect ratio.

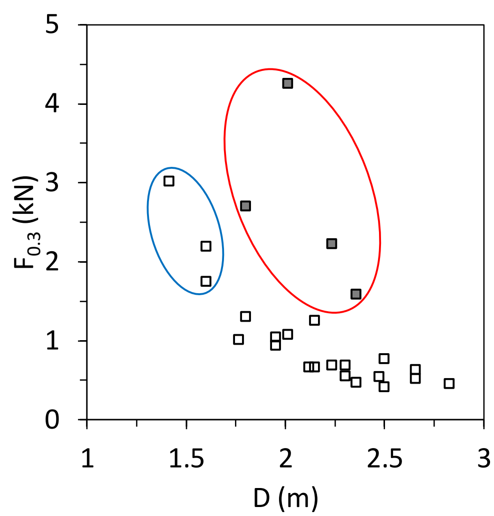

Figure 4.9 Effect of *D* on $F_{0.3}$ with bolt pattern A (grey points indicate a *V*/*H* ratio close to the mesh opening aspect ratio)

4.4 Effect of bolt spacing with bolt pattern B

Bolt pattern B is widely used in practice. A full factorial design was used to develop a series of simulations of mesh pinned by pattern B by varying the horizontal bolt spacing from 2 to 6 m in 1 m intervals and vertical bolt spacing from 1.5 to 3 m in 0.5 m intervals. These spacings were selected to facilitate a comparison of pattern B with pattern A when the distances from the bolts to the centre of the punch device were similar. The full force-displacement curves are shown in Figure 4.10. Similar to pattern A, the mesh resistance force increases in an exponential manner with mesh displacement, but there is a greater range in the mesh displacement for a given horizontal bolt spacing, and the peak force is generally higher for pattern B.

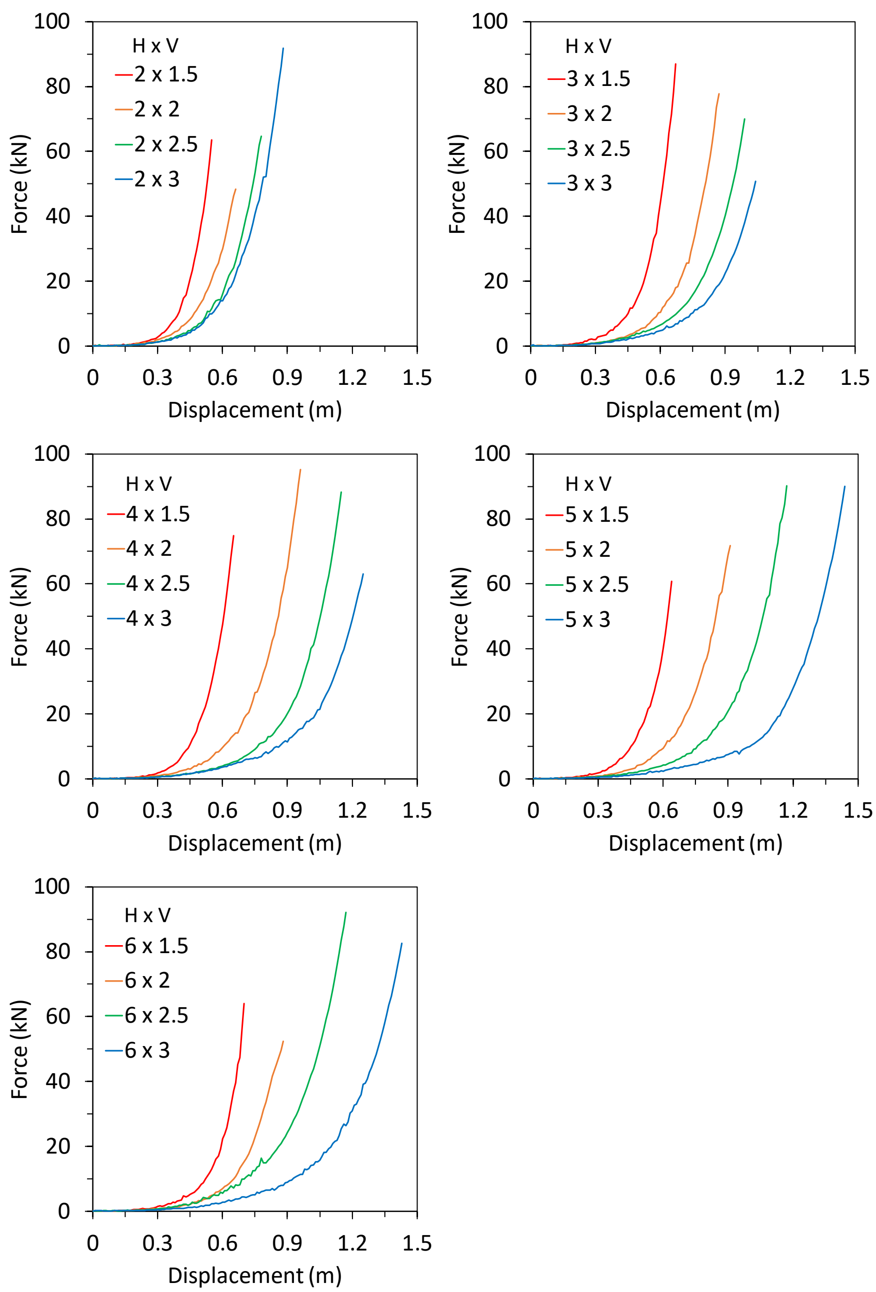

Figure 4.10 Force-displacement response of mesh with bolt pattern B

Figure 4.11 shows the simulated force-displacement response of the steel mesh with a constant horizontal spacing of 3 m. As with pattern A, we focus on the mobilization of resistance force by the steel mesh at deformations less than 0.5 m. When *H* is fixed, the mesh resistance force when the punch device reaches a certain deformation decreases as the *V*/*H* ratio increases, and as the mesh area between the nearest four bolts to the punch device increases. For pattern B, a *V*/*H* ratio of 0.86 (equal to half of 1.72 as for pattern A) corresponds to the mesh opening aspect ratio because the bolts in alternating rows are offset one half of the separation distance between the bolts. It is interesting to note that when *V*/*H* = 0.83, which is close to 0.86, the force-displacement curve is no better than curves with other ratios. For pattern B, the *V*/*H* ratio has little influence on optimizing the mesh performance.

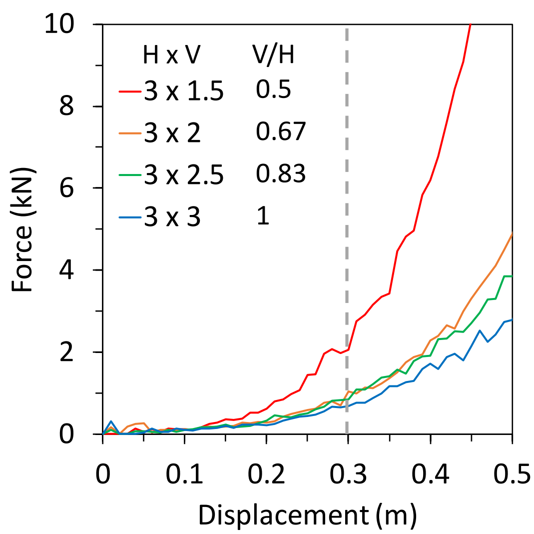

Figure 4.11 Effect of vertical and horizontal bolt spacing on the force-displacement response of mesh with bolt pattern B

Figure 4.12 further illustrates the effect of the *V*/*H* ratio on $F_{0.3}$. When the vertical spacing is constant, $F_{0.3}$ increases as the *V*/*H* ratio increases. This effect is due to a decrease in the mesh area between the nearest four bolts to the punch device. There is no peak in $F_{0.3}$ associated with a *V*/*H* ratio that matches the mesh opening aspect ratio. As shown in Figure 4.13, although the *V*/*H* ratio is close to the mesh opening aspect ratio for a 2 × 1.5 m spacing for pattern B, the forces are not carried directly from the punching device to the bolts. The wires that carry a higher load form a diamond shape surrounding the punching device with four corners at the bolt locations.

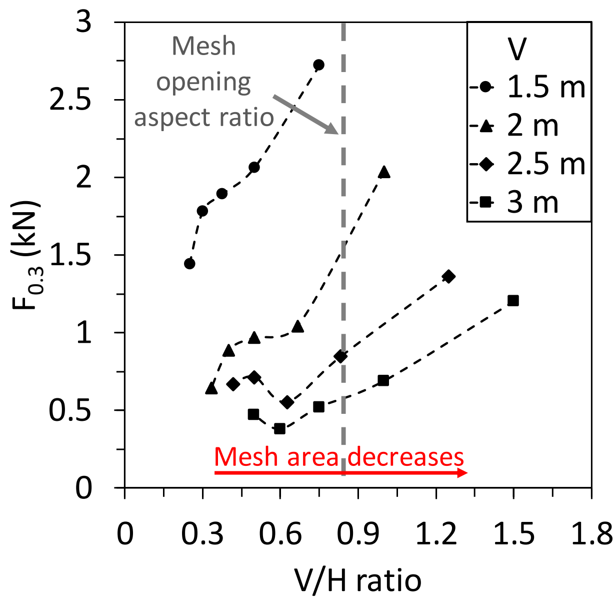

Figure 4.12 Effect of *V*/*H* ratio on $F_{0.3}$ for bolt pattern B

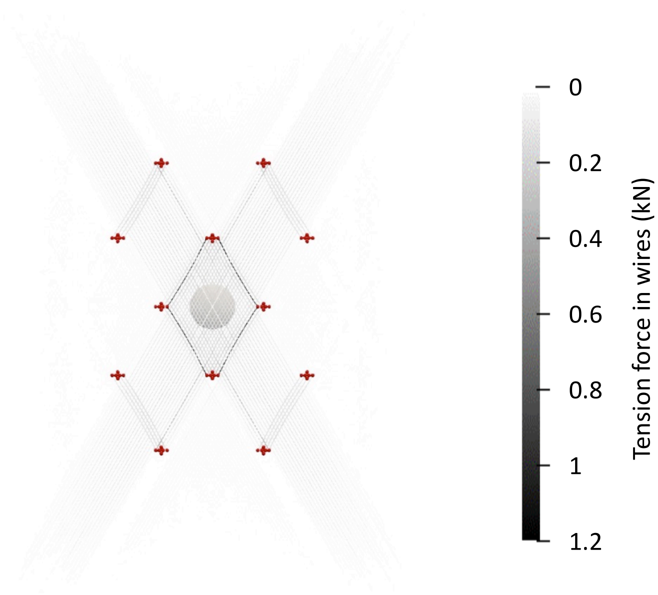

Figure 4.13 Force distribution in wires for bolt pattern B with 2 × 1.5 m bolt spacing for a 0.3 m displacement of the punching device

The horizontal and vertical spacings have more influence on the effectiveness of the mesh than the spacing ratio. Figure 4.14 shows the effect of the distance from the nearest bolts to the centre of the punch device on $F_{0.3}$. A V/H ratio that is close to the mesh opening aspect ratio does not always provide the highest $F_{0.3}$, as shown by the shaded symbols inside the red ellipses. The distance from the nearest bolt above (or below) the punch device to the centre of the punch device is denoted as D_V, and the distance from the nearest bolt on the left side (or right side) of the punch device to the centre of the punch device is denoted as D_H, as shown in Figure 4.1. The mesh resistance force decreases as D_H and D_V increase in Figure 4.14. However, the influence of D_V (Figure 4.14b) is larger than D_H (Figure 4.14a), as illustrated by the steeper slope on the curves. Thus, reducing the vertical bolt spacing is more important than the horizontal spacing in achieving better mobilization of a mesh resistance force. This is because this mesh has a diamond-like shape with the longer diagonal aligned with the longitudinal direction of the mesh enabling the mesh to carry more load in the longitudinal (vertical) direction versus the transverse direction. Also, this diamond-like mesh is much stiffer in the longitudinal direction than in the transverse direction (Xu and Tannant 2016).

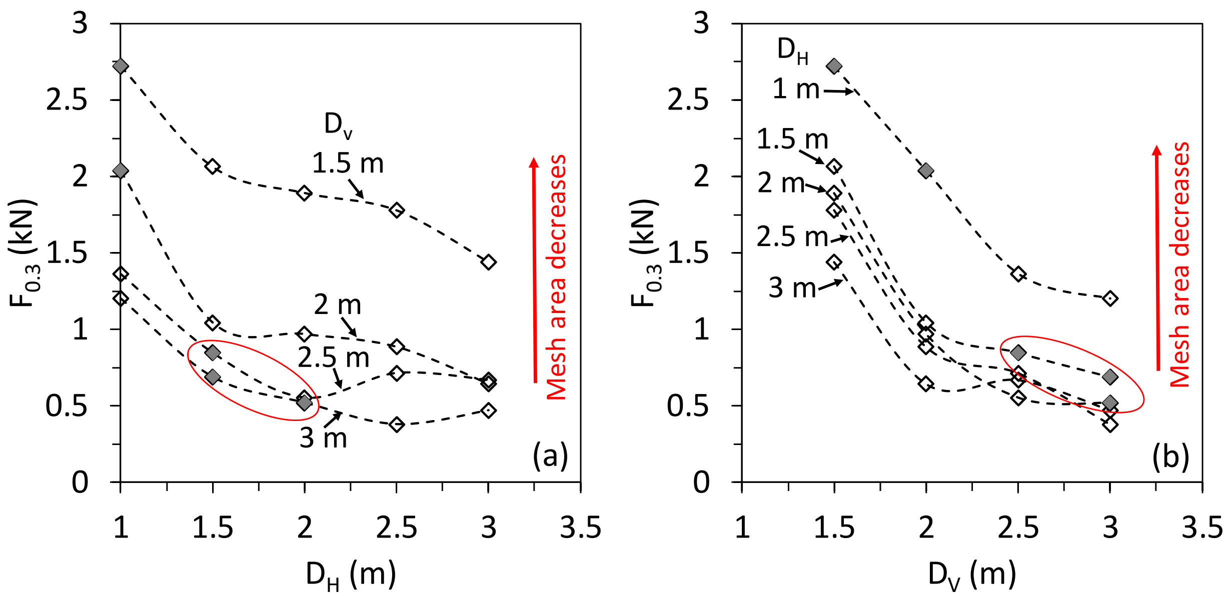

Figure 4.14 Effect of D_H and D_V on $F_{0.3}$ with bolt pattern B (grey points indicate a *V*/*H* ratio close to the mesh opening aspect ratio)

4.5 Comparison between bolt patterns and effectiveness of steel mesh

Bolt patterns A and B are widely used, but there is a lack of guidelines to help choose the proper bolt patterns and bolt spacing. This section compares the effectiveness of high-tensile steel mesh with bolt pattern A and pattern B. In addition, relationships between the resistance force of steel mesh and bolt density at various mesh deformations were established to help guide the design of bolted steel mesh.

4.5.1 Effectiveness of steel mesh with different bolt patterns

The two types of bolt patterns were compared to provide suggestions for the design of a bolted steel mesh system. Figure 4.15 shows two force-displacement curves for mesh held by a 2 × 2 m bolt spacing in pattern A and a 3 × 1.5 m bolt spacing in pattern B. These two arrangements of bolts create a similar distance (approximately 1.5 m) from the nearest bolts to the centre of the punch device. For these two bolt spacings, pattern B can be viewed as rotating the bolt arrangement in pattern A by 45°, which allows the two bolt patterns to have the same bolt density. Note that the number of bolts in the model with pattern B was less than that in pattern A (12 versus 16).

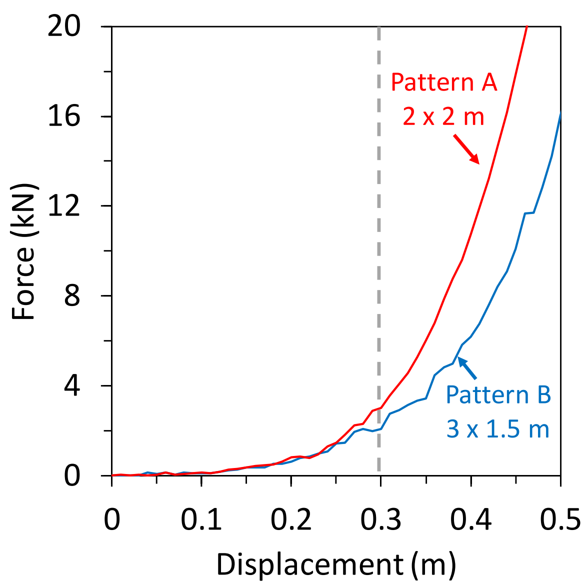

Figure 4.15 Comparison of force-displacement curves of different bolt patterns with a similar distance from the nearest bolts to the centre of the punch device

Figure 4.15 shows the mesh held by bolt pattern A is stiffer and mobilizes a resistance force quicker than pattern B. From a force transmission perspective for pattern A, the mesh mobilizes forces in the wires pinned by the four bolts above and the four bolts below the punch device, as shown in Figure 4.16a. In comparison, for pattern B, the mesh mainly mobilizes forces in the wires pinned by the three bolts above and three bolts below the punch device, with one bolt on each side carrying a minor load (Figure 4.16b). There are eight bolts involved in each of these two cases, but the mesh held by pattern A behaves stiffer and has a higher $F_{0.3}$.

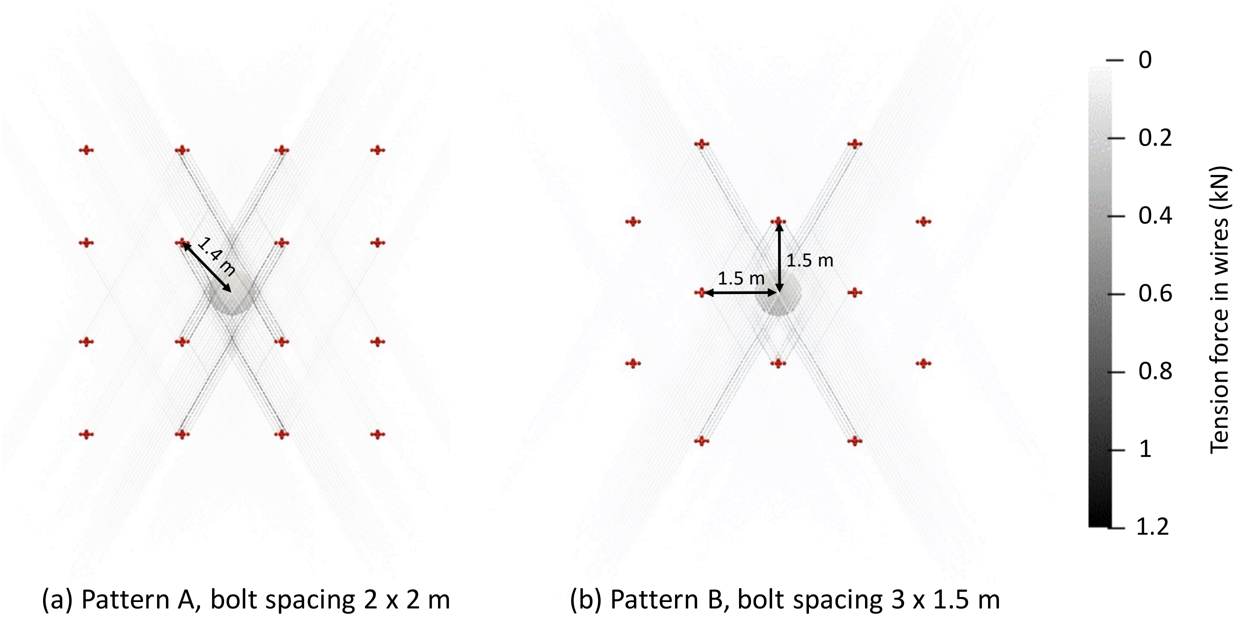

Figure 4.16 Force distribution in wires for different bolt patterns at 0.3 m displacement of the punch device

Figure 4.17 shows the results for the two bolt patterns for a range of mesh areas between the nearest bolts to the punch device. The mesh area around the punch device is considered as an indicator of the effect of the distance from the nearest bolts to the punch device. The difference between the two bolt patterns is small in terms of $F_{0.3}$ in Figure 4.17. As expected, the $F_{0.3}$ decreases as the area increases for both bolt patterns. The points in grey indicate the cases where the V/H ratio is close to the mesh opening aspect ratio. For pattern A, a V/H ratio close to the mesh opening aspect ratio and a smaller area around the punch device provide a higher $F_{0.3}$. For pattern B, placing the bolts to match the mesh's opening aspect ratio does not provide a higher $F_{0.3}$. If the bolt arrangement for pattern A is close to the mesh opening aspect ratio, the mesh performance is slightly better compared to pattern B.

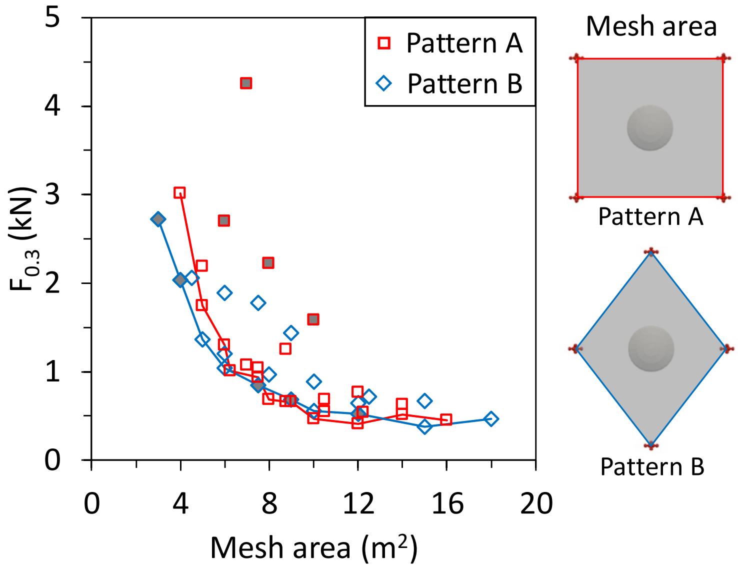

Figure 4.17 Mesh resistance force mobilized for different bolt patterns and mesh area (grey points indicate a *V*/*H* ratio close to the mesh opening aspect ratio)

4.5.2 Resistance force of bolted steel mesh at various deformations

To help guide the design of bolted steel mesh, this section establishes preliminary engineering design relationships between the resistance force of steel mesh and the mesh area for punching plate displacement of 0.2 m, 0.3 m, and 0.4 m for each bolt pattern. For a mesh displacement threshold of 0.3 m, the red and blue lines in Figure 4.17 connect the points with the lowest mesh resistance force. These lines can be used as the lower bound or conservative engineering design curves.

Following the same process, the lower boundaries of the mesh resistance force were generated for punch device displacements of 0.2 m and 0.4 m, as shown in Figure 4.18. It is recognized that the force that the mesh can apply to loose rock is much smaller than that supplied by the bolts. Nevertheless, there is an opportunity to optimize this force to maximize the benefit from the mesh. For both bolt patterns, the resistance force increases as the mesh area between bolts around loose rock decreases. The mesh resistance force also increases as the displacement of the rock increases.

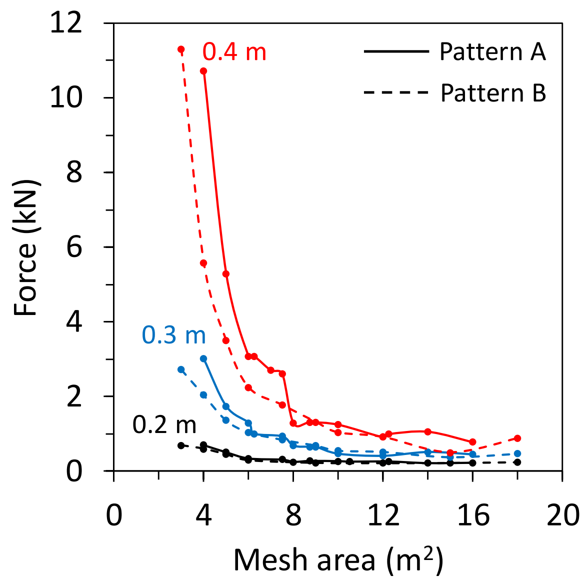

Figure 4.18 Design curves for mesh resistance force mobilized at different mesh displacement for different mesh area and patterns

The mesh resistance force is small (< 3kN) if the area is larger than 7 to 8 m^2, and there is little difference between bolt patterns A and B on the mesh resistance force. It is recommended that the bolt spacing be selected such that the area between four bolts is less than 7 to 8 m^2 (bolt spacing less than approximately 2.7 m) to allow the mesh to mobilize a higher resistance force. Bolt pattern A should create a higher mesh resistance force than bolt pattern B if the area is less than 7 to 8 m^2.

The established curves in Figure 4.18 can help guide engineers to choose a bolt pattern and spacing when designing bolted steel mesh. Starting with an expected size of a loose rock and a desired mesh deformation limit, the mobilized mesh resistance force can be calculated. This force can be used to evaluate whether the mesh can stabilize the rock and achieve equilibrium.

4.6 Summary

This chapter analyzes the influence of bolt patterns and spacing on the force-displacement response and the effectiveness of the high-tensile steel mesh. The modelling results show that punch tests conducted with a rigid supporting frame may underestimate the deformation and overestimate the load capacity of the steel mesh. These testing conditions differ from the boundary conditions of the steel mesh used in the field. In the field, the steel mesh is usually anchored by bolts and plates with various patterns. Boundary conditions that are representative of field conditions and two commonly used bolt patterns were used to model the performance of mesh when loaded by a loose rock located between the rockbolts.

The chapter determines the bolt arrangements that give a more effective mesh response. An effective mesh provides a larger mesh resistance force at lower mesh displacement; thus, a mesh displacement of 0.3 m is chosen as an example to demonstrate the influence of various bolt patterns on the mesh performance. The results are also applicable for other small mesh displacements. For bolt pattern A, a vertical to horizontal bolt spacing ratio that matches the mesh opening aspect ratio (1.72 ratio) makes the mesh more effective at carrying loads and limiting deformations. However, a V/H ratio that matches the mesh opening aspect ratio for bolt pattern B does not help to optimize the mesh effectiveness. Reducing the vertical bolt spacing in pattern B is more important than the horizontal spacing in achieving better mobilization of a mesh resistance force. For both bolt patterns, the mobilized mesh resistance force of steel mesh decreases as the distance from the nearest bolt to the loaded area increases. If the mesh is loaded at the centre within a pattern of bolts and the bolt spacing geometry is close to the mesh opening aspect ratio, the mesh performance for pattern A is better compared to pattern B.

Preliminary engineering design relationships for the mobilized mesh resistance force at different bolt densities and mesh deformations were developed for TECCO G65/3 steel mesh. These relationships can help engineers choose the bolt spacing and provide a lower-bound estimate of the mesh resistance force at the desired deformation limit for a given bolt pattern. An ideal bolt arrangement will help the steel mesh mobilize load quickly at lower deformations. A mesh area less than 7 to 8 m^2 between the nearest bolts around the load is recommended because the mesh will provide a higher resistance force. Also, bolt pattern A has a better performance than bolt pattern B in this range.

Chapter 5: Discrete element method and support vector machine applied to the analysis of rock-bolted steel mesh response

5.1 Overview

It is difficult to achieve the proper pretension in the steel mesh during installation in practice, and the tensile forces mobilized in the wires are typically much less than their tensile strength. Unstable rocks can still move and deform the steel mesh. The current designs of steel mesh pinned by bolts only use the ultimate load capacity of mesh and do not adequately consider the deformation of the mesh. A better design approach must limit the mesh deformations rather than using the ultimate load capacity of the mesh, because large mesh deformations may not be acceptable in practice when there is limited space between rock slopes and buildings or infrastructure.

This chapter presents a study of the performance bolted mesh when resisting a sliding rock block. The chapter is structured in the following sections to cover the following topics. (1) The development of DEM models to simulate wire mesh and a moving rock block are presented. The DEM models simulate field conditions where an unstable rock located between the bolts slides downward along a steep joint to load the bolted steel mesh. (2) A parametric study was performed using 900 DEM simulations to analyze the influences of various factors on the response of the mesh. (3) The DEM simulation results were used to develop a mesh performance prediction model based on a support vector machine learning approach. This predictive tool can be used to evaluate the performance of bolted steel mesh for rock slopes.

5.2 DEM model of bolted steel mesh and rock block

The behaviour of steel mesh depends on many influence factors, such as pinned or fixed boundaries, geometries of rock blocks, contact and relative movement between the rock and steel mesh. This section describes a numerical approach that simulates a steel mesh pinned by bolts interacting with a moving rock block. The loading conditions in the simulations were representative of field conditions.

The steel mesh was modelled by the particle-based mesh model in Chapter 3. The following sections described the modelling of the rock blocks and the construction of the whole model.

5.2.1 Model of rock blocks

The rock block was simulated by a polyhedral element that was proposed and implemented into YADE by Eliáš (2014). Figure 5.1 shows a polyhedral element used as a rock block. According to Eliáš (2014), the creation of a polyhedral element is as follows: (1) a three-dimensional space with a volume of $5 \times 5 \times 5$ units is used; (2) nuclei starting with a nucleus at the centre of the volume are placed at random locations within the volume with an average distance between nuclei of approximately 1 unit; (3) a Voronoi tessellation process is performed on this volume to divide the space by many planar polygons; (4) the polygons surrounding the central nucleus define the shape of a polyhedral element; (5) the final step is randomly rotating the polyhedral element to avoid directional bias. The randomness of the polyhedral element is controlled by a seed factor.

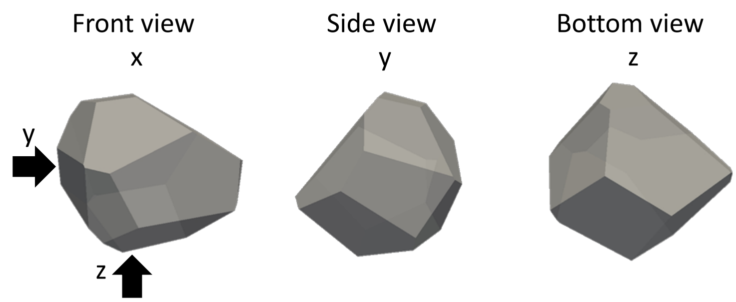

Figure 5.1 Rock block model constructed from a polyhedral element

The randomly generated shape of the polyhedral element captures the irregular shapes of rocks in the field. Hence, various contacts between the rock block and the mesh can be simulated by the model. Because the polyhedral elements are randomly generated, the volume for each polyhedral element is different. The input parameters of a polyhedral element are size factor, aspect ratio, and seed factor. Ten thousand polyhedral elements were generated using size factor = 1 unit, aspect ratio = 1:1:1, and seed factor from 1 to 10,000. Figure 5.2 shows a histogram of the block volume. The mean volume of these polyhedral elements was 0.775 unit^3 with a standard deviation of 0.104 unit^3. For the simulations, the volume of the polyhedral element needs to be restricted to a narrow range of sizes close to the mean value. This was done by finding a relationship between the volume of each polyhedral element and its input parameters. The seed factors that gave a volume between 0.77 to 0.78 unit^3 were selected to generate a seed factor list (398 in total).

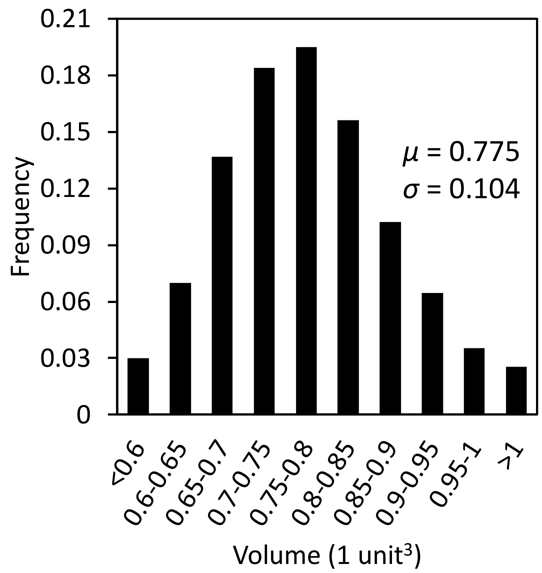

Figure 5.2 Volume histogram for 10,000 randomly generated polyhedral elements using size factor 1 and aspect ratio 1:1:1

Twenty rock blocks were generated using the seed factors that were randomly chosen from this list. The size factor of these blocks ranged from 0.1 to 2, with a 0.1 interval. The relationship between the size factor and volume is shown in Figure 5.3, and it can be expressed by Equation (5.1). Thus, it is possible to generate a rock block with the desired volume by calculating the corresponding size factor.

$$\text{Size factor} = \sqrt[3]{\frac{\text{Volume}}{0.775}} \tag{5.1}$$

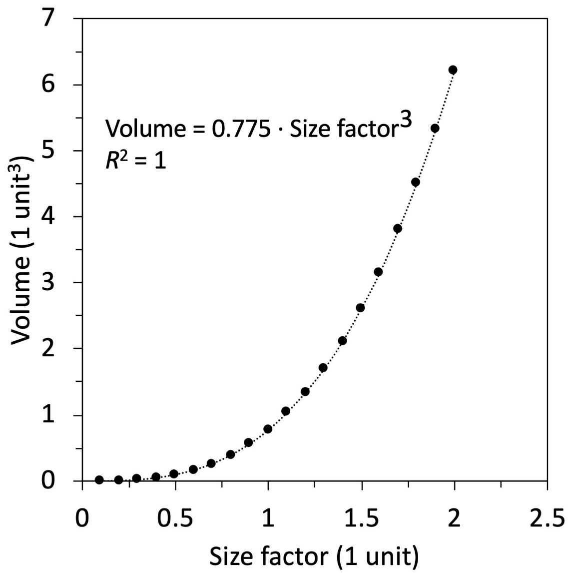

Figure 5.3 Relationship between volume and size factor

5.2.2 Model construction

The modelling considers situations where potentially unstable rocks on a slope have been already scaled down before the installation of bolted steel mesh. The steel mesh is well attached to the slope surface, so there is no gap between the mesh and the rock. Due to weathering or other reasons, a rock block behind steel mesh becomes unstable. It is assumed that the unstable rock will slide along a joint or the intersection of two joints. When the unstable rock pushes against the mesh, the mesh generates a resistance force to stop the movement of the rock. The rock is assumed to stay on the joint(s) during the sliding process. Thus the modelling does not consider a rock that falls down the slope face.

As shown in Figure 5.4a, the DEM model consists of a model of high-tensile steel mesh and a rock block model, as described in Section 3.5 and Section 5.2.1, respectively. The mesh particles at the boundaries are set free in all directions. Thus, the influence of the mesh model size was minor.

The effect of rockbolts and their plates was simplified by fixing the movement in all directions of six mesh particles that were at each bolt location. There were 12 rockbolt plates represented in each model. The mesh model was generated at an inclination angle of β to represent the slope angle (Figure 5.4b). The mesh was assumed to rest on a planar slope surface, but the actual slope surface was not modelled. The simulations were performed by loading the bolted steel mesh by a moving rock block. The simulations were stopped if either of the following criteria were detected: (1) the velocity of the rock in the direction perpendicular to the mesh reverses direction, or (2) one or more mesh wires break. Using the second criterion is somewhat conservative from a mesh design perspective because the mesh can often sustain a few broken wires and still stop the rock's motion via load redistribution. However, this research was interested in assessing the performance of the mesh before it sustained any significant damage.

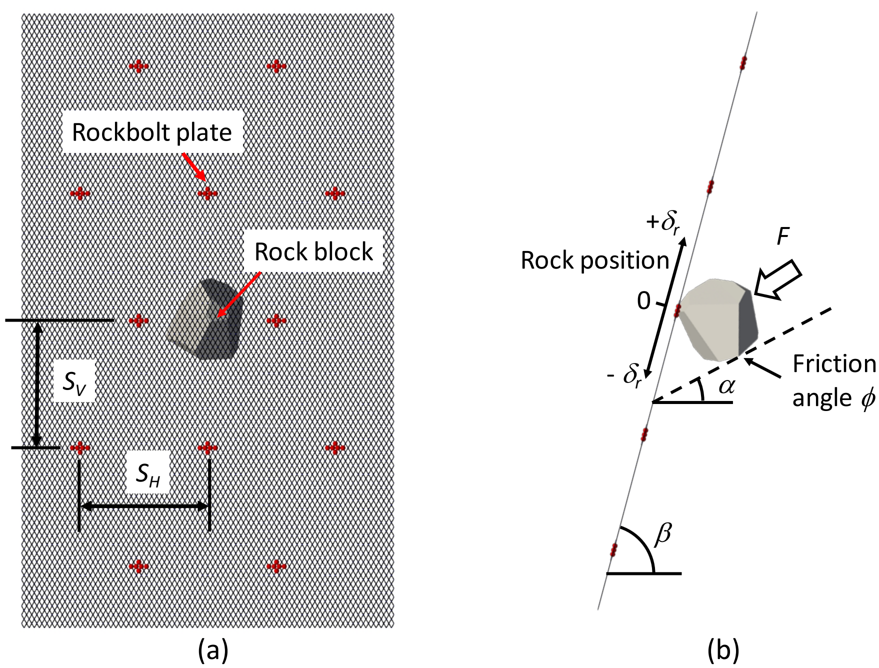

Figure 5.4 DEM model for the rock block and bolted wire mesh (a) front view (b) side view

Note that the boundary condition of the mesh model in this simulation is different from the boundary condition used for mesh model calibration. In the calibration, the mesh boundaries are fixed in all directions. Releasing the mesh boundaries significantly affects the mesh behaviour for both the physical mesh and the mesh model. The physical mesh can bend much more easily along its longitudinal direction because of the chain-link geometry. For example, the mesh can be easily rolled up in the longitudinal direction. The mesh model will also be more flexible because it is made by particles connected by virtual springs. When the mesh model is fixed by simulated 'plates' and subject to load, the force will be transferred through the mesh wires to the plates. Because the mesh model and physical mesh have the same mesh geometry, the load transfer will be similar when they are pinned by plates. However, the mesh model does not capture the bending resistance in the wires in the transverse direction, which results in a larger displacement in the mesh model than in the physical mesh.

The rock was created by a polyhedral element, and it was placed behind the mesh with a specified offset or rock position δ_r relative to the centre of the mesh along the longitudinal direction.

The following assumptions are made to simplify the modelling:

(1) No gravity is applied in the simulation.

(2) A constant force F is applied to the rock at an orientation of α (sliding angle) to simulate the mesh loading by the rock.

The mesh is only affected by the movement of the rock because no gravity is simulated in the model. The steel mesh initially has no tensile forces in the springs that represent the wires. As the rock moves into the mesh, the wires (springs) mobilizes resisting tensile forces. The sliding angle can be taken to represent the joint dip angle for planar sliding or the inclination angle of two joints intersecting to form a sliding wedge. The analysis considers the sliding angle as the dip angle of a plane upon which the block slides to be conservative. The movement direction of the rock may shift slightly in response to the force applied to the rock by the mesh. This effect can be more pronounced in the vertical direction depending on the relative position of the rock with respect to the pattern of fixed particles representing the plates.

The magnitude of the load applied to the rock block, F, was based on a calculation of the unbalanced force for a block sliding along a virtual joint with a friction angle of ϕ (no cohesion) that is inclined at an angle α. The rock volume V_{rock} and the assumed density of the rock (ρ = 2,600 kg/m^3) also affect F. Equation (5.2) is applicable for a simple planar sliding mechanism for the rock block.

$$F = \rho g V_{\text{rock}} \sin\alpha - \rho g V_{\text{rock}} \cos\alpha \tan\phi \qquad (5.2)$$

The force F was kept constant in the model, whereas for real rock, as the mesh was deformed, it would apply a force that would increase the sliding resistance, thus decreasing F. This assumption makes the simulated deformation of the steel mesh larger than that in the field.

It is worth noting that there was no contact detection between the virtual mesh wires and the rock. The interaction only existed between the rock model and the particles in the mesh model. This may cause the mesh displacement to be larger compared to actual mesh because the mesh does not recognize the rock until the mesh particles contact the rock. However, the influence is minor because the rock size was much larger than the opening size in the mesh.

The interaction between the rock block model and mesh model follows the classical contact law between discrete elements (Cundall and Strack 1979). The contact properties for the rock-mesh interaction in this paper were set as $k_n = 1 \times 10^7$ N/m, $k_s/k_n = 0.15$ and $\varphi = 30°$. YADE uses a numerical damping scheme that decreases the force causing the particle velocity (Šmilauer et al. 2015). In the simulations, the damping for the rock was set to zero for the block sliding. Local non-viscous damping of 0.5 was applied to the mesh to simulate the mesh resistance due to the wire bending. An increase of the damping coefficient will decrease the mesh displacement. A similar damping parameter for a mesh model was also used by Thoeni et al. (2013).

Table 5.1 shows the ranges of the input parameters. The rock volume ranged from 0.1 to 3 m^3, which covers small to large rock blocks held by bolted steel mesh. Rock slopes are often excavated at a slope of 0.25:1 (H:V), which corresponds to a slope angle of ~75°. The simulations considered a range from 65° to 85°, which matches the historical cases in Table 5.2. The other parameters were assumed based on engineering experience.

Table 5.1 Input parameters for DEM simulations

Input parameters	Range
Volume of rock V	0.1 - 3 m^3
Slope angle β	65 - 85°
Sliding angle α	30 - 50°
Friction angle ϕ	25 - 40°
Rock position δ_r	-0.5 to 0.5 m

The choice of the bolt pattern and spacing used in the model was based on observations of common practice. Two different patterns are usually used for bolted steel mesh, namely, pattern A and pattern B (Xu et al. 2019). In pattern A, the bolts are aligned in rows and columns. In pattern B, the bolts in alternating rows are offset one half of the separation distance between the bolts. The arrangements of bolts used for 11 rock slope stabilization projects are listed in Table 5.2 (retrieved from https://www.geobrugg.com/en/Slope-Protection-77493.html). As shown in Table 5.2, bolt pattern B was used more often than pattern A for the TECCO mesh. For the simulations, only pattern B was used.

Table 5.2 Bolt patterns and spacing for rock slopes in the past projects

Location	Year	Slope angle	Mesh type	Bolt pattern	Bolt spacing (m)
National road D8, Croatia	2013	60-85°	TECCO G65/3	A	2.5 × 2.5 *
Sapjane, Croatia	2015	65-90°	TECCO G65/3	A	2 × 2.5 *
Demir Kapija-Smokvica motorway, Macedonia	2013	65-85°	TECCO G65/3	B	4 × 1.25 *
Wetter, Germany	2014	60-85°	TECCO G65/3	B	2.5 × 3 *
Bilaspur, Himachal Pradesh, India	2015	60-80°	TECCO G65/3	B	1.9 × 1.9 2.4 × 2.4
Zion Hill, Panama	2015	65-80°	TECCO G65/3	B	2.5 × 2.5
San Jose - Calderas, Costa Rica	2015	45-85°	TECCO G65/3	B	2 × 2
Marinella di San Terenzo, Comune di Lerici, Italy	2017	60-80°	TECCO G45/2	B	3 × 3
Udhampur, Jammu & Kashmir, India	2017	65-70°	TECCO G65/3	B	2 × 2 2.5 × 2.5
Meja, Croatia	2017	75-80°	TECCO G65/4	B	2 × 2 *
Lauca, Angola	2017	40-90°	TECCO G65/3	B	1.4 × 1.4 3 × 1.4 5 × 5 2 × 2

* Visually estimated from photos in the published case history

The bolt spacing typically ranges from 2 to 3 m. Hence, models were constructed with a 2 × 2 m bolt spacing, a 2.5 × 2.5 m bolt spacing, and a 3 × 3 m bolt spacing. For the 2 × 2 m bolt pattern, the size of the mesh model was 6 × 10 m (10,363 particles). For the 2.5 × 2.5 m bolt pattern, the mesh model was 6 × 12 m (12,420 particles). For the 3 × 3 m bolt pattern, the mesh model was 8 × 14 m (19,207 particles).

This study conducted 300 simulations for each bolt spacing using a combination of input parameters (900 simulations in total). A Latin-Hypercube sampling (Fang et al. 2006) method was used for the simulations, assuming a uniform distribution of values for the input parameters.

5.3 Simulation results

5.3.1 Response of steel mesh deformed by a rock block

Two mesh responses occurred in the simulations: (1) the bolted steel mesh successfully resisted the moving rock block or (2) one or more wires ruptured in the mesh. The mesh was considered capturing the rock when the movement of the rock in the direction perpendicular to the mesh reversed direction. The maximum bulge of the steel mesh was also recorded in the simulations. Where mesh bulge data are presented, they only include data from cases in which no wires ruptured.

Figure 5.5 shows two mesh response examples for a 2 × 2 m bolt spacing with two different rock sizes. The ratio of tensile force in the wires to the maximum allowable tensile force (12.5 kN) is also shown. For both cases, the rock started its motion centred with the bolt pattern (rock position $\delta_r = 0$). The position of the rocks shown in Figure 5.5 captures how the rock has moved downward with respect to the bolt pattern. The smaller rock was stopped or captured by the mesh, whereas the larger rock resulted in the rupture of mesh wires near the plate immediately below the rock.

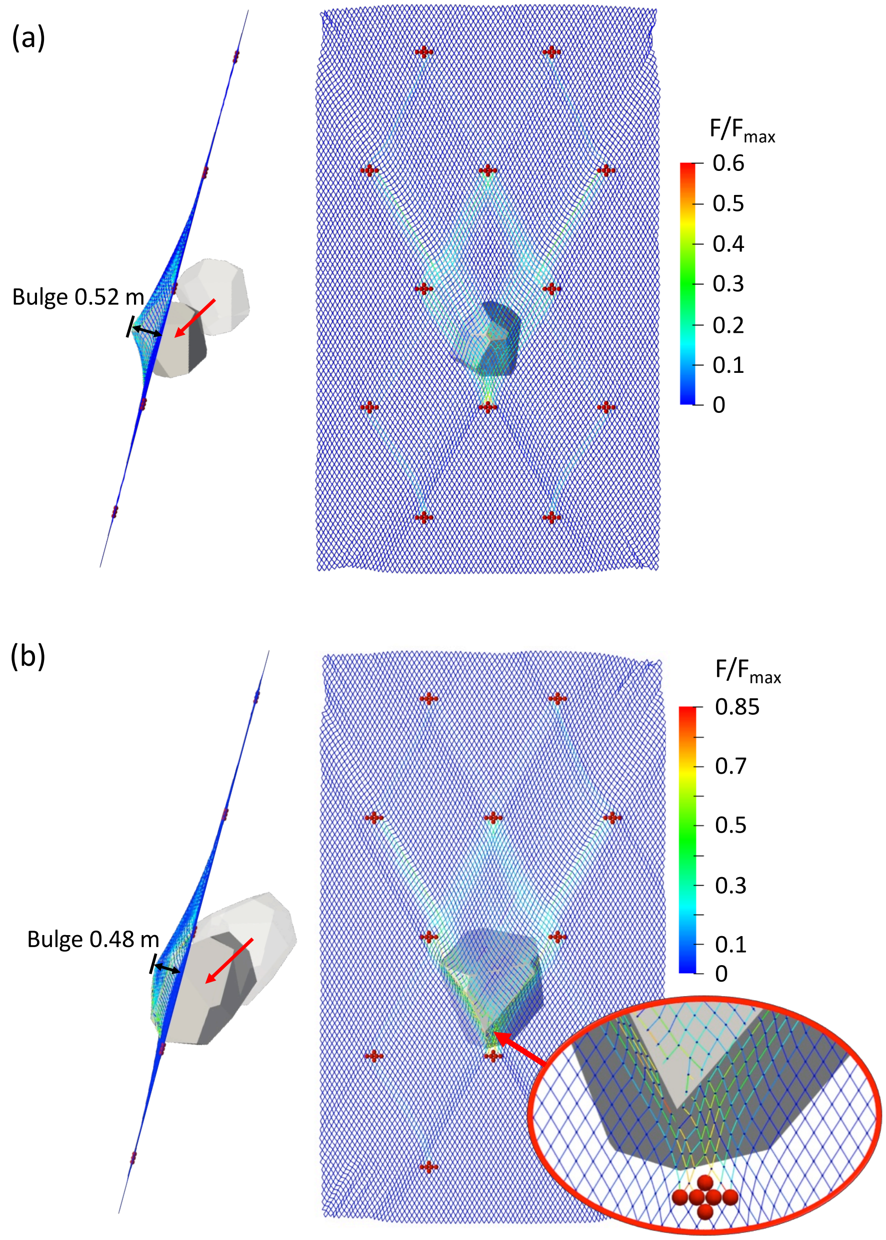

Figure 5.5 Mesh responses for bolt pattern B with a 2 × 2 m spacing (β = 75°, α = 40°, ϕ = 30°, δ_r = 0 m)
(a) rock captured by bolted mesh: V = 0.78 m^3 and (b) wire failure: V = 2.62 m^3

The bolted steel mesh successfully captured the 0.78 m^3 rock without damaging the steel mesh (Figure 5.5a). The maximum bulge of the steel mesh is 0.52 m. The load was transformed from the rock to the rockbolt plates in the second and third row, as well as the rockbolt plate below the rock (the middle one in the fourth row). The tensile force was mainly concentrated in the wires near the rockbolt plate below the rock block. The most critical wire reached 60% of its tensile strength.

Several mesh wires broke in resisting the movement of the 2.62 m^3 rock (Figure 5.5b). The load transformation is similar to the first case. The maximum bulge of the steel mesh was 0.48 m, which is slightly smaller than the other case. The reason is that a larger contact area between the large rock and mesh results in a larger local deformation in mesh wires to resist the rock movement, which ruptured mesh wires.

5.3.2 Influence of rock volume and sliding angle

Figure 5.6 shows the sliding angle α versus the rock volume V for all 2 × 2 m bolt spacing simulations. The symbols on this plot show ranges of the maximum mesh bulge or whether the model was stopped because of the rupture of mesh wires. The bolted wire mesh captured the rock block successfully in 180 cases. The rock did not even move in 45 cases because the friction angle was larger than the inclination angle; these results are not plotted. The maximum mesh bulge was 0.2 to 0.4 m in 63 cases, 0.4 to 0.6 m in 111 cases, and 0.6 to 0.7 m in 5 cases. The cases in which wires ruptured are clustered at the upper right half of the plot, where simulations with larger rocks and steeper virtual joints occur.

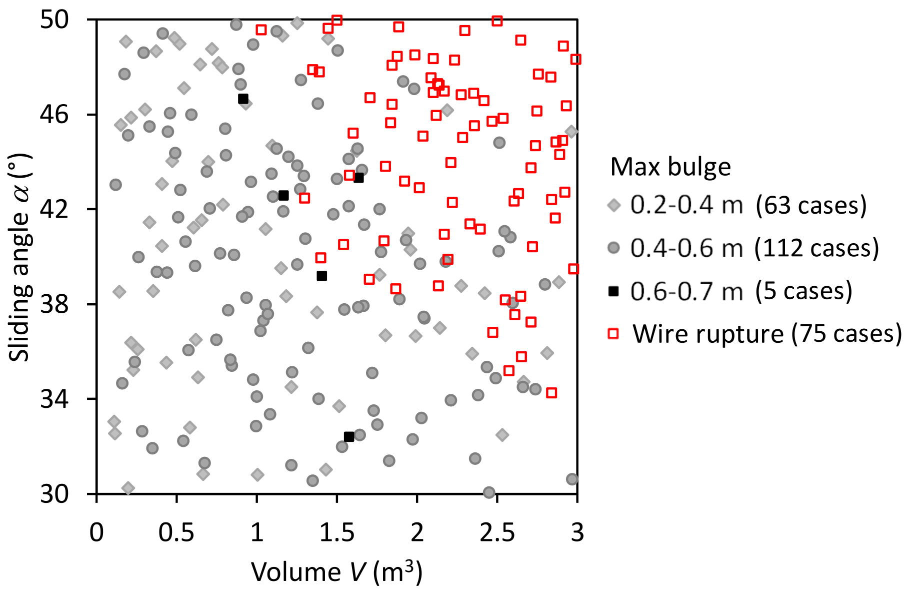

Figure 5.6 Simulation results of α versus V for 2 × 2 m bolt spacing

Table 5.3 shows the percent of cases with wire rupture for different rock volumes. The bolted steel mesh worked well if V was less than 1 m^3 (no wire ruptures). The percent of cases with wire rupture increases as V increases. When the rock was 2 to 3 m^3, 49% to 54% of the cases experienced a wire rupture.

Table 5.3 Influence of rock volume on mesh response for 2 × 2 m bolt spacing

V (m^3)	Total number	Wire rupture	Percent of cases with wire rupture
0-1	93	0	0
1-1.5	51	6	12%
1.5-2	53	16	30%
2-2.5	51	25	49%
2.5-3	52	28	54%

Table 5.4 shows the influence of the sliding angle α on the percent of cases with wire rupture. For α between 30° and 35°, only one out of 75 cases had a wire rupture. The percent of cases with wire rupture increases as α increases. For example, 49% of the cases had wires rupture if α was between 45° to 50°.

Table 5.4 Influence of sliding angle for 2 × 2 m bolt spacing

α (°)	Total number	Wire rupture	Percent of cases with wire rupture
30-35	75	1	1%
35-40	75	13	17%
40-45	75	24	32%
45-50	75	37	49%

Figure 5.7 shows the influence of rock volume V on the mesh bulge. The number of cases in which the mesh bulge was between 0.2 and 0.4 m decreases as V increases. The number of cases in which the mesh bulge was between 0.4 and 0.6 m increases slightly as the range in V increases from 0 - 1 to 1 - 2 m^3. The number of cases in which V is greater than 2 m^3 is small because a large portion of the simulations caused a rupture of a wire.

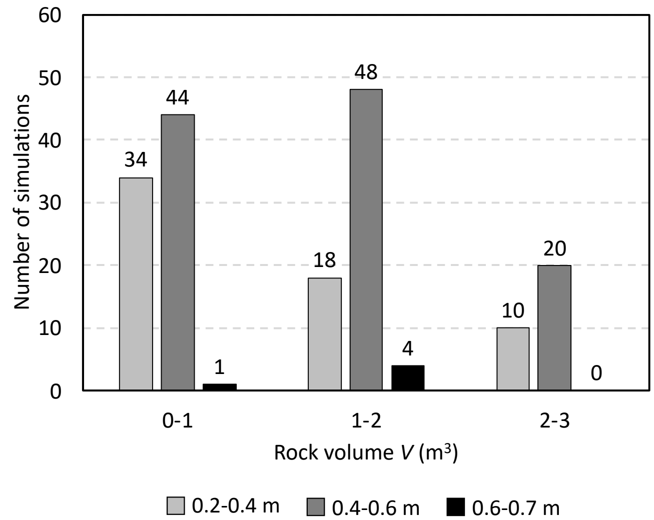

Figure 5.7 Influence of V on the mesh bulge for 2 × 2 m bolt spacing

Figure 5.8 shows the influence of the virtual sliding angle α on the mesh bulge. The number of cases in which the mesh bulge was between 0.2 and 0.4 m fluctuates as α increases, whereas the number of cases in which the mesh bulge was between 0.4 and 0.6 m shows an increasing trend as α increases. The number of cases in which $\alpha > 45°$ is small because many simulations with a steep sliding angle caused a rupture of a wire.

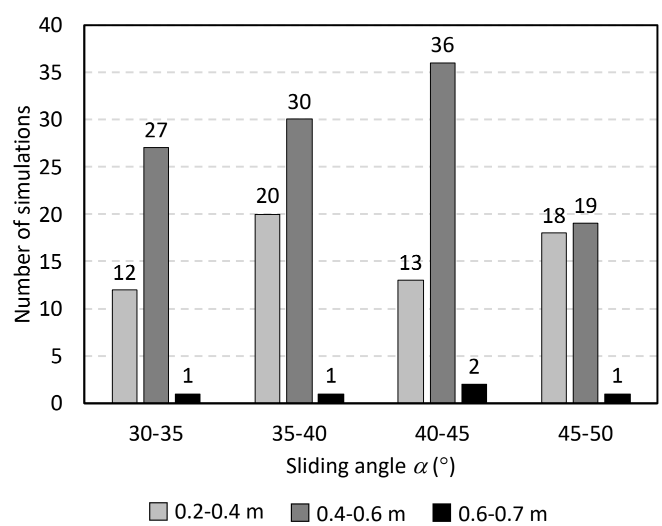

Figure 5.8 Influence of α on the mesh bulge for 2 × 2 m bolt spacing

The rock volume and sliding angle obviously have a large influence on the mesh response because they determine the force acting on the mesh and the loading direction with respect to the mesh panel. A large rock sliding on a steep joint is more likely to result in a large mesh bulge and to damage the steel mesh.

5.3.3 Influence of slope angle and rock position

Figure 5.9 shows the slope angle β versus the rock volume V for all 2×2 m bolt spacing simulations. The wire rupture cases are evenly distributed along the axis of the slope angle, which indicates that β has a minor influence on the mesh wire rupture. The results for the influence of β on the mesh bulge are shown in Figure 5.10. As β increases, the number of simulations in which the mesh bulge was between 0.2 m and 0.4 m decreases, whereas the number of simulations where the mesh bulge was greater than 0.4 m increases. Thus, a large mesh deformation may be expected on steeper rock slopes. The reason is that a steeper slope surface increases the angle between the loading direction and mesh panel. The mesh is more deformable if the load is perpendicular to the mesh.

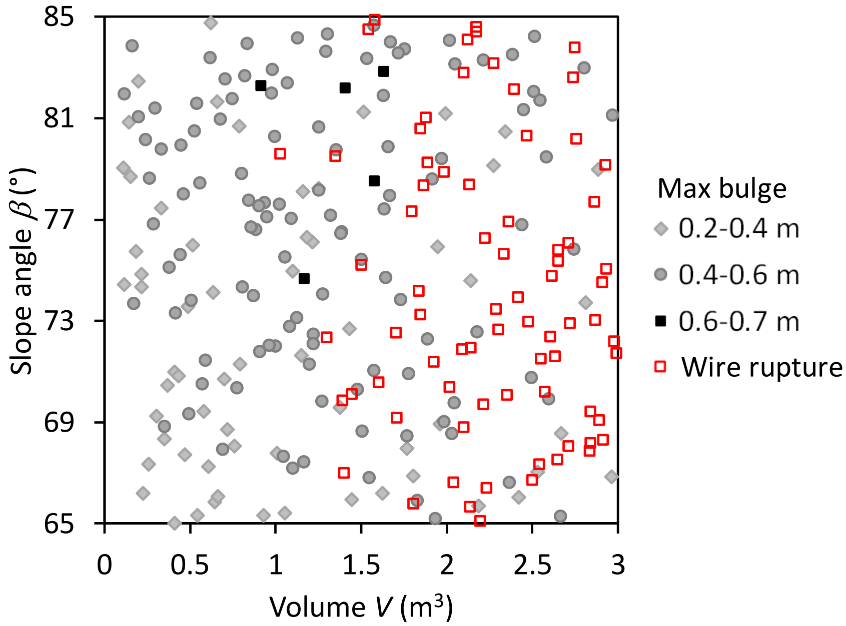

Figure 5.9 Simulation results for β versus V for 2 × 2 m bolt spacing

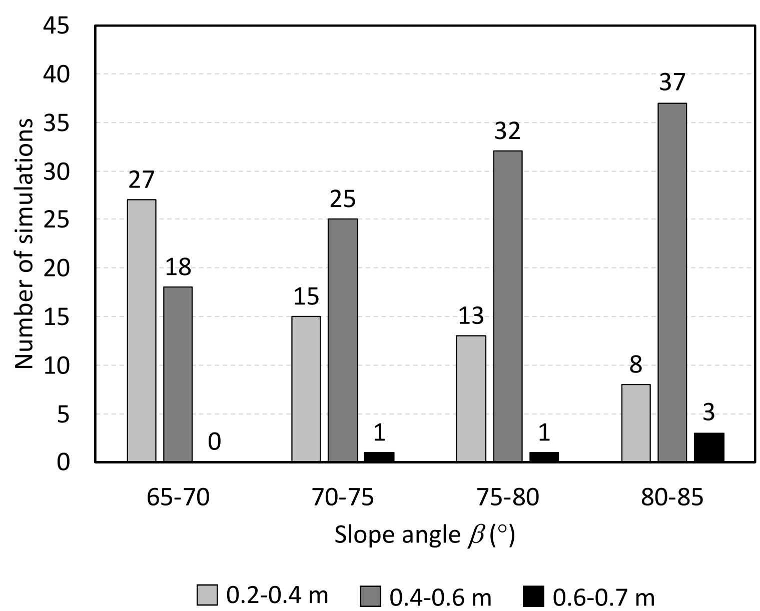

Figure 5.10 Influence of β on the mesh bulge for 2 × 2 m bolt spacing

Figure 5.11 shows the rock position δ_r versus the rock volume V for all 2 × 2 m bolt spacing simulations. The cases in which the wire ruptured are evenly distributed along the axis of rock position. This distribution indicates that δ_r has little influence on the rupture of wires in the mesh. The results for the influence of δ_r on the mesh bulge are shown in Figure 5.12. The mesh bulge increases if the rock is closer to the upper bolt, whereas the mesh bulge decreases if the rock is closer to the bottom bolt. A large mesh bulge (0.6 to 0.7 m) only occurs when the rock position was above the centre between the bolts ($\delta_r > 0$ m). The most flexible part of a mesh is at the centre within a pattern of bolts. When an unstable rock originates closer to the upper bolt, it may slide down towards the centre of the bolt pattern, thus causing a large mesh displacement.

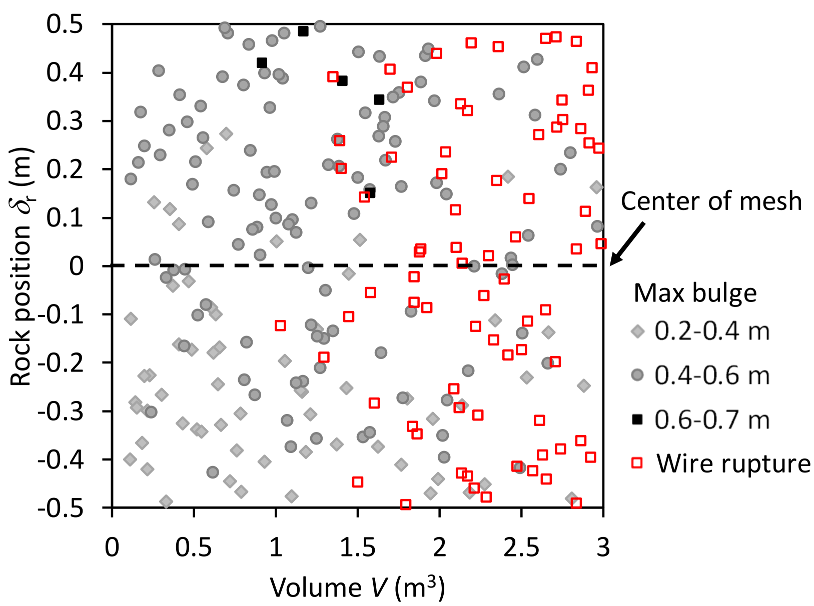

Figure 5.11 Simulation results for δ_r versus V for 2 × 2 m bolt spacing

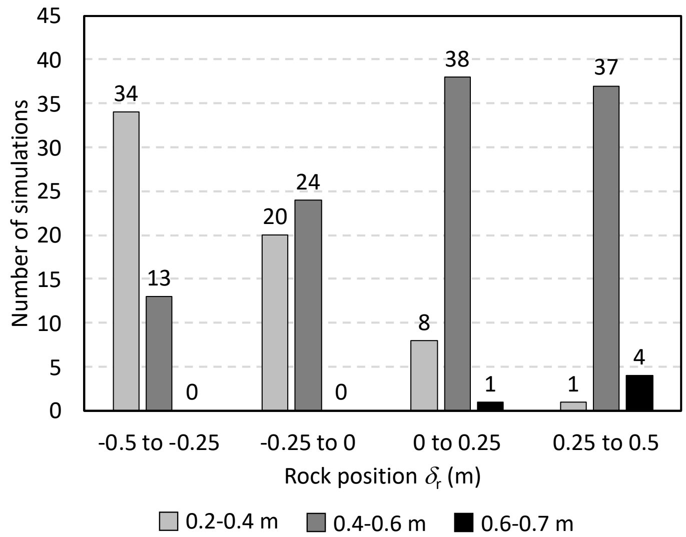

Figure 5.12 Influence of δ_r on the mesh bulge for 2 × 2 m bolt spacing

5.3.4 Influence of force applied by the rock on steel mesh

Figure 5.13 shows the simulation results for different forces (F) applied by the rock to the mesh for all 2 × 2 m bolt spacing simulations. Recall that F is the unbalanced force calculated for a sliding block using Equation (5.2), and its magnitude is typically much smaller than the weight of the rock. Two boundaries (dash lines) can be seen in Figure 5.13. The steel mesh stops the rocks if $F < 8.5$ kN. A force larger than 13 kN ruptures mesh wires. The steel mesh may stop the rock, or the wires may rupture if the force is between 8.5 and 13 kN. A large force occurs for large blocks sliding on steep joint surfaces. The mesh sustained broken wires at forces that are seven times lower than what was reported as the mesh capacity measured in laboratory tests where the mesh was fixed to a loading frame, and many wires work together to carry the load (Geobrugg 2014).

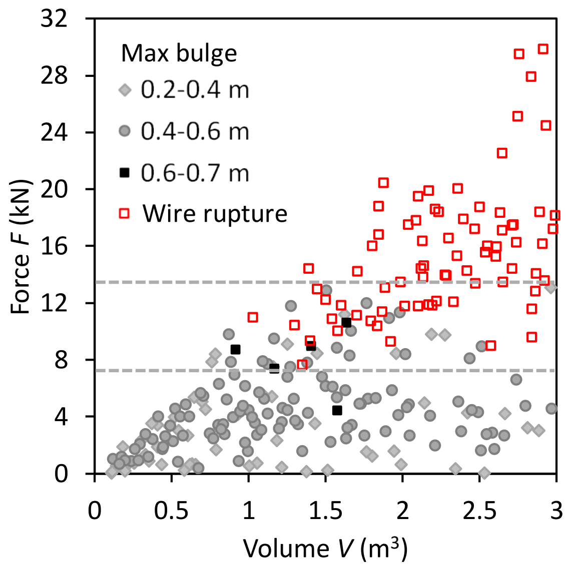

Figure 5.13 Simulation results of F versus V for 2 × 2 m bolt spacing

5.3.5 Influence of bolt spacing

Figure 5.14 and Figure 5.15 show the sliding angle versus the rock volume and the force versus the rock volume for all 2.5 × 2.5 m and 3 × 3 m bolt spacing simulations, respectively. The results show similar distributions to the 2 × 2 m bolt spacing simulations. The number of cases with wire rupture is 86 out of 300 for a 2.5 × 2.5 m bolt spacing, and 90 out of 300 for a 3 × 3 m bolt spacing. The wire rupture cases are also clustered at the upper right half of the α versus V plots. The increase of the bolt spacing only slightly increases the percentage of cases with mesh wire rupture. The rocks were captured by steel mesh if $F < 8$ kN and a force larger than 12 kN typically caused wire rupture.

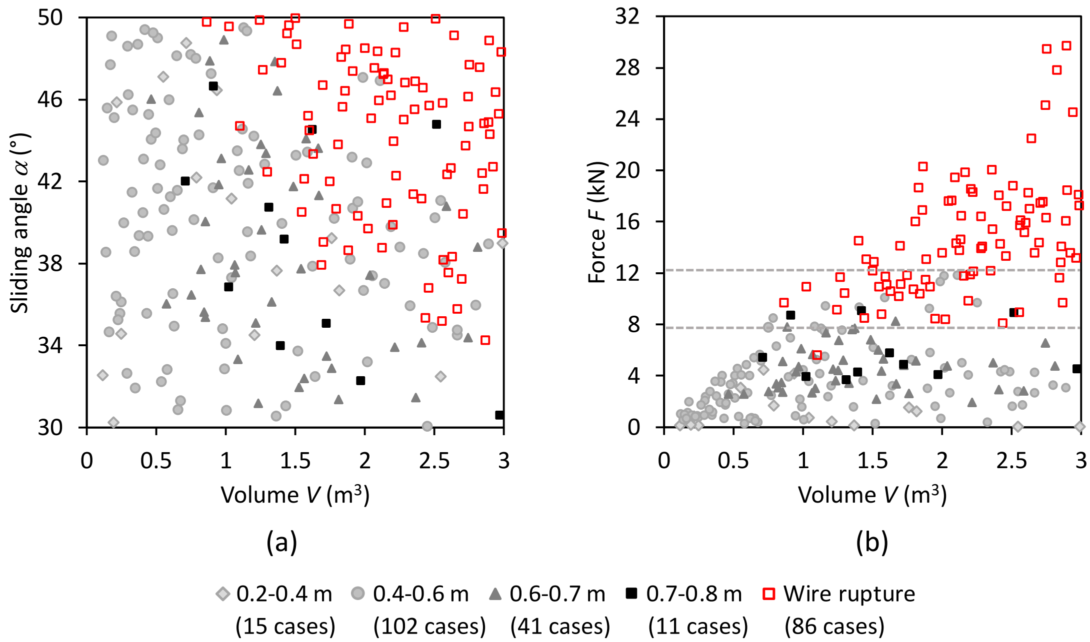

Figure 5.14 Simulation results for (a) α versus V and (b) F versus V for 2.5 × 2.5 m bolt spacing (dash lines show boundaries between different types of mesh response)

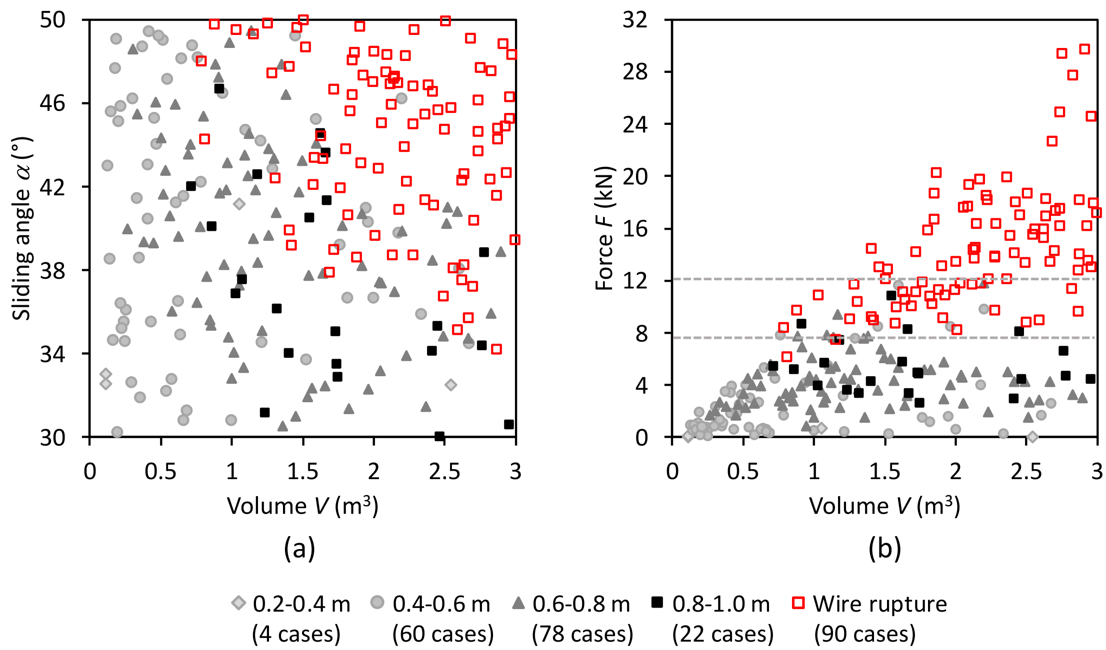

Figure 5.15 Simulation results for (a) α versus V and (b) F versus V for 3 × 3 m bolt spacing (dash lines show boundaries between different types of mesh response)

The bolt spacing has a large influence on the steel mesh deformation. Figure 5.16 shows the number of cases of various mesh bulge for different bolt spacings. As expected, the overall mesh bulge increases as the bolt spacing increases. For both 2 × 2 m and 2.5 × 2.5 m bolt spacing, most mesh bulges were 0.4 to 0.6 m (112 and 102 cases). For a 3 × 3 m bolt spacing, most mesh bulges were 0.6 to 0.8 m (78 cases). A 2 × 2 m bolt spacing successfully restrained most rocks with a mesh bulge less than 0.6 m, whereas a 3 × 3 m bolt spacing had 22 cases with a mesh bulge greater than 0.8 m. Larger spacing between bolts results in a more flexible mesh response.

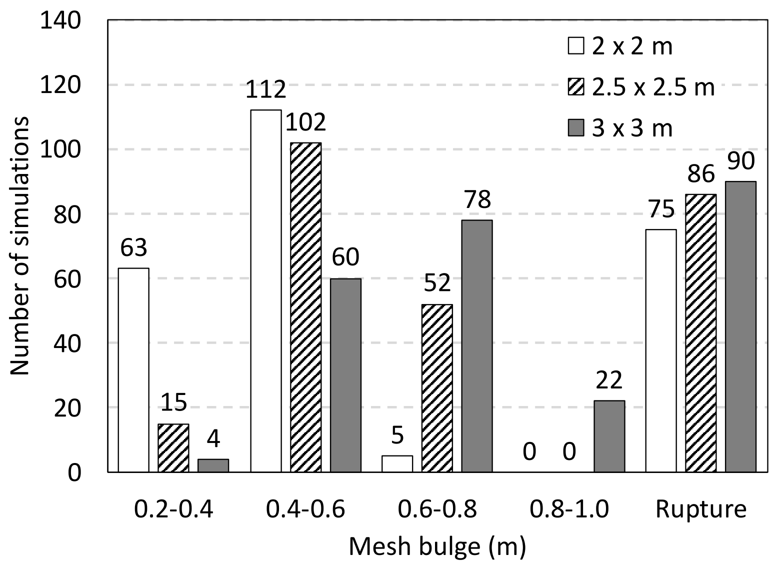

Figure 5.16 Comparison between 2 × 2 m, 2.5 × 2.5 m and 3 × 3 m bolt spacing

5.4 Support Vector Machine approach

The support vector machine (SVM) approach, one of the widely used machine learning algorithms, was used to analyze the response of bolted steel mesh to the loading by a rock block. The SVM modelling was conducted with the scikit-learn library (Pedregosa et al. 2011), an open-source machine learning code in Python. The numerical simulation results in Section 5.3 were used to train and test the performance of SVM models. The complex relationship between the mesh responses and a wide range of influence factors can be captured. The advantage of using SVM is that it has a regulation parameter to avoid overfitting. SVM can find out the global optimum which overcomes the limitations of other machine learning algorithms like ANN.

5.4.1 A brief introduction to SVM

Although the SVM was developed to distinguish two-class problems, it can also be used in multiclass classification by introducing the one-versus-rest or one-versus-one method. The one-versus-one method in scikit-learn was used. The basic idea is to construct one classifier for each pair of classes. When predicting, each classifier votes for one class, and the class that receives the most votes is selected. The advantage of this method is that any unbalance in the class sizes is taken into account.

A basic two-class SVM classifies the data points by finding the best hyperplane that separates all data points of one class from the other (Figure 5.17). The points that are closest to this hyperplane are called the support vectors. The optimal hyperplane is the one with the largest margin between the two classes. The margin is the maximum distance between support vectors on each side of the hyperplane. Kernel functions can be used to transform the data points from one space to another space with higher dimensions to better separate the data points. The three frequently used kernel functions (Liu et al. 2019) are as follows:

(1) Linear kernel function (LF)

$$K(x, y) = x \cdot y \tag{5.3}$$

(2) Polynomial kernel function (PF)

$$K(x, y) = (1 + x \cdot y)^d, d = 1, 2, 3 \dots \tag{5.4}$$

(3) Radial basis function (RBF)

$$K(x, y) = \exp(-\gamma \cdot \|x - y\|^2) \tag{5.5}$$

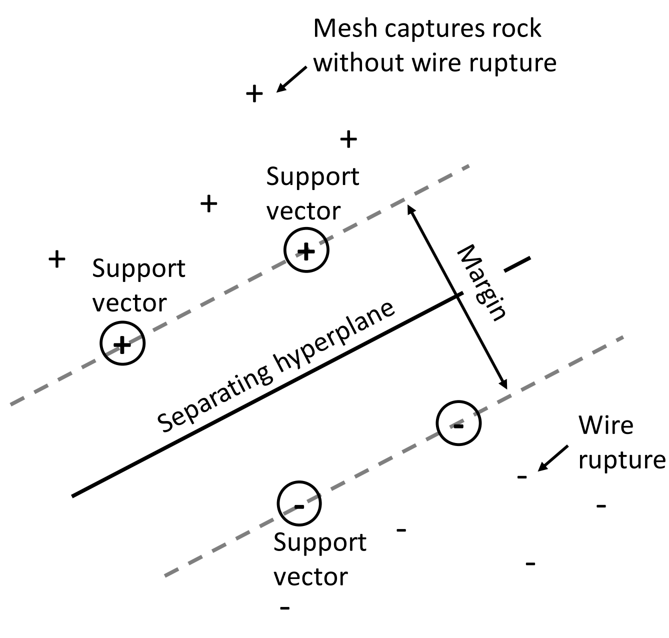

Figure 5.17 Support vectors and hyperplane in SVM

An SVM can be categorized into hard- and soft-margin SVM (Brereton and Lloyd 2010). A hard-margin SVM finds the optimal boundary that exactly separates the classes. This may lead to overfitting when forcing the algorithm to search for this optimal hyperplane. To avoid overfitting in the model, the soft-margin SVM is used to tolerate a degree of misclassification and balance the classification error by introducing a penalty parameter C. A larger value for C means a lower tolerance of misclassification and more complex boundaries. Thus, the SVM is trained to determine the parameters in the chosen kernel function and the penalty parameter C that provide the lowest misclassification error. These parameters are called hyperparameters in machine learning.

5.4.2 SVM modelling process

The first step in the machine learning modelling was data preprocessing. The data from numerical simulations were grouped into two categories, a feature group and a target group. The feature group (input group) contains the bolt spacing, rock volume V, sliding angle α, slope angle β, friction angle ϕ, and rock position δ_r. The feature group data were standardized by their mean and standard deviation. The target group (output group) is the mesh response. A mesh bulge of 0.5 m was added as a criterion in the mesh response. Thus, three mesh responses were the output: (a) mesh bulge less than 0.5 m without breaking a wire, (b) mesh bulge greater than 0.5 m without breaking a wire, and (c) one or more wires in the mesh ruptures. Then, the whole data set was randomly split into two sets, one set for training (training data set) and one set for testing (testing data set). The ratio between the two sets was 80% to 20% (720 versus 180).

The next step was to use the training set data to train a model. The goal is to search for the hyperparameters that give the best modelling performance. The 10-fold cross-validation strategy was applied to access the performance of a trained model. In the cross-validation process, the training set data were randomly divided into 10 subsets. The model training was repeated 10 times. Each time, one of the 10 subsets was used to test the modelling performance after the other 9 subsets were put together to train the model. The modelling performance was examined by the accuracy, which is defined by Equation (5.6),

$$\text{Error} = \frac{1}{n}\sum_{i=1}^{n} I\{\hat{y}_i \neq y_i\} \tag{5.6}$$

where n is the sample size, $\hat{y}_i$ is the predicted mesh response, and y_i is the corresponding mesh response from the numerical results. $I\{x\}$ is the indicator function, 1 if $\hat{y}_i = y_i$, else 0 if $\hat{y}_i \neq y_i$. The average accuracy across all 10 sets of training was computed.

A random search technique (Bergstra and Bengio 2012) was applied to find the best combinations of the hyperparameters that give the highest modelling accuracy. As such, an optimal model was obtained after retraining the model using the whole training data set with the best hyperparameters.

The last step was to evaluate the prediction performance of the obtained model using the test data set. One way is to use accuracy in Equation (5.6), and another way is to use the confusion matrix (Awad and Khanna 2015). The confusion matrix technique shows the misclassification rate of a model in the predicted mesh responses. The scenario of two types of mesh response is taken as an example to explain this technique. The response of bolted steel mesh is classified as Class S if rock block stops without rupturing a wire, and Class R if one or more wires in the mesh ruptures. With reference to the DEM simulation results, a prediction model can provide good predictions (true, T) and bad predictions (false, F). As shown in Table 5.5, a good prediction can be positive (TP) if Class S is estimated by the model and Class S is observed in the DEM results; a good prediction also can be negative (TN) if Class R is estimated by the model and Class R is observed in the DEM results. Similarly, a bad prediction can be positive (FP) if Class S is estimated by SVM, but Class R is observed in the DEM results; a bad prediction can also be negative (FN) if Class R is estimated by the model, but Class S is observed in the DEM results.

Table 5.5 Confusion matrix

DEM results	Model Prediction	
	Class S	Class R
Class S	TP	FN
Class R	FP	TN

Based on the confusion matrix, two criteria, namely Precision and Recall, can be used to evaluate whether a model makes good predictions of each class. For a prediction of Class S, the Precision is calculated by Equation (5.7), which shows the proportion of the predicted Class S that is actually correct. The Recall is calculated by Equation (5.8), which shows the proportion of the actual Class S that is correctly identified. An ideal model should have both Precision and Recall that are close to 1. It is often convenient to combine Precision and Recall into one metric, namely F_1 score, to evaluate a model's performance. The F_1 score is the weighted average of Precision and Recall and is calculated by Equation (5.9). A model with a higher F_1 score is better.

$$Precision = \frac{TP}{TP + FP} \tag{5.7}$$

$$Recall = \frac{TP}{TP + FN} \tag{5.8}$$

$$F_1 = 2 \cdot \frac{Precision \cdot Recall}{Precision + Recall} \tag{5.9}$$

5.4.3 SVM modelling results

Table 5.6 shows the optimized hyperparameters for each algorithm. These parameters gave the highest prediction accuracy for their models. Figure 5.18 shows the cross-validation accuracy curves of each machine learning algorithm with different numbers of DEM simulations used in training (training data size) when using the optimized hyperparameters. The cross-validation accuracy represents the prediction capability of each algorithm. As expected, the cross-validation accuracy increases as the training size increases. The rate of improvement in the prediction accuracy slows down dramatically once the training data size increases beyond approximately 100 to 150. The maximum cross-validation accuracy is around 85%-87% for the SVM-PF and SVM-RBF models, and about 80% for the SVM-LF model. Thus, the SVM-PF and SVM-RBF models should have a better prediction performance than the SVM-LF model.

Table 5.6 Optimized hyperparameters for each algorithm

Algorithms	Hyperparameters	
SVM-LF	$C = 1.437$	
SVM-PF	$C = 0.2313$	$d = 2$
SVM-RBF	$C = 7.7561$	$\gamma = 0.0342$

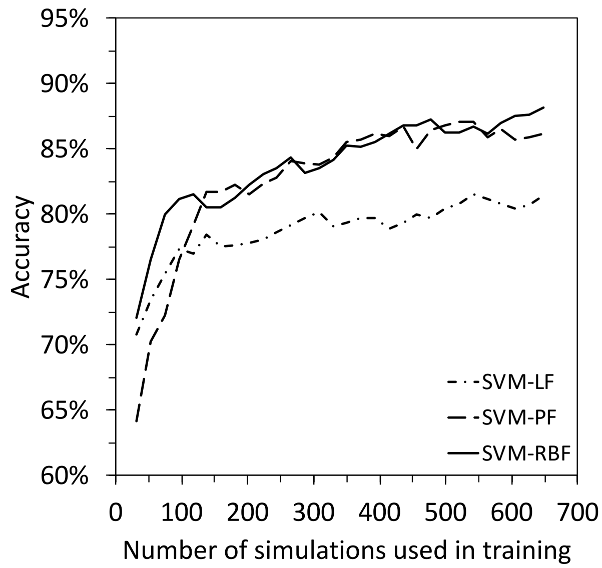

Figure 5.18 Cross-validation accuracy curves for different algorithms

Next, the models were trained with the whole set of training data (720 cases), and the trained models were used to make predictions with the test data (180 cases). Figure 5.19 shows the confusion matrix for the models with different algorithms. The correct prediction numbers are in the light grey boxes, and the misclassified prediction numbers are in the dark grey boxes. The confusion matrixes were used to calculate the precision, recall, and F_1 score for each prediction class, as shown in Table 5.7. The weighted average F_1 scores of SVM-PF and SVM-RBF models were both 0.92, which means that these two models had good overall prediction performance. The

SVM-LF model has a weighted average F_1 score of less than 0.9, which indicates that it provided poorer predictions.

Table 5.7 Performance evaluation of different algorithms

Classifier	Predictions	Precision	Recall	F_1 score
SVM-LF	Bulge < 0.5 m	0.85	0.84	0.84
	Bulge > 0.5 m	0.83	0.78	0.80
	Wire rupture	0.90	0.96	0.93
	Weighted average	0.86	0.86	0.86
SVM-PF	Bulge < 0.5 m	0.91	0.91	0.91
	Bulge > 0.5 m	0.92	0.87	0.90
	Wire rupture	0.92	0.96	0.94
	Weighted average	0.92	0.92	0.92
SVM-RBF	Bulge < 0.5 m	0.94	0.90	0.92
	Bulge > 0.5 m	0.91	0.87	0.89
	Wire rupture	0.90	0.98	0.94
	Weighted average	0.92	0.92	0.92

DEM results

SVM-LF predictions

	Bulge<0.5	Bulge>0.5	Wire rupture
Bulge<0.5	57	7	4
Bulge>0.5	10	43	2
Wire rupture	0	2	55

SVM-PF predictions

	Bulge<0.5	Bulge>0.5	Wire rupture
Bulge<0.5	62	4	2
Bulge>0.5	4	48	3
Wire rupture	2	0	55

SVM-RBF predictions

	Bulge<0.5	Bulge>0.5	Wire rupture
Bulge<0.5	61	4	3
Bulge>0.5	4	48	3
Wire rupture	0	1	56

Figure 5.19 Confusion matrix of the prediction results on the test data set for different algorithms

It is important to examine the precision of the mesh bulge < 0.5 m class, the recall of mesh bulge > 0.5 m class, and recall of mesh wire rupture class because low precision and recall values indicate a higher risk for overestimating the performance of the bolted steel mesh. The SVM-PF and SVM-RBF models had a similar precision score in mesh bulge < 0.5 m class (0.94 versus 0.91), a similar recall score in wire rupture class (0.98 versus 0.96), and the same recall score in mesh bulge > 0.5 m class (0.87). Thus, both models were good at predicting the mesh bulge < 0.5 m and wire rupture classes. The lower recall score obtained for the mesh bulge > 0.5 m class indicates that these models suffered in identifying data in this class. This was because there was a high overlap between the mesh bulge > 0.5 m class and the other two.

5.4.4 Machine learning as a tool to estimate the performance of bolted steel mesh

Current bolted mesh design methods only consider the maximum load capacity of the mesh and do not examine the mesh displacement that may occur on the rock slope. The developed machine learning model can help overcome this limitation. The predictive models can be used to estimate the mesh performance including mesh bulge and mesh wire rupture. The predictive models can be used to improve existing design methods by adding a check of the mesh performance, thus including the assessment of mesh displacement.

The flow chart in Figure 5.20 shows the validation process. A geotechnical investigation of a rock slope can determine the following features: slope angle, expected rock block volume, critical joint dip, and joint friction angle. A mesh type, bolt pattern and bolt spacing can be selected. Based on the desired bolt locations in the slope, the rock position in a pattern of surrounding bolts can be estimated. These parameters can be used as input to the machine learning model to predict the mesh responses. If the model predicts wire rupture or mesh bulge > 0.5 m, then the mesh type or bolt arrangement should be changed. The process ends when the predicted mesh bulge is less than the selected criterion of 0.5 m. The choice of mesh wire rupture or a mesh bulge of 0.5 m as assessment criteria can be changed to different criteria based on relevant site conditions.

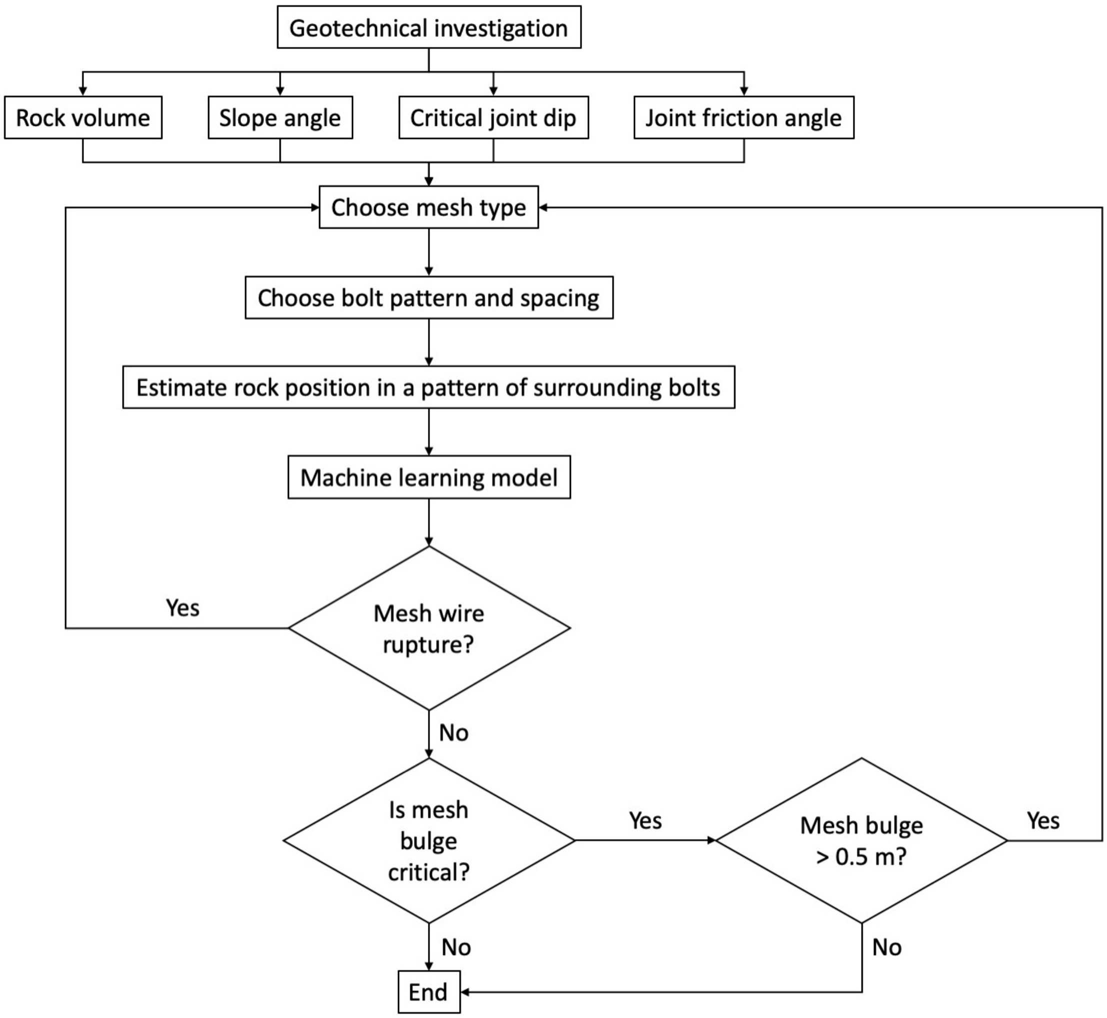

Figure 5.20 Flow chart for bolted mesh validation using the machine learning model

Although TECCO G65/3 mesh was used to develop the prediction models, the same DEM approach is applicable for other mesh types and different bolt patterns and spacings. The response of other mesh types and bolt arrangements can be obtained by conducting the DEM simulations. The new results could be added to the current simulation results to retrain the machine learning model to refine the predictive model.

The predictive model developed with the use of numerical modelling and machine learning provides a tool for checking the performance of mesh designs coming from existing design methods that ignore displacement. If the mesh is predicted to sustain unacceptably large displacements by the predictive model, engineers can change their design by reducing the bolt spacing or using a stronger mesh.

5.5 Summary

This chapter examines the response of bolted steel wire mesh to loading by a loose rock block between a pattern of rockbolts. Three components of this work are (1) the creation of discrete element models to simulate realistic field scenarios where an unstable rock interacts with the bolted steel mesh, (2) a parametric study of factors affecting the mesh performance based on DEM simulations, and (3) the development of a tool to estimate the mesh performance for bolted steel mesh for rock slope.

The DEM models were created to capture the response of bolted steel mesh to loads imposed by an unstable sliding rock using the open-source DEM code YADE. The DEM model used an assembly of particle elements connected by virtual springs to simulate the mesh and a polyhedral element to simulate the rock. The models allowed for large mesh deformations and wires could break.

The parametric study on the mesh response involved 900 DEM simulations of steel mesh for three bolt spacings (2 × 2 m, 2.5 × 2.5 m, and 3 × 3 m) considering five influence factors: rock volume and shape, sliding angle, slope angle, friction angle and rock position. Two kinds of mesh responses were tracked in the simulations: (1) the mesh stopped the rock motion with no mesh damage and (2) one or more wires broke in the mesh. The simulations used the mechanical properties of high-tensile TECCO 65/3 steel mesh. The results showed that the mesh typically experienced a bulge of 0.4 to 0.8 m for a rock volume less than 3 m^3 for the scenarios that were simulated. The mesh bulge increased as the rock volume, sliding angle, slope angle, and bolt spacing increased. The mesh bulge is smaller if the unstable rock is located closer to the bottom bolt. The rock volume and sliding angle have the largest influence on the rupture of mesh wires. Slope angle and rock position have a minor influence on wire rupture. The bolted steel mesh was unlikely to experience wire ruptures if the net load from the rock block was less than 8 kN, but wire ruptures were likely if the load was larger than 13 kN. For loads between 8 and 13 kN, wires may or may not rupture in the mesh depending on the other influence factors.

The DEM simulation results were used to create mesh performance prediction models by using a support vector machine (SVM) learning approach. The SVM models can predict the behaviour of bolted steel mesh loaded by a sliding rock block for a range of input conditions. Different mesh performance criteria, such as the mesh bulge, can be selected to define classes in an SVM model. Three classes of mesh performance were used: (1) mesh bulge < 0.5 m without breaking a wire, (2) mesh bulge > 0.5 m without breaking a wire, and (3) > 1 wire in the mesh ruptures. The predictive ability of the SVM models with a polynomial or a radial basis function kernel was good.

The development of the DEM models of steel wire mesh and using the simulation outcomes to construct SVM models is part of an approach to develop tools to estimate the performance of bolted steel mesh. Engineers can first use the current methods to design the bolted steel mesh, then apply the predictive model to assess the mesh performance on a rock slope. If the mesh performance is not satisfactory, the design can be improved by reducing the bolt spacing or choosing a stronger mesh to limit the mesh displacement.

Chapter 6: Investigation of bolted steel mesh to support a sliding and a toppling rock block using DEM

6.1 Overview

It is important to reveal the interaction between the unstable rock and the bolted steel mesh. A better understanding of the deformation and load transfer in the bolted mesh system is beneficial to more effective design. This chapter presents numerical studies on the behaviour of the bolted steel mesh to resist a sliding and a toppling block using discrete element modelling. The displacement of the blocks and mesh was analyzed, as well as the load on the blocks and rockbolt plates. The simulation results provide a better insight into the force-displacement relationship of the bolted mesh system. Recommendations are also made to improve mesh efficiency.

6.2 Sliding block supported by bolted steel mesh

One situation in rock slope stabilization is to stabilize single rock blocks. When it is impossible to place rockbolts through the unstable rock block or if it is expected that the rock block will disintegrate around the rockbolts, then rockbolts can be arranged around the critical area (Flum et al. 2008). Figure 6.1a and b show a vertical cross-section and a horizontal cross-section, respectively. It is essential to estimate the tension force in the steel mesh through longitudinal restraint ($F_{1\text{-mesh}}$, which equals the resultant of T_1 and T_2) and transverse restraint ($F_{2\text{-mesh}}$, which equals the resultant of T_3 and T_4) to select the appropriate mesh and to design the corresponding rockbolts. This section presents an analysis of the response of the steel mesh under a load from a sliding rock block and the load transfer mechanism using discrete element simulations.

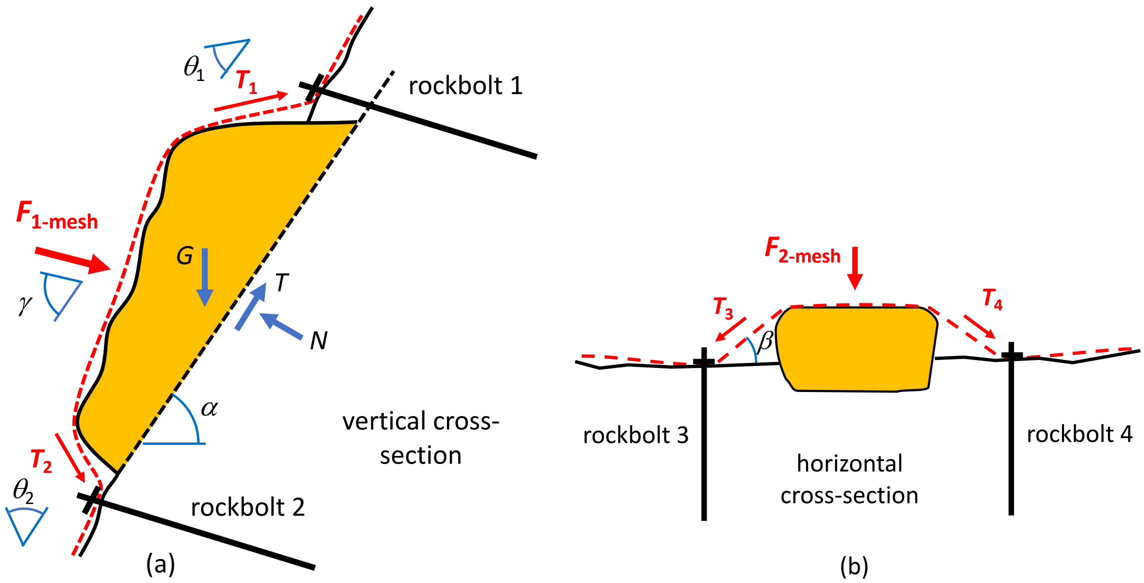

Figure 6.1 Schematic drawing of tension forces in steel mesh in support of a sliding rock block

6.2.1 Modelling of a sliding rock supported by bolted steel mesh

A DEM model comprising a rock block, slope face, and bolted steel mesh was constructed to study the displacement and load transfer between a sliding rock block and the bolted steel mesh. The calibrated TECCO G65/3 mesh model in Section 3.5.4 is used in all the simulations. This section describes the model construction process.

The rock block size in the simulations is 1.5 × 2 × 0.5 m with a density of 2600 kg/m^3 (block weight = 38.5 kN). The rock block model is made of 2204 overlapping particles (overlap radius = 0.1 m) that are clumped together (Figure 6.2). The slope face is made with triangular facet elements. The Young's modulus and friction angle of the rock block and the slope surface are set to 50 GPa and 30°, respectively.

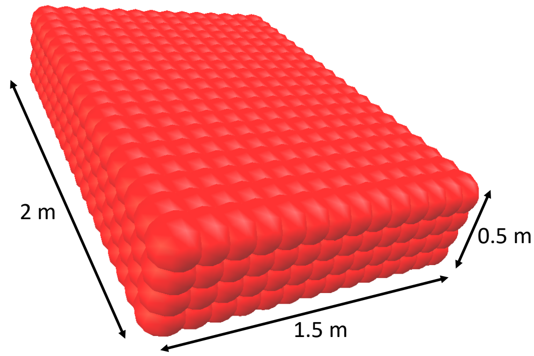

Figure 6.2 Rock block model

Figure 6.3 shows the process of model construction. First, the slope surface is generated at a 30° inclination, and the rock block is attached to the slope surface. Then, a steel mesh model is generated in front of the slope with an initial mesh size of 8×8 m^2. The top edge of the steel mesh model is aligned with the top of the slope surface. There is an initial angle between the steel mesh and slope face to make sure no overlaps between the particles of mesh and rock block. The particles on the top edge of the mesh model are fixed in the directions that are perpendicular and parallel to the rock face. This boundary condition simulates the anchorage of the steel mesh to the top of the slope. The other boundaries of the steel mesh are set to free in all directions. Next, the gravity is turned on to let the steel mesh drape freely to cover the rock block until equilibrium is obtained. Finally, four 'rockbolts' are installed to support the rock block.

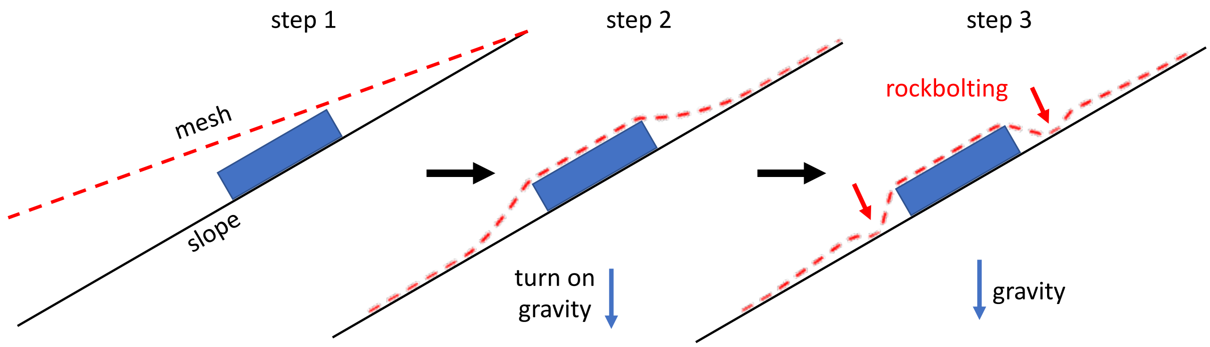

Figure 6.3 Process of model construction showing the actual profile of the steel mesh

The commonly used two bolt patterns, pattern A and pattern B, are simulated, as shown in Figure 6.4. The effect of the rockbolt plates is modelled by fixing the movement of mesh particles in all directions at locations where the plate would be located. The simulated rockbolt plates are the 'spike plate P33' with a dimension of 330 × 190 mm. Thus, six particles are needed to simulate the effect of one rockbolt plate because they directly contact the plates (Figure 6.4). The installation process is simulated by moving the 'rockbolt plates' in a direction that is normal to the slope face to pretension the steel mesh. The 'rockbolts' are installed in a top-down sequence. The movement of the particles that represent the rockbolt plates is stopped once the plate contacts the slope surface. The horizontal and vertical spacing of rockbolts are 2 m and 3 m in pattern A, and 2.5 m and 3 m in pattern B. After installing the rockbolts, the resultant force on the rock block is about 5 kN for pattern A, and about 36 kN for pattern B. The resultant force on the rock block for pattern B is much larger than for pattern A because the bolts in pattern B are closer to the rock block, which results in more pretension in the mesh wires.

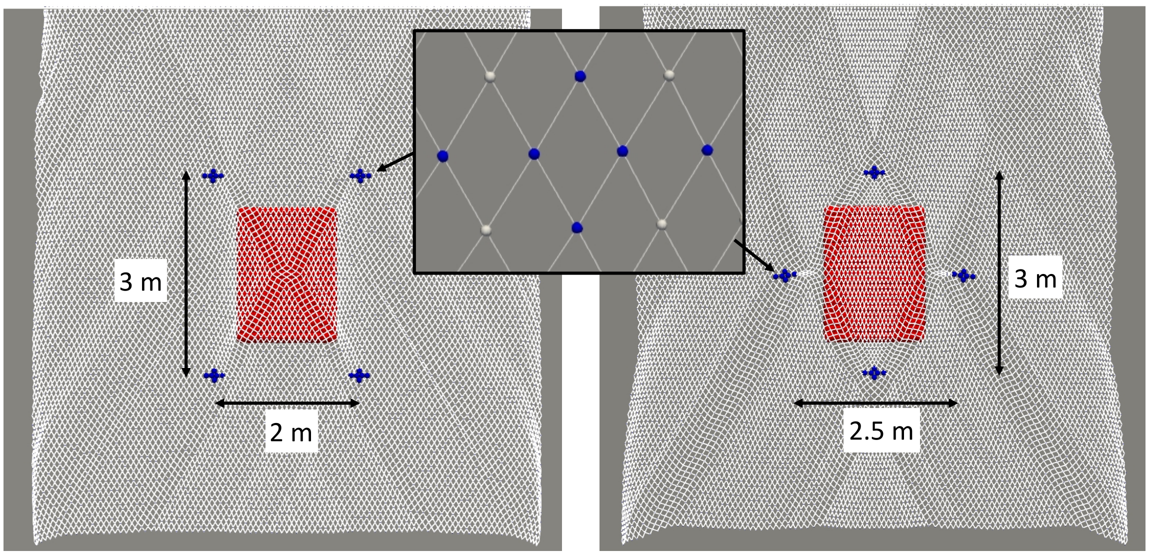

(a) Bolt pattern A (b) Bolt pattern B

Figure 6.4 DEM model of rock block and bolted steel mesh with inset showing six particles used to represent the rockbolt plate

Figure 6.4 shows the two constructed DEM models. The simulations start by releasing the rock block models from the slope surface. During the simulations, the displacement and force on the rock block are recorded, as well as the force on each rockbolt plate. Different scenarios are simulated by progressively increasing the angle of the sliding plane to 85° in 5° increments.

6.2.2 Displacement of rock block and steel mesh

As expected, the rock block moves when the sliding angle increases to 35° for bolt pattern A. The support force provided by the bolted mesh is too small to provide enough frictional resistance to stop the block from sliding. The mesh becomes loose after the rock block slides. The rock block continues to slide away between the lower two bolts, as shown in Figure 6.5. Therefore, it is more likely for rocks to pass between bolts when using bolt pattern A because there is no bolt to stop them on their way.

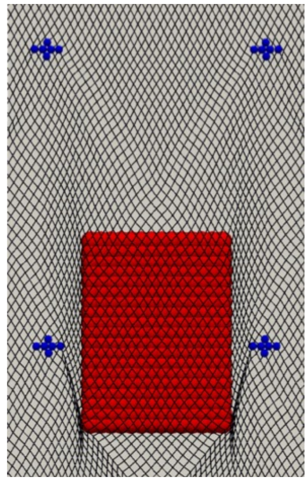

Figure 6.5 Rock block sliding between bolts for bolt pattern A

For bolt pattern B, the bolted steel mesh successfully stops the rock block in all simulations. Figure 6.6 shows the maximum displacement of the rock block along the sliding direction for different angles of the sliding plane. The maximum displacement of the rock block increases as the angle of the sliding plane increases when the sliding angle is larger than 55°. The final displacement of the rock block along the sliding plane ranges from 0.14 to 0.25 m.

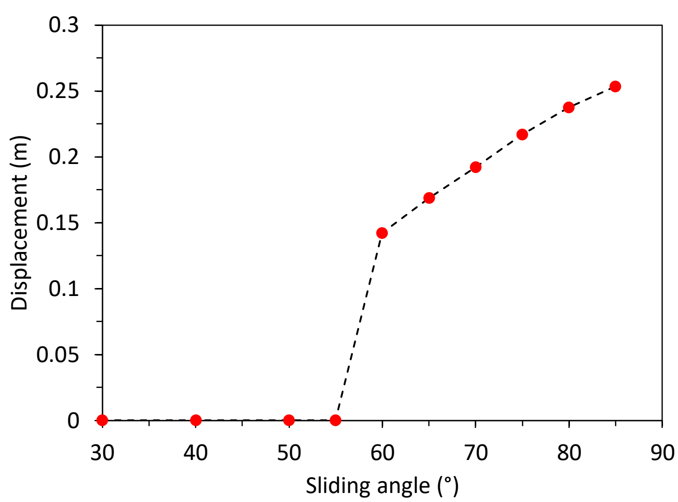

Figure 6.6 Displacement of rock block at various sliding angles for bolt pattern B

The movement of rock block deforms the steel mesh. Figure 6.7a and b show the vertical and horizontal profiles of the steel mesh. As the rock block slides downwards, it pushes the steel mesh below the block and stretches the mesh above (Figure 6.7a). However, the profiles of the steel mesh in the transverse direction display little change (Figure 6.7b). This is because the thickness of the rock block in the simulations is constant, and the rock block slides beneath the steel mesh without catching the steel mesh.

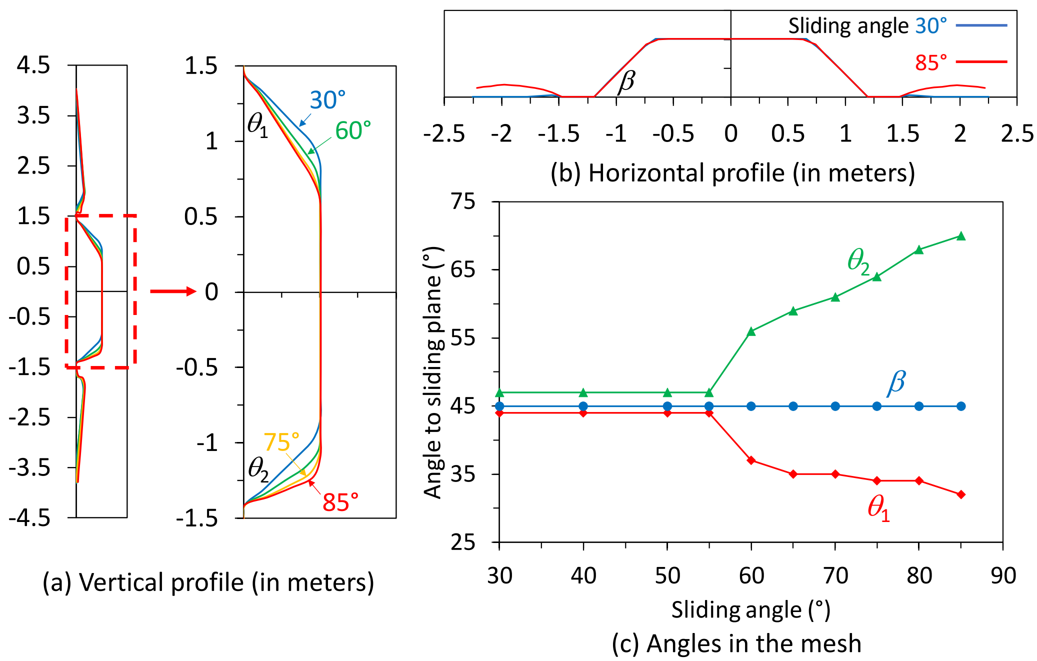

Figure 6.7 Geometry of steel mesh with various sliding angles for bolt pattern B

Figure 6.7c shows the angle between the steel mesh and the sliding plane in the upslope direction (θ_1), and the downslope direction (θ_2), and along the transverse direction (β). For sliding angles from 30° to 55°, the rock block is kept at its original position, resulting in no changes in the angles between the steel mesh and the sliding plane. The geometry of steel mesh depends on the geometry of the rock block and the distance between rockbolts. In this simulation, the angles were around

44 - 47°. When the sliding plane angle is larger than 55°, the rock block moves, and the geometry of the steel mesh changes accordingly. The angle θ_1 decreases, and θ_2 increases as the sliding angle increases because the rock block pushes the steel mesh below the block and stretches the steel mesh above the block.

6.2.3 Load transfer between a rock and bolted steel mesh

Because the bolted steel mesh failed to stop the sliding of the rock block in bolt pattern A, only the load transfer between the rock and bolted steel mesh for bolt pattern B is presented for this section.

Figure 6.8 shows the distribution of the force carried by the mesh wires when the sliding angle is 60°, 75°, and 85°. Note that the maximum force in the plots is set to 6.5 kN for better visualization. The force distribution in the wires shows a diamond shape with corners at the rockbolts and covers the rock block underneath. The force is mainly carried along the wires that run from one rockbolt to another, which transmits the rock block loads to the rockbolts. As the sliding angle increases, the loads on the wires increase. The maximum force in the wires for these sliding angles is 5, 7.2, and 10 kN, respectively.

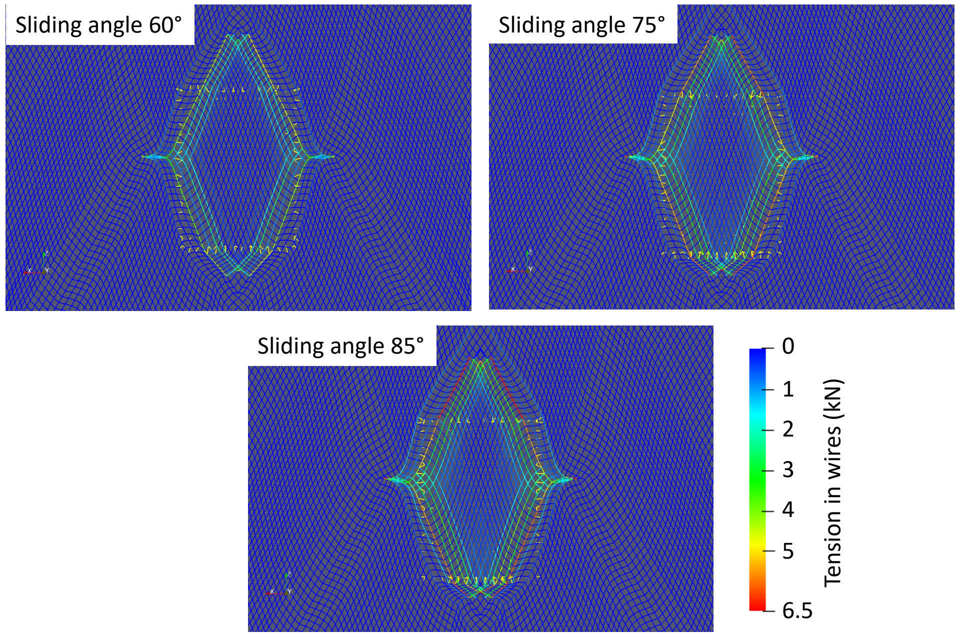

Figure 6.8 Distribution of axial force in wires in steel mesh

The resultant force on each rockbolt as the rock block moved with sliding angles of 60° and 85° are shown in Figure 6.9. For different sliding angles, the force on the top and bottom rockbolts is higher than the rockbolts at each side of the rock block. The force on a rockbolt first decreases when the block initially starts to move then increases as the deformation of the block increases. The reason is that the steel mesh is tensioned at the beginning because of the installation of the rockbolts, but relaxes slightly when the block moves. After further deformation, the steel mesh is tightened and carries the load again.

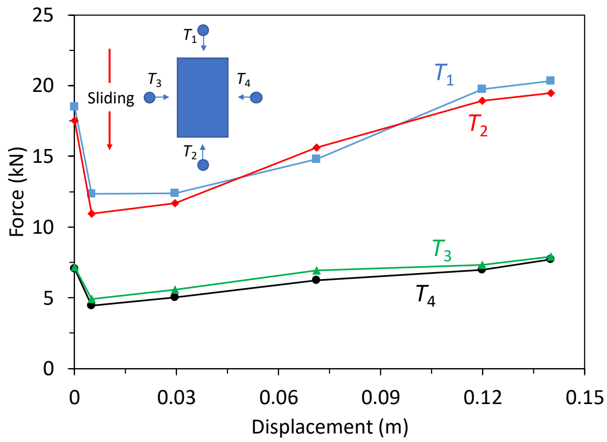

(a) Sliding angle 60°

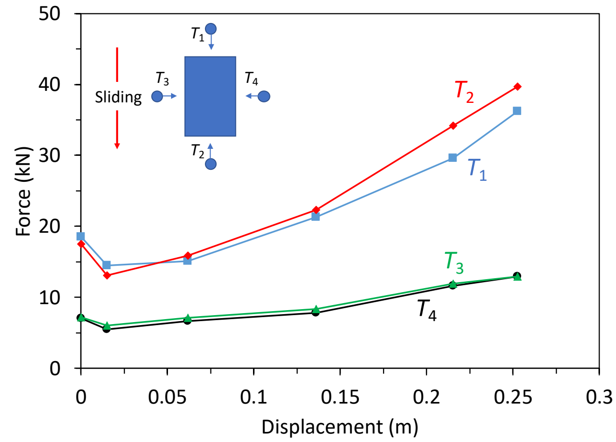

(b) Sliding angle 85°

Figure 6.9 Resultant force on each rockbolt during deformation of rock block with sliding angle of 60° and 85°

At a sliding angle of 60°, the load on the rockbolt at the top is higher than the bottom at the beginning. Then, the load on the bottom bolt plate gradually becomes larger than the load on the top bolt plate as the deformation increases. However, the top bolt plate carries a higher load than the bottom plate at the end of the simulation. For a larger sliding angle (85°), the load on the rockbolt at the top is higher than the bottom at the beginning, but the load on the bottom rockbolt increases faster than the load on the top rockbolt as the deformation of rock block increases. The rockbolt below the block carries the highest load when the slip plane is steep.

The maximum force acting on each rockbolt occurs when the block stops moving. These are shown in Figure 6.10a for different sliding angles. The insert sketch shows the force and its direction on each rockbolt plate. The forces on the top and bottom rockbolts (T_1 and T_2) are higher than the forces in the rockbolts at each side of the rock block (T_3 and T_4) for all sliding angles. Also, there is no significant difference between T_3 and T_4 because of the symmetric positions of these two rockbolts.

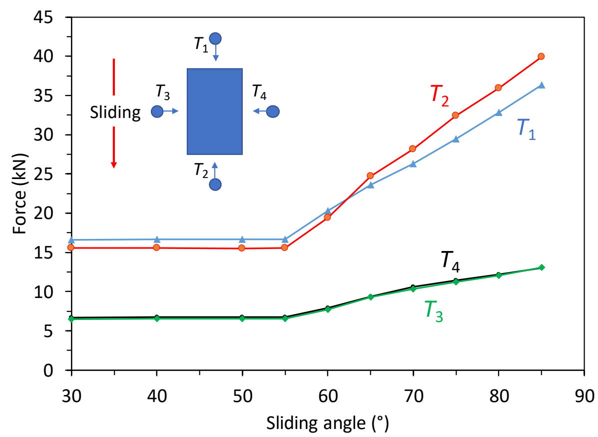

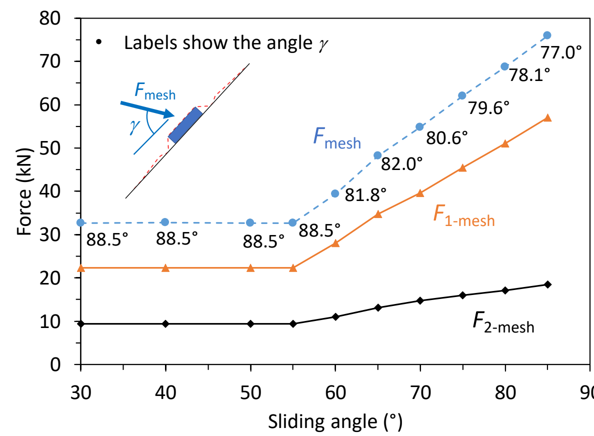

Figure 6.10 Resultant force on each rockbolt and rock block

For a sliding plane angle from 30 to 55°, when the steel mesh holds the rock block at its original position, the force on the rockbolts remains nearly the same value with T_1 slightly larger than T_2 (16.6 vs. 15.5 kN), and T_3 and T_4 around 6.6 kN. When the sliding angle exceeds 55°, the force on rockbolt plates increases. However, T_2 becomes larger than T_1 when the sliding angle is somewhere between 60° and 65° and larger.

The simulations also track the resultant force acting on the rock block that is generated by the steel mesh (F_{mesh}). Figure 6.10b shows these data. The angle between F_{mesh} and sliding plane, γ, decreases as the sliding angle increases. This means that the support force from the mesh is inclined towards the upslope direction when the slope angle is steeper. The resultant force of T_1 and T_2 (longitudinal restraint $F_{1\text{-mesh}}$), and the resultant force of T_3 and T_4 (transverse restraint $F_{2\text{-mesh}}$) are compared with F_{mesh} in Figure 6.10b and Table 6.1. The support force of steel mesh in both directions increases as the sliding angle increases. The proportion of the longitudinal restraint contributing to the block stabilization increases as the sliding angle increases, while the proportion of transverse restraint decreases. The support provided by the longitudinal restraint accounts for about 68% - 75% of the load, while about 26% - 29% is provided by transverse restraint. Thus, the rockbolts in the longitudinal direction are more significant than the bolts in the transverse direction.

Table 6.1 Load carried by longitudinal restraint vs. transverse restraint

Sliding angle	$F_{1\text{-mesh}}/F_{\text{mesh}}$	$F_{2\text{-mesh}}/F_{\text{mesh}}$
30°	68.3%	28.8%
40°	68.4%	28.8%
50°	68.3%	28.9%
55°	68.4%	28.9%
60°	71.2%	27.9%
65°	72.0%	27.2%
70°	72.2%	26.8%
75°	73.3%	25.7%
80°	74.3%	24.9%
85°	75.1%	24.3%

6.3 Toppling block supported by bolted steel mesh

The toppling failure of rock blocks is another common failure mechanism on rock slopes. The current design methods are all based on a sliding failure assumption, which is not suitable for the toppling failure of rock blocks. It is recognized that the steel mesh may only provide a small amount of support force because it is difficult to pre-stress the mesh properly during bolt installation (Blanco-Fernandez et al. 2013). However, a low support force may be enough to stabilize some toppling rock blocks depending on the rock block geometry and the equilibrium of moments. Thus, it is necessary to understand the performance of bolted steel mesh when stabilizing a toppling rock block to improve the design. This section presents an analysis of the response of a toppling rock for different support forces provided by bolted steel mesh using the discrete element simulations.

6.3.1 Modelling of a toppling rock supported by bolted steel mesh

The components of the DEM model are the steel wire mesh, the rock surface and the rock block (Figure 6.11a). The rock block size is $1 \times 1 \times 1$ m^3 with a density of 2600 kg/m^3 (weight = 26 kN). The rock block model is made of 729 overlapping and clumped particles (overlap radius = 0.1 m), as shown in Figure 6.11b. The slope face is made by the triangular facet elements. There is a 0.25 m offset between the upper half and lower half of the slope face, which forms a small bench. The Young's modulus and friction angle of the rock block and the slope surface are set to 50 GPa and 30°, respectively.

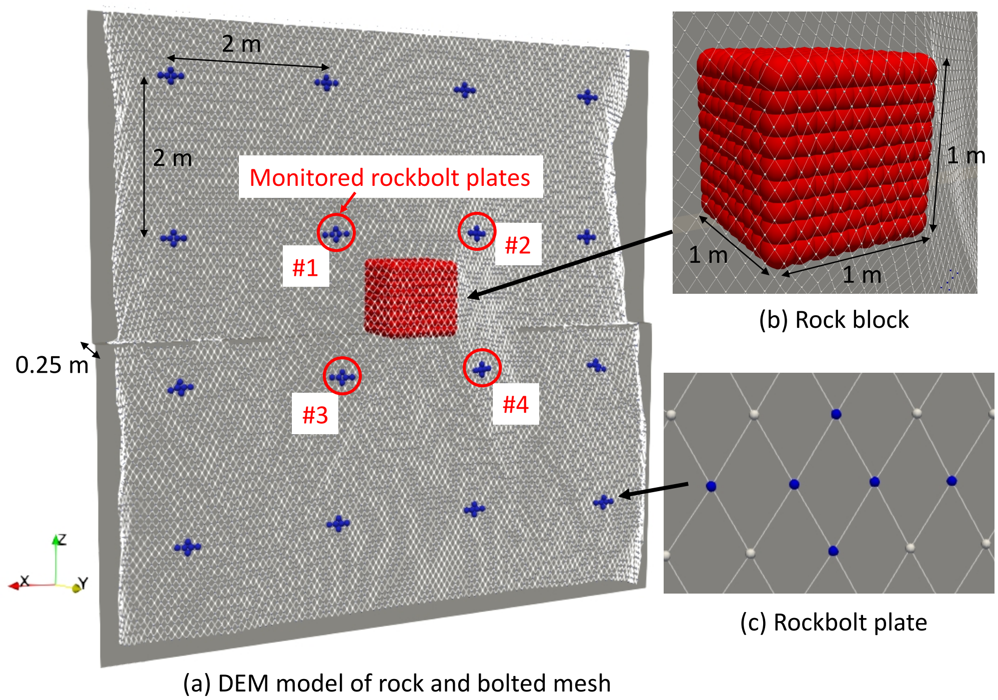

Figure 6.11 DEM model of a toppling rock block with bolted steel mesh

Figure 6.12 shows the process of model construction. First, the slope face is generated, and the rock model is placed on the small bench of the slope face. Then, a steel mesh model is generated in front of the slope with an initial size of 8×8 m^2. The top edge of the steel mesh model is aligned with the top of the slope surface. The initial angle between the steel mesh and slope face is 20° to ensure no overlap occurs between the mesh and rock block. The particles on the top edge of the mesh model are fixed in the directions that are perpendicular and parallel to the rock face to simulate the anchorage of the steel mesh to the top of the slope. The other boundaries of the steel mesh are set to free in all directions. Next, gravity is turned on to let the steel mesh drape freely to cover the rock block until equilibrium is reached. There are 16 rockbolts installed using pattern A to support the rock block. The horizontal and vertical spacing between the bolts is 2 m. The installation process is simulated by moving six particles at each 'rockbolt plate' location in a direction normal to the slope face to pretension the steel mesh. All 'rockbolt plates' are moved at the same time. Once a rockbolt plate touches the slope face, the movement of the six particles is fixed in all directions (Figure 6.11c), which is the same as Section 6.2.1.

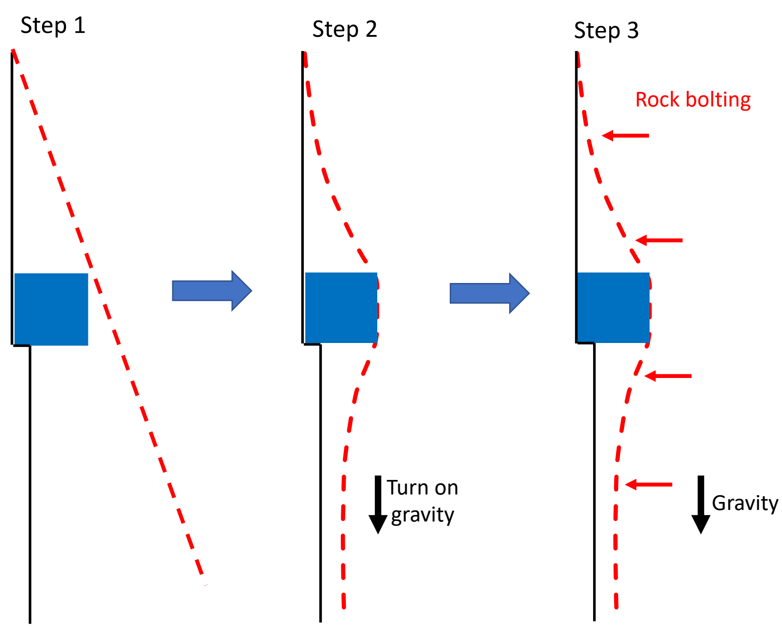

Figure 6.12 Model construction process

6.3.2 Support force on rock block during installing rockbolts

The support force on the rock block and the force on the four nearest rockbolt plates around the rock (Figure 6.11a) are recorded during the rock bolting process. The monitored forces are in a direction perpendicular to the slope face. The support force on the rock block and the force on the 'rockbolt plates' increases as the displacement of the 'rockbolt plates' increases, as shown in Figure 6.13. The forces on the upper two bolts (#1 and #2) are larger than that on the lower two bolts (#3 and #4). The support force on the rock block is much higher than the force applied on a single rockbolt plate.

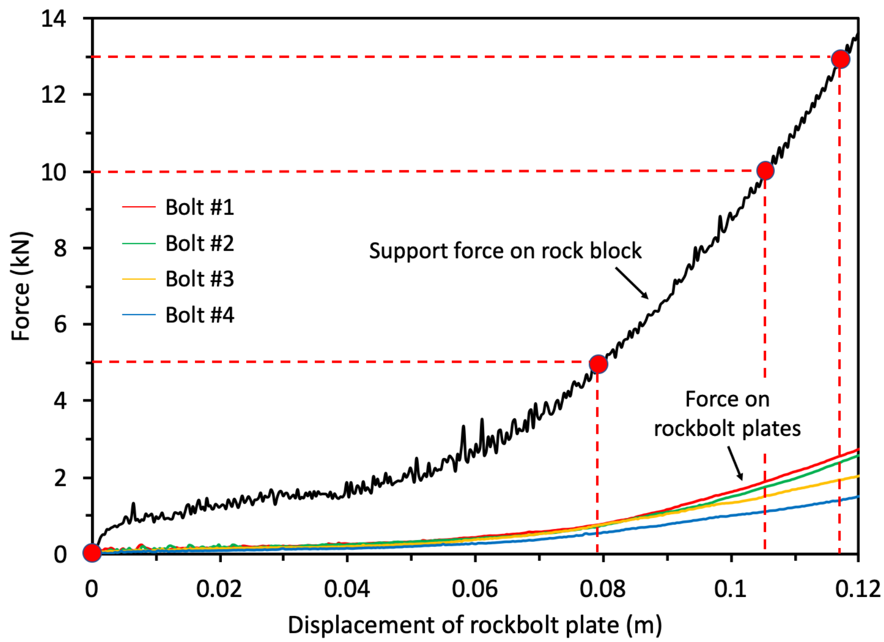

Figure 6.13 Support force on rock block versus displacement of rockbolt plates

Theoretically, the minimum support force to stop the rock block from toppling can be determined. This force is $F_{\text{support}} = \frac{26\ \text{kN} \cdot 0.25\ \text{m}}{0.5\ \text{m}} = 13\ \text{kN}$. As shown in Figure 6.13, when the support force reaches 13 kN, the force on the rockbolt plates around the rock block ranges from 1.5 to 2.3 kN. The displacement of the rockbolt plates is close to 0.12 m. This means that moving the rockbolt plates approximately 0.12 m during installation generates about 13 kN support force on the rock block.

Figure 6.14 shows the tensile force distribution in the mesh wires when the support force on the rock is 13 kN. The force is mainly transferred from the rock block to the nearest four bolts above and four bolts below the rock. The tensile force in the mesh wires is much smaller than the maximum allowable tensile force for these 3 mm wires (12.5 kN).

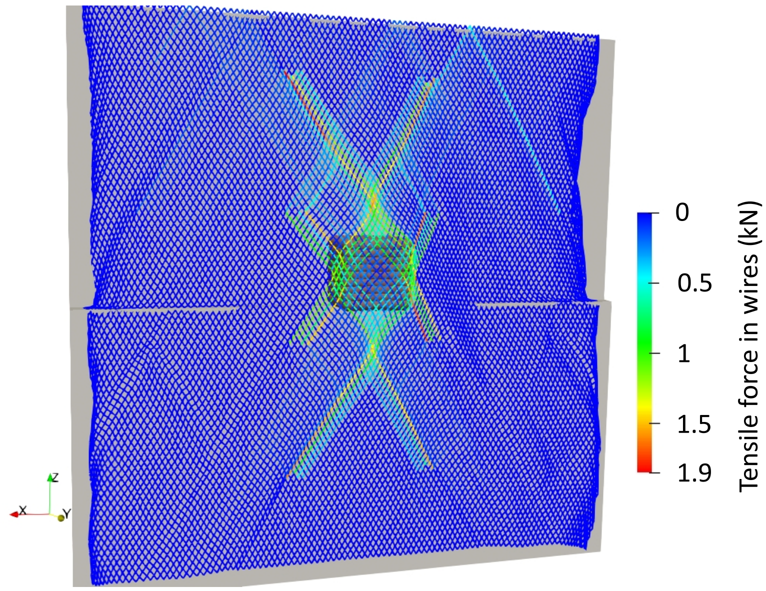

Figure 6.14 Tensile force distribution in mesh wires when support force on rock is 13 kN

6.3.3 Effect of support force of bolted steel mesh to resist rock toppling

For a comparison purpose, when the support force on a rock block reached 0, 5, 10, and 13 kN, the rockbolt plates are stopped, and their movements are fixed in all directions, as shown in the four red points in Figure 6.13. Four different models are saved at these four points to investigate the rock block trajectory under different initial support forces. A support force of zero represents no steel re-stressing of the mesh by the rock bolting. The simulations initiate by releasing the rock block under gravity. During the simulations, the trajectory of the centroid of the rock block is monitored. The simulations are stopped if an equilibrium state is obtained or the rock falls off from the slope face.

The bolted steel mesh held the rock block on the slope in all four simulations. Figure 6.15 shows the trajectories of the centroid of the rock blocks with various initial support forces. When the steel mesh is not pre-stressed by bolts (zero initial support force on rock), the displacement of rock block is the largest among the four situations. As the initial support force increases, the displacement of the rock block decreases. A larger initial support force also keeps the trajectory of the rock block closer to the slope face. With a support force of 13 kN applied on the rock block, the displacement of the rock block is very small, which means that the bolted steel mesh holds the rock at its original position as expected.

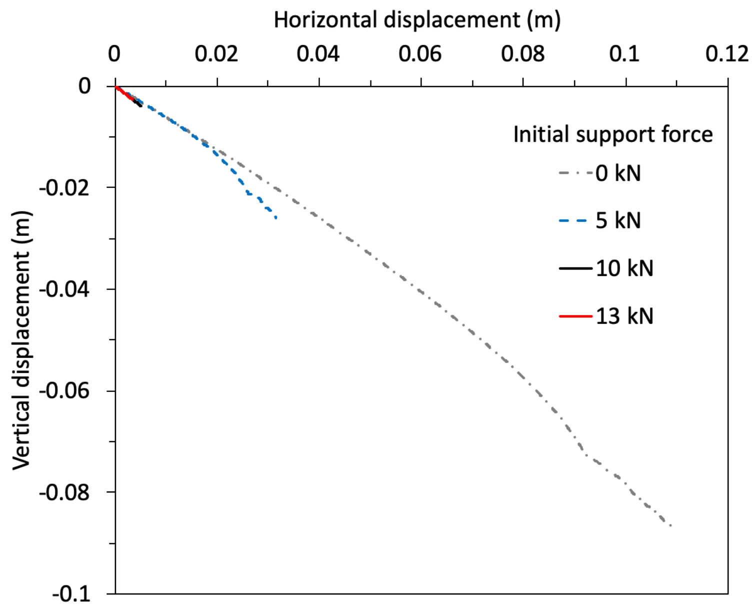

Figure 6.15 Trajectories of the rock block centroid

6.4 Influence of bolting sequence

Different bolting sequences may cause different mesh behaviour. This is because the tension in the steel mesh varies as the bolting sequence changes. This section discusses the influence of two different bolting sequence on the support force of the bolted steel mesh using discrete element modelling. The simulations were conducted on a convex slope face. The two bolting sequences are from top to bottom and from bottom to top. The purpose of the simulations is to highlight the influence of the installation process of bolts.

6.4.1 Modelling of rock slope with a convex profile

The DEM model comprises a steel wire mesh, a rock surface, and a rock block, as seen in Figure 6.16. The rock block size is $1 \times 1 \times 0.5\ m^3$ with a density of 2600 kg/m^3 (weight 13 kN). The rock block model is made of 324 particles with an overlap of their radius and clumped together. The block model is attached to a plane rock face model. The rock face model is made using triangular facet elements. A steel mesh model is draped in front of the rock model. The initial mesh size is $8 \times 8\ m^2$. The particles on the top edge of the mesh model are fixed in both the vertical direction and horizontal direction perpendicular to the rock face to simulate the anchorage of the steel mesh at the top. The other boundaries of the steel mesh are set to be free in all directions.

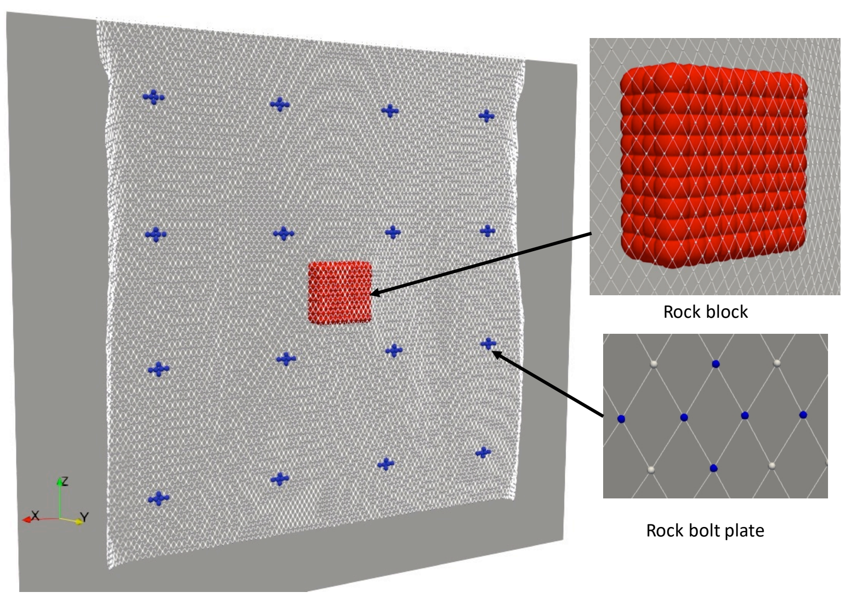

Figure 6.16 DEM model of rock block with bolted steel mesh

The effect of the rockbolt plates is modelled by fixing the movement of 'mesh' particles that directly contacted the plates, as shown in Figure 6.16. The rock bolts and plates (16 in total) are modelled in a bolt pattern A with a 2 m spacing in four rows and four columns. The installation process is simulated by moving the ‘rockbolt plates’ towards the rock face to pretension the steel mesh. The ‘rockbolt plates’ are stopped when they contact the rock face.

The first simulation applies a top-to-bottom bolting sequence, while the second simulation uses the opposite sequence. The models ran to an equilibrium state before installing each row of rock bolts.

6.4.2 Support force of different bolting sequences

Figure 6.17 shows the profiles for both simulations. When bolting from top to bottom, the changes in the profiles are below the rock block because the installation of rockbolts pulls up the loose steel mesh from below. There is no significant change in the profile when bolting from bottom to top because the mesh is secured at the bottom by the bolt plates.

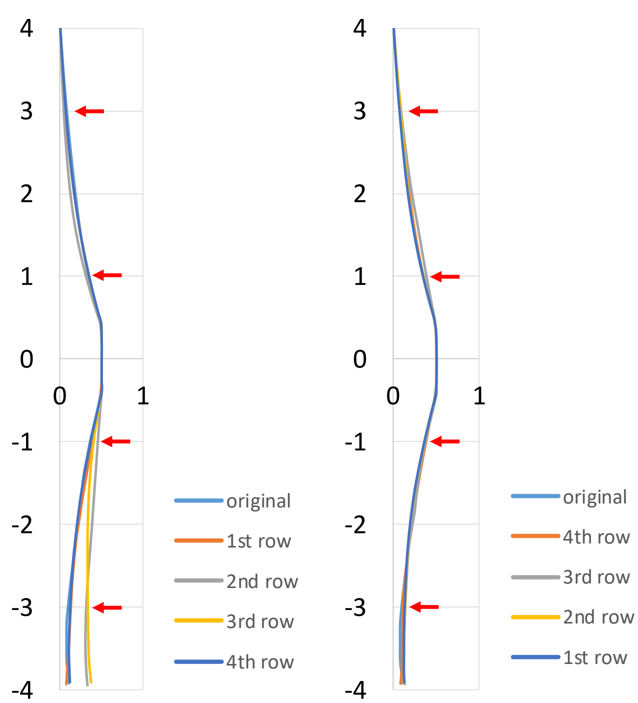

Figure 6.17 Vertical profile of the steel mesh in the middle section (in metres)

The bolting sequence affects the tensile force distribution in the steel mesh, as shown in Figure 6.18. The tensile force in the mesh wires concentrates on the upper edge of the rock block when bolting from top to bottom. Because the steel mesh above the rock block is secured at first, bolting the steel mesh below the rock block stretches the steel mesh downwards. On the contrary, the tensile force concentrates on the bottom edge of the rock block when bolting from bottom to top. A smaller support force at the top edge of the rock block is needed to resist its toppling because it has a larger moment arm about the rotation base. Therefore, bolting from top to bottom better for preventing rock block toppling using bolted steel mesh.

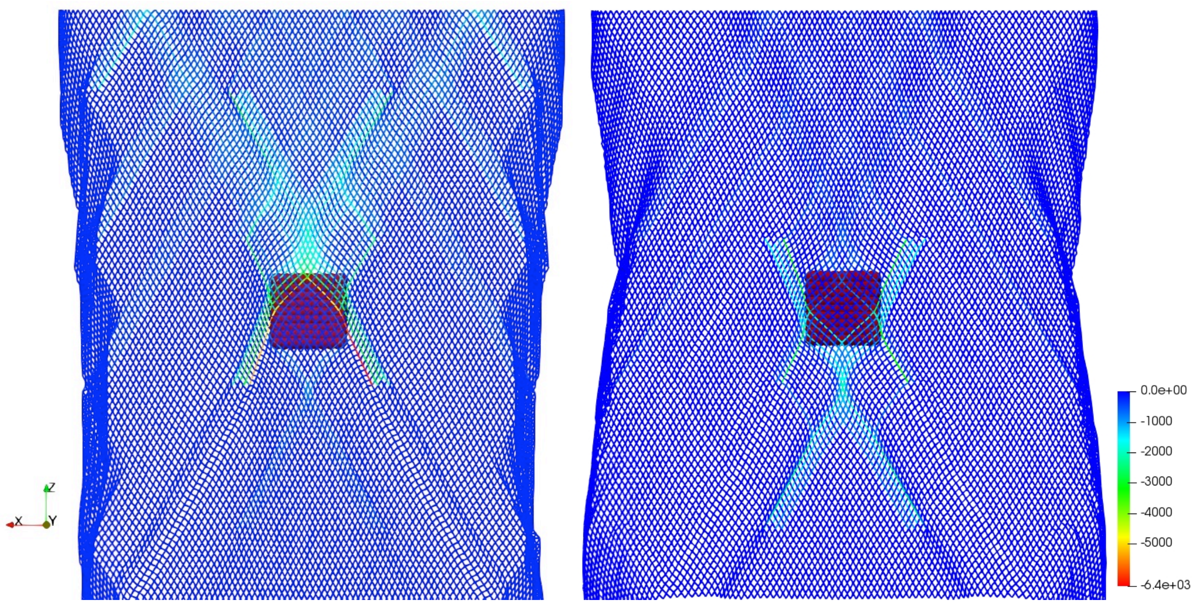

Figure 6.18 Tensile force distribution in the steel mesh

The final tensile force in the mesh wires around the rock block in a top-bottom bolting sequence is larger than in the bottom-top bolting sequence, resulting in a larger support force on the rock block as well (Figure 6.19). During bolting, the support force increases when installing the adjacent bolts around the block (second and third rows). This indicates that the bolted steel mesh can provide a certain amount of support force before rock block moves if the mesh is tensioned properly.

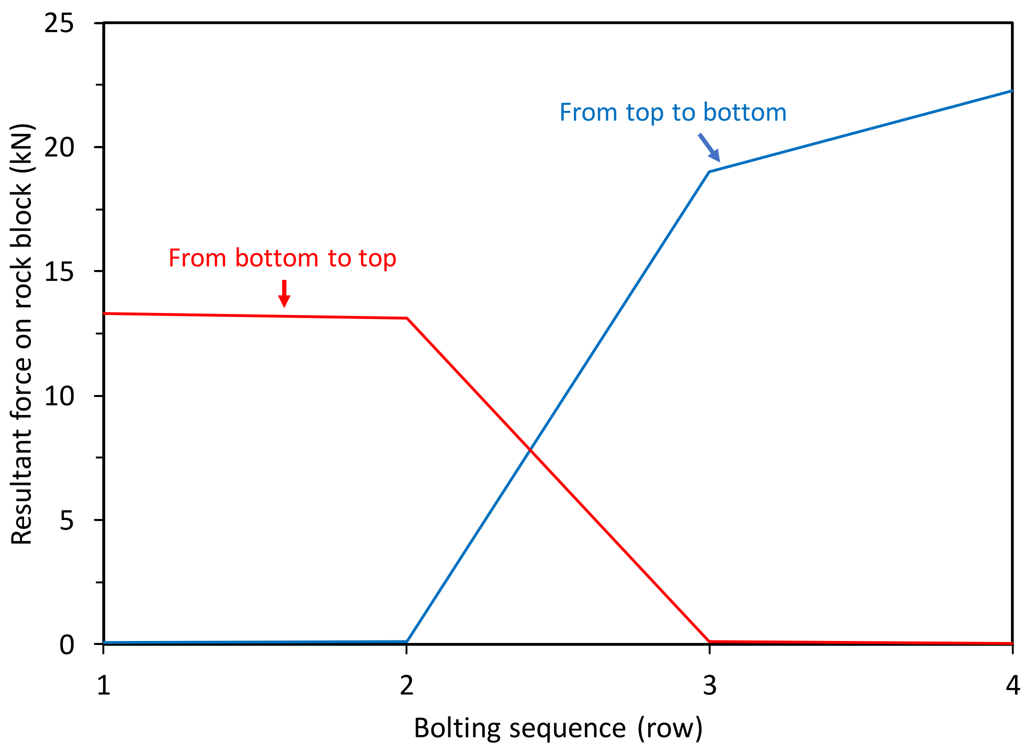

Figure 6.19 Resultant force on rock block during bolting process

6.5 Summary

This chapter presents numerical studies on the use of bolted steel mesh to support a sliding rock block and a topping rock block using the discrete element method (DEM). The rock block is simulated by clumped particle elements. The slope face is modelled by the triangular facet elements. The calibrated steel mesh model is used to hold the rock block. Two different types of models are constructed, one with a sliding rock and the other one with a toppling rock, to investigate the displacement and load transfer in the bolted steel mesh system.

The results show that the steel mesh can provide a sufficient support force to retain a sliding rock block on a slope face if the mesh is properly pre-stressed by rockbolts. Noted that the rock block may slide between the bolts if the bolts are aligned with each other in rows and columns. The force is mainly carried by the wires that run diagonally from one rockbolt location to another. The rockbolt above and below the rock block (longitudinal restraint) carries much more load than the rockbolts on either side of the rock block (transverse restraint). Also, the percentage of load carried by longitudinal restraint in the mesh increases as the sliding angle increases. The load on the rockbolts below the rock block is slightly larger than the load on the bolts above the rock block at steep sliding angles.

Using rockbolts to secure the steel mesh on the slope face can improve the performance of the steel mesh in resisting the toppling of rock blocks. A proper pretension on the steel mesh can hold a rock block at its original position. Results show that even if the mesh is not pre-stressed during rock bolting, the mesh still can still resist rock toppling, but a larger displacement may occur. It is recommended to install the rockbolts at the concave spots on the slope face to permit slight preloading of the mesh to gain better control of the displacement of the rock blocks. A top-to-bottom bolting sequence can provide a larger support force on the rock block.

Chapter 7: Case history: bolted steel mesh design for a rock cut

7.1 Background

This chapter presents a design of bolted steel wire mesh to stabilize a rock cut. The design applied the research outcomes from Chapters 4 to 6. The rock cut is beside Shannon View Drive, West Kelowna, British Columbia, Canada. The City of Kelowna plans to stabilize this rock cut. There is no bolted mesh present when this thesis was written. Figure 7.1 shows a plan view of the rock cut area. The bearing of the rock cut is 61°, which is about the same as Shannon View Drive. Figure 7.2 shows an oblique view of the rock cut area. The design is focused on the rock cut 1. There is another smaller rock cut located approximately 20 m east to the rock cut 1. Large blocks of rocks have already fallen from the face of the rock cut 2.

Figure 7.1 Plan view of rock slope area

Figure 7.2 Oblique view of rock cut area (from point cloud)

Figure 7.3 shows a front view of the rock cut 1. The rock consists of trachyandesite with minor intercalated pyroclastic deposits (Tempelman-Kluit 1989). A layer of pyroclastic rock (dark red area) locates in the middle part of the rock cut. Two nearly vertical dykes intrude into the trachyandesite. There are a ditch and a concrete barrier at the toe of the rock cut. The debris in the ditch mostly comes from the pyroclastic layer.

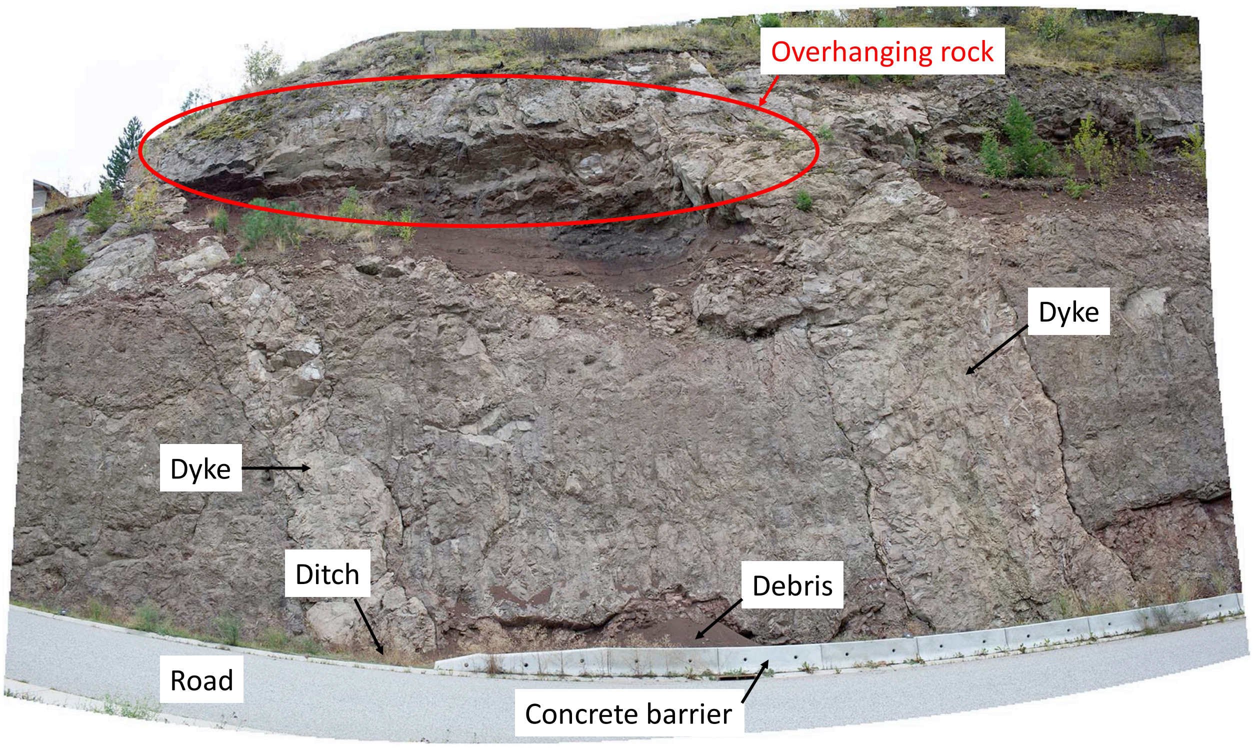

Figure 7.3 Front view of rock cut 1

Using the ISRM strength classification (ISRM 1981), the intact trachyandesite is strong to very strong strength (~70 to 140 MPa compressive strength), but the intercalated pyroclastic rock is weak to very weak (~ 2 to 10 MPa compressive strength). A big notch in the middle of the rock cut has formed as the pyroclastic layer gradually eroded. The big notch causes overhanging rock above the notch and between the two dykes. The span of the overhanging rock is about 20 m. The overhanging rock mass is jointed and fractured as shown in Figure 7.4, and rockfalls often occur. There was only a ditch at the toe of the rock cut before 2015. As talus accumulates in the ditch, falling rocks often bounce onto the road. A concrete barrier was built to minimize this situation. However, the fractured overhanging rock mass is still a potential threat to the public. For example, the length of the largest fallen rock block from the rock cut 2 is 3.9 m, and it has an estimated mass of approximately 24,000 kg, as shown in Figure 7.5. It did not cause any damage because there was a bench below to catch this rock. However, it is a huge concern that large rock blocks may fall from the rock cut 1 as well. Using steel wire mesh pinned by rock bolts can stabilize the rock cut and hold loose rocks.

Figure 7.4 Notch and fractured rock

Figure 7.5 Large fallen rock blocks

7.2 Field investigation using UAV

The field investigation applied the aerial photogrammetry technique to obtain the topography of the rock cut and map the geological structures. The aerial photographs were taken by a DJI Phantom 4 RTK unmanned aerial vehicle (UAV).

Ten survey targets were placed on the rock cut before taking the photos (five near the toe and five near the crown). The 3D coordinates of the targets were measured using a Leica TS06 total station. These targets were used as a reference to examine the scale of the 3D model that was georeferenced by the Global Navigation Satellite System (GNSS) in the UAV.

The field investigation conducted three UAV flights to take the aerial photographs: (1) 45 m above the road with a 45° shooting angle (124 images taken, 88 images used); (2) 60 m above the road with the camera shooting straight down (96 images taken, 95 images used); and (3) a free flight near the notch of the slope (133 images taken, 13 images used). Figure 7.6 shows these camera locations. The flight grids cover the rock cut. The free fights capture a higher level of detail in the overhanging rock because the first two flights are above the notch. The coordinates of the UAV recorded by the on-board GNSS system for each aerial photograph were corrected and transformed to the NAD83 Canadian Spatial Reference System / UTM zone 11 N with elevations given relative to the CGVD2013 vertical datum. This was done by submitting the RINEX observation data from the UAV to an online tool of Natural Resources Canada (https://www.nrcan.gc.ca/maps-tools-and-publications/tools/geodetic-reference-systems-tools/tools-applications/10925). These coordinates are for the image sensor in the camera for each image.

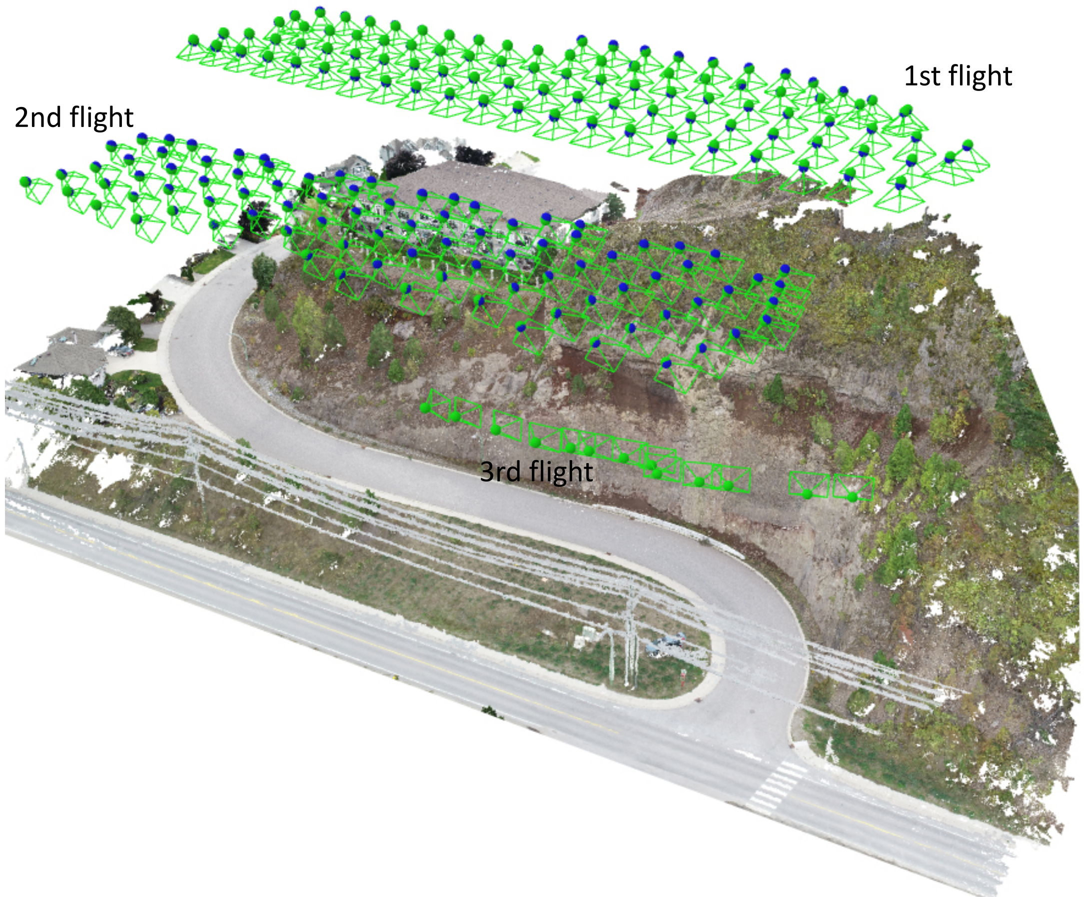

Figure 7.6 Point cloud of rock slope with camera locations from three flights

The aerial photographs were processed in Pix4D photogrammetry software (https://www.pix4d.com) by two different projects. One project processed the 183 images from the first two flights. The GNSS coordinates embedded in the EXIF header for each image were not used, instead, the UTM coordinates of the camera were used. The other project processed the 13 images from the third flight separately from the first two flights using an arbitrary coordinate system. The reason is that the free flight did not have the RINEX file to correct and transform their coordinates. Three common points that were identified in both projects to enable the merging of the two projects. For the merge project, 196 images were processed using the structure-from-motion algorithms to generate a dense and accurate point cloud with 15.9 million points, and an orthophoto of the area. The relative coordinate accuracy was estimated to be 20 mm based on a comparison of ten distances between the 10 survey targets calculated from 3D target locations measured with the total station and from the point cloud.

7.3 Rock cut characterization

Figure 7.7 shows the joints in the rock mass. The orientations of joints in the rock mass were measured using the Compass plugin in CloudCompare (Thiele et al. 2017). Figure 7.8 shows a stereonet plot of the measured joint orientations. The main joint set is likely roughly parallel to the upper and lower boundary of the lava flow. The mean orientation of the main joint set is 35°/145° (dip/dip direction). The other joints are the columnar joints that were formed during the cooling of the lava. The orientations of these columnar joints are nearly perpendicular to the main joint set. As shown in Figure 7.8, the poles of columnar joints spread along the great circle (red circle) corresponding to the mean orientation of the main joint set.

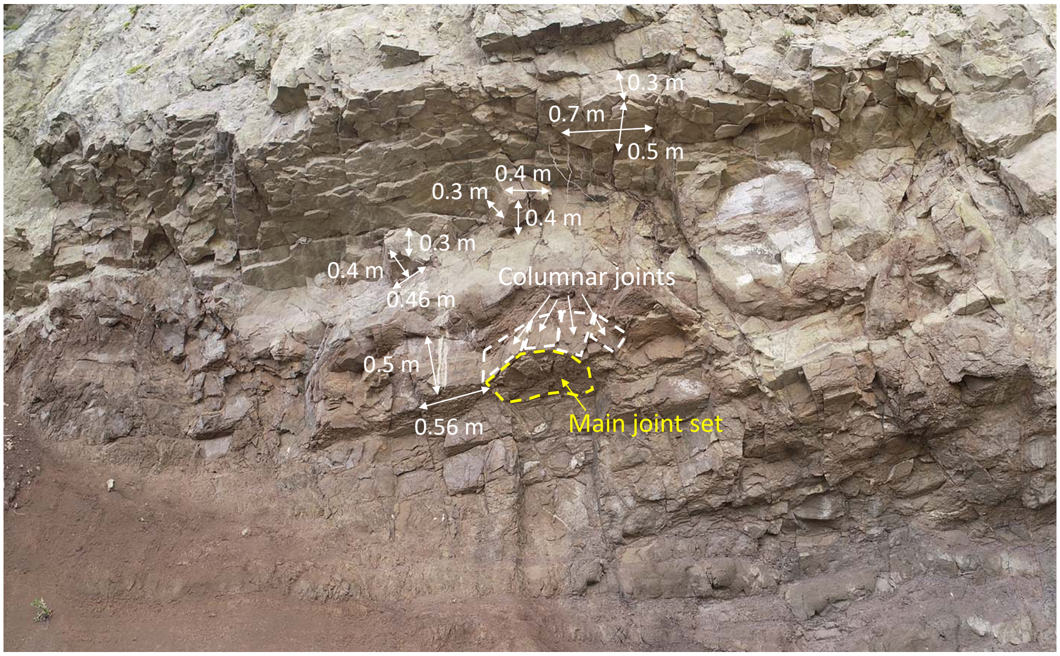

Figure 7.7 Joint sets on rock mass and measurements of rock block dimensions

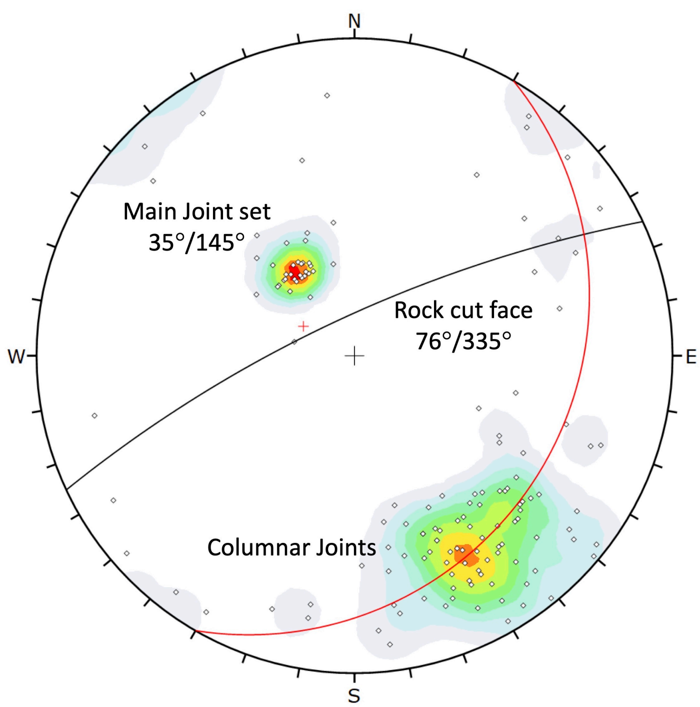

Figure 7.8 Stereonet of the discontinuities on the rock slope

The rock cut face was excavated at an orientation of 76°/335°, which dips in an opposite direction to the main joint set (Figure 7.8). Because of the development of the notch, the main joint set forms the bottom of the overhanging rock. The columnar joints that have an orientation close to 67°/327° are the potential sliding plane for small block failures in the rock cut. The main joint set and columnar joints form the potentially unstable rock blocks. Figure 7.7 shows a few block size measurements. The length of the rock blocks ranges between 0.3 and 0.7 m.

Three cross-sections with a strike of 337° are made through the most critical overhanging rock on the slope. These cross-sections are 4 m apart. Figure 7.9 shows the positions of these cross-sections on a plan view. Figure 7.10 shows a cropped version of the point cloud containing five million points corresponding to the locations of the cross-sections.

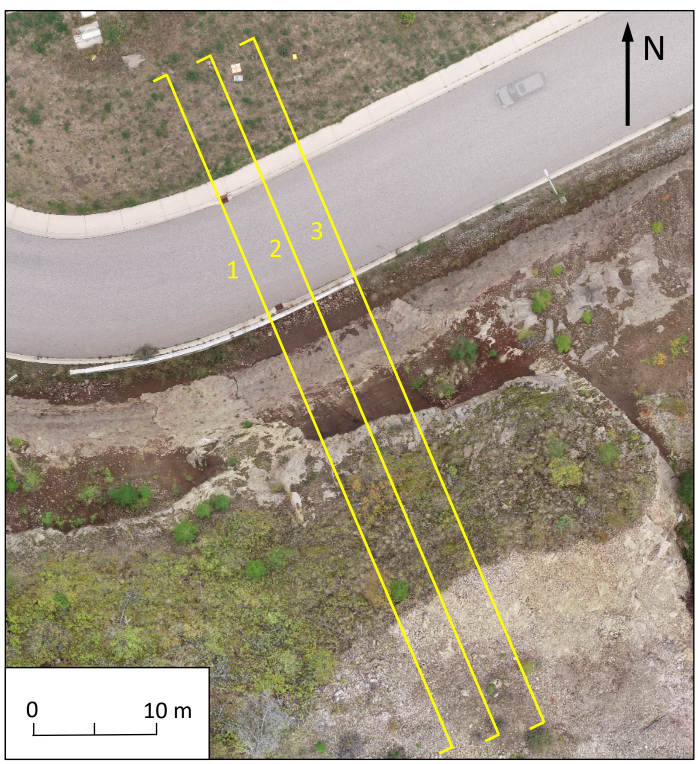

Figure 7.9 Plan view of rock slope showing the locations of three cross-sections

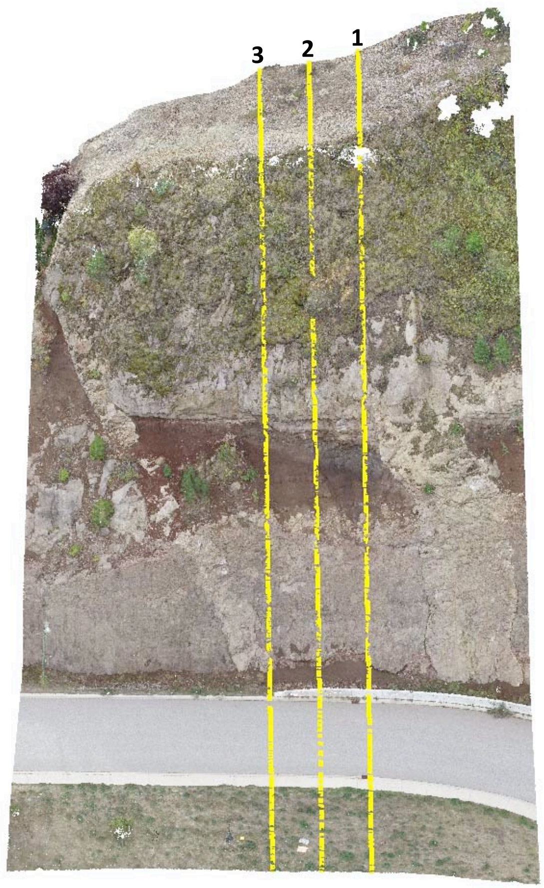

Figure 7.10 Point cloud of the rock slope with the locations of three cross-sections

The data from cross-section 2 in Figure 7.10 are plotted in Figure 7.11. The pyroclastic deposits are located between an upper and lower trachyandesite lava flow and intersected with the slope face at an elevation between 550 m to 554 m. The layer of pyroclastic rock has a dip angle of roughly 35°. The inserted figure shows the orientations of joints in the rock mass. The apparent dip of a joint on a cross-section can be calculated by

$$\alpha = \mathrm{atan}(\tan(\delta) \cdot \sin(\beta)) \tag{7.1}$$

where α is the apparent dip, δ is the true dip, and β is the angle between the strike of joint and the bearing of the cross-section.

From Eq. (7.1), the apparent dips of the columnar joints and the main joint set can be calculated as 67° and 35° for cross-section 2, respectively. The slope height is about 36 m from the road. The road was at about 538 m elevation. The locations of the ditch and concrete barrier are also shown. The angle of the slope face above the ditch is about 76°. The big notch in the middle of the rock slope is at an elevation between 550 m to 558 m. The angle of slope face above the notch is 56°, which was smaller than the slope angle below the notch. The top of the rock slope was excavated because of the construction of an apartment nearby.

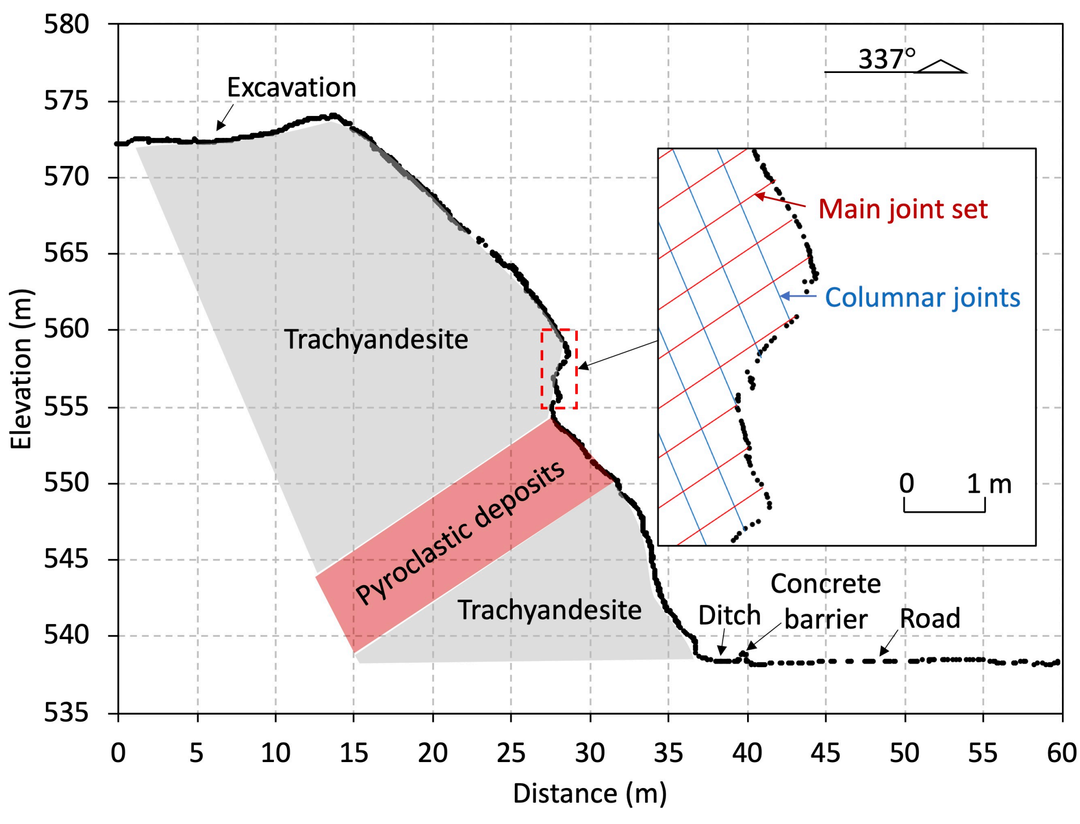

Figure 7.11 Rock types on cross-section 2 with insert figure showing joints

Figure 7.12 shows the slope geometries for all three cross-sections. The notch size gradually increases from cross-section 1 to cross-section 3. The rock slope profile to the east of cross-section 3 is similar to cross-section 3; thus cross-section 3 represents the rest of the slope profile.

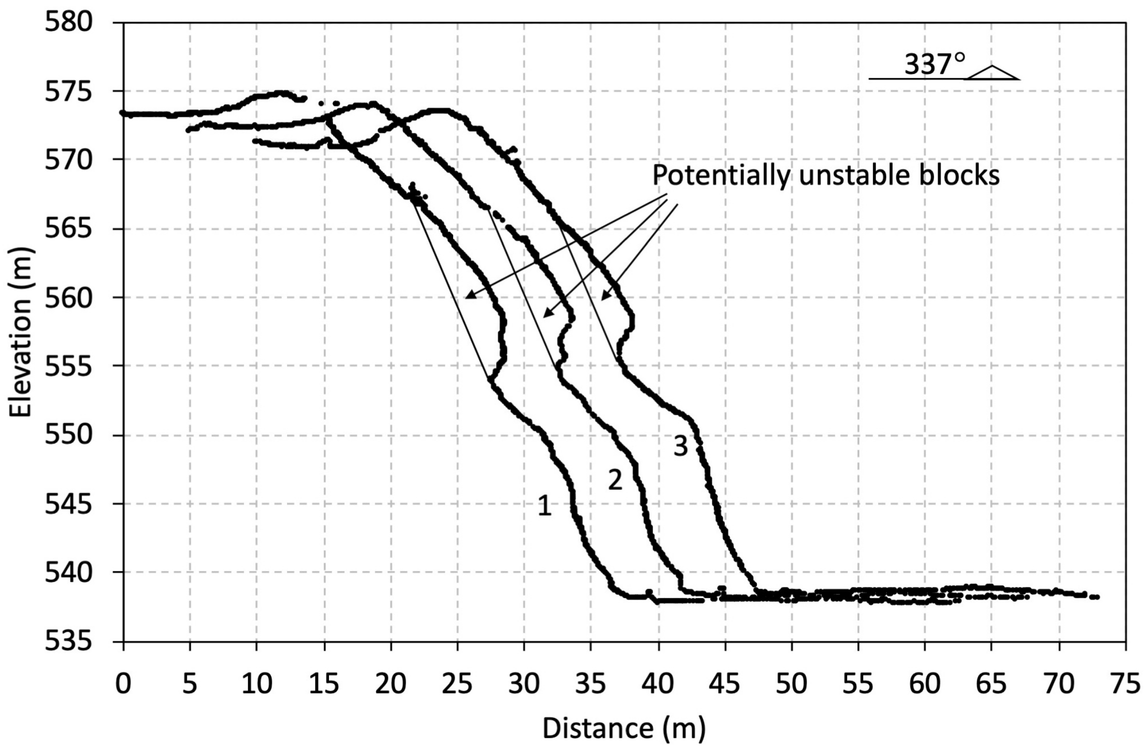

Figure 7.12 Slope geometries of three cross-sections with potentially unstable rock blocks

The geometries of larger-scale blocks that could slide along the steeply dipping columnar joints are shown in Figure 7.12. The volumes of these blocks were calculated. The rock block on cross-section 1 had the largest volume (22.9 m^3/m). The volumes of blocks at cross-section 2 and 3 were approximately 19.2 and 12.4 m^3/m, respectively.

7.4 Bolted steel mesh design for the rock cut

7.4.1 Back analysis of joint strength properties

The rock block at cross-section 1 is the most critical one, and it was used for the analysis because it has the largest volume. A back analysis of the columnar joint friction angle and cohesion is necessary because no laboratory experiments were conducted. Figure 7.13 shows a free-body diagram for the rock block. The stability analysis of the rock block is based on the Mohr-Coulomb failure criterion. The factor of safety can be expressed as

$$F_s = \frac{R_t}{W \cdot \sin\varphi} \tag{7.2}$$

$$W = \gamma_{\text{rock}} \cdot V \tag{7.3}$$

$$R_t = R_n \cdot \tan\phi + c \cdot A \tag{7.4}$$

$$R_n = W \cdot \cos\varphi - U \tag{7.5}$$

where W is the rock block weight, γ_{rock} is the rock density, V is the rock volume, R_n is the normal resistant force, R_t is the shear resistant force, φ is the dip of the critical joint, ϕ is the friction angle of the critical joint, c is the cohesion on the critical joint, A is the area of the sliding face, U is the water force at the bottom, F_s is the factor of safety.

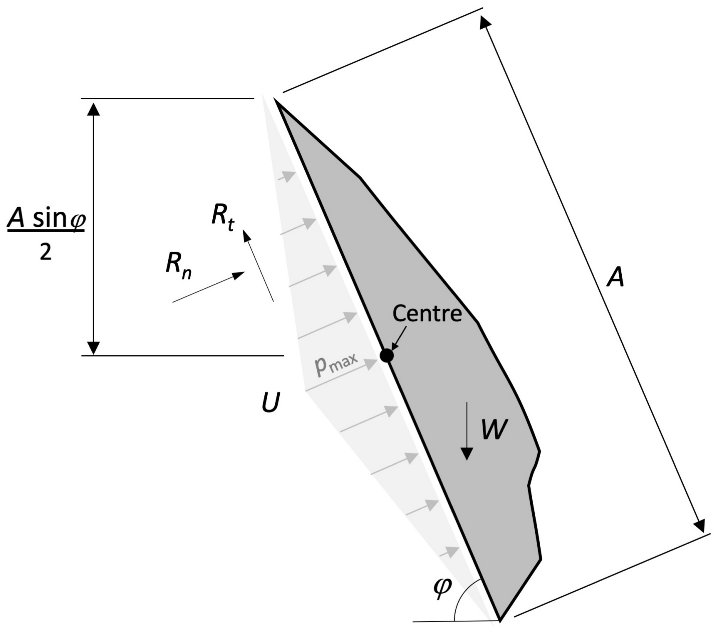

Figure 7.13 Free-body diagram for block at cross-section 1

Assuming the water fills the full fissure, as shown in Figure 7.13, the water can drain at both the top and bottom of the block. The peak water pressure is taken at the centre of the sliding surface. The water force can be calculated as

$$U = p_{\max} \cdot \frac{A}{2} = \gamma_w \cdot \frac{A}{2} \cdot \sin\varphi \cdot \frac{A}{2} \tag{7.6}$$

where $p_{\max}$ is the maximum water pressure, and γ_w is the unit weight of water (9.81 kN/m^3).

From Eq (7.2) to (7.6), F_s can be obtained by

$$F_s = \frac{(\gamma_{\text{rock}} \cdot V \cdot \cos\varphi - \gamma_w \cdot \frac{A^2}{4} \cdot \sin\varphi) \cdot \tan\phi + c \cdot A}{\gamma_{\text{rock}} \cdot V \cdot \sin\varphi} \tag{7.7}$$

Table 7.1 shows the rock block properties for the stability analysis Table 7.1. The unit weight of the rock is assumed 25.5 kN/m^3 (density 2600 kg/m^3). The critical joint dip is 67°. The area of the sliding face is measured as 13.8 m^2 per metre.

Table 7.1 Rock block properties for stability analysis

Property	Value
Unit weight of rock γ_{rock} (kN/m^3)	25.5
Rock volume V (m^3/m)	22.9
Area of sliding face A (m^2/m)	13.8
Critical joint dip φ (°)	67

The Barton shear strength criterion (Barton 1973) was used to estimate the friction angle in the joint. The shear strength τ in a joint can be determined by

$$\tau = \sigma' \tan(\phi_b + JRC \log\frac{JCS}{\sigma'}) \tag{7.8}$$

where ϕ_b is the base friction angle of a joint, JRC is the joint roughness coefficient, JCS is the compressive strength of the rock on the joint surface, σ' is the normal effective stress applied on this joint surface.

In Eq (7.8), the term $\phi_b + JRC \log\frac{JCS}{\sigma'}$ can be considered equivalent to the friction angle ϕ in the joint. According to Barton and Choubey (1977), the base friction angle ϕ_b for most smooth unweathered rock surfaces lies between 25° and 35°. Thus, the lower bound ϕ_b = 25° is chosen to be conservative. Based on the field investigation and comparison with Barton's standard curves for *JRC* (Hudson & Harrison 1997), the value of *JRC* is determined as 7. The *JCS* is assumed as 50 MPa, which is half of the rock's uniaxial compressive strength. The σ' is estimated from the normal stress acting on the centre of the sliding face, which is $\sigma' = 25.5 \times 22.9 \times \cos 67°/12.8/1000 = 0.018$ MPa. As shown in Figure 7.14, ϕ can be determined as 46° by drawing a line tangent to shear strength curve at point (0.018, 0.021).

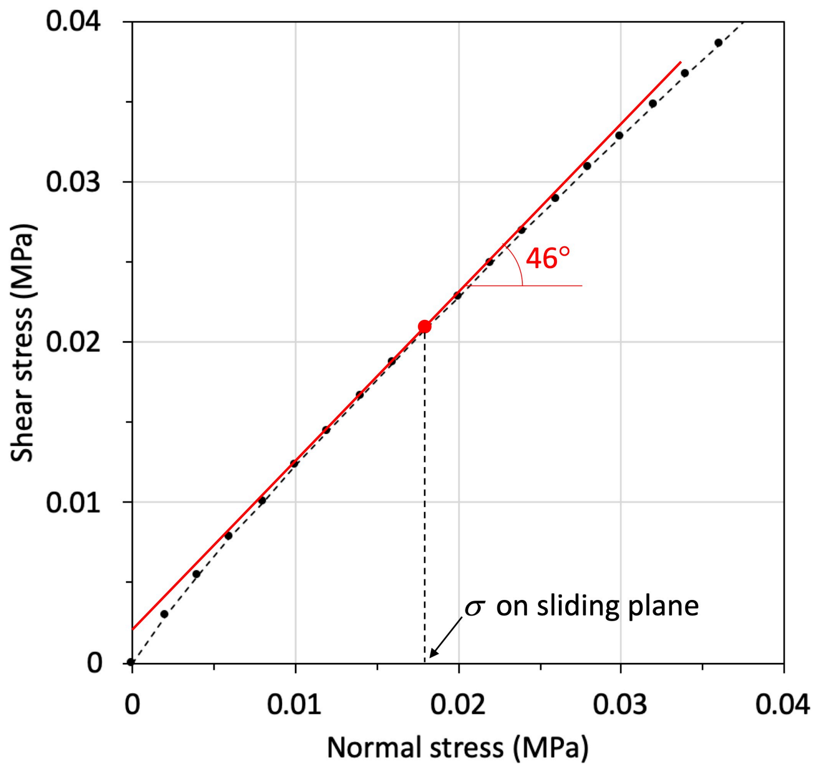

Figure 7.14 Estimation of ϕ based on Barton's shear strength criterion

The rock block is stable currently, thus its F_s must be greater than 1. There are likely rock bridges aside from the friction angle to holding the rock block. The effect of rock bridges can be taken as being equivalent to a cohesion c in the joint. Based on Eq (7.7), a value of c = 54 kPa can be found assuming F_s = 1 when ϕ = 46°. The equivalent sliding resistance from rock bridges can be calculated as $F = c \cdot A = 54 \times 13.8 = \sim745$ kN. The estimated shear strength of the intact rock is 50 MPa based on the rock's uniaxial compressive strength of 100 MPa. Thus, the area of rock bridges can be calculated as $A_{\text{rock bridges}} = 745/50/1000 = 0.015$ m^2. The minimum percentage of rock bridge in the joint is $A_{\text{rock bridges}}/A = 0.015/13.8 = \sim0.1\%$. Note that the chosen values for ϕ and c are on the conservative side.

7.4.2 General design of bolted steel mesh

Steel wire mesh pinned by rockbolts can secure the overhanging rock on the rock cut. The rockbolts can stabilize the large rock blocks, and steel wire mesh can hold the smaller rock blocks between the bolts. Figure 7.15 shows the design layout for the rock cut.

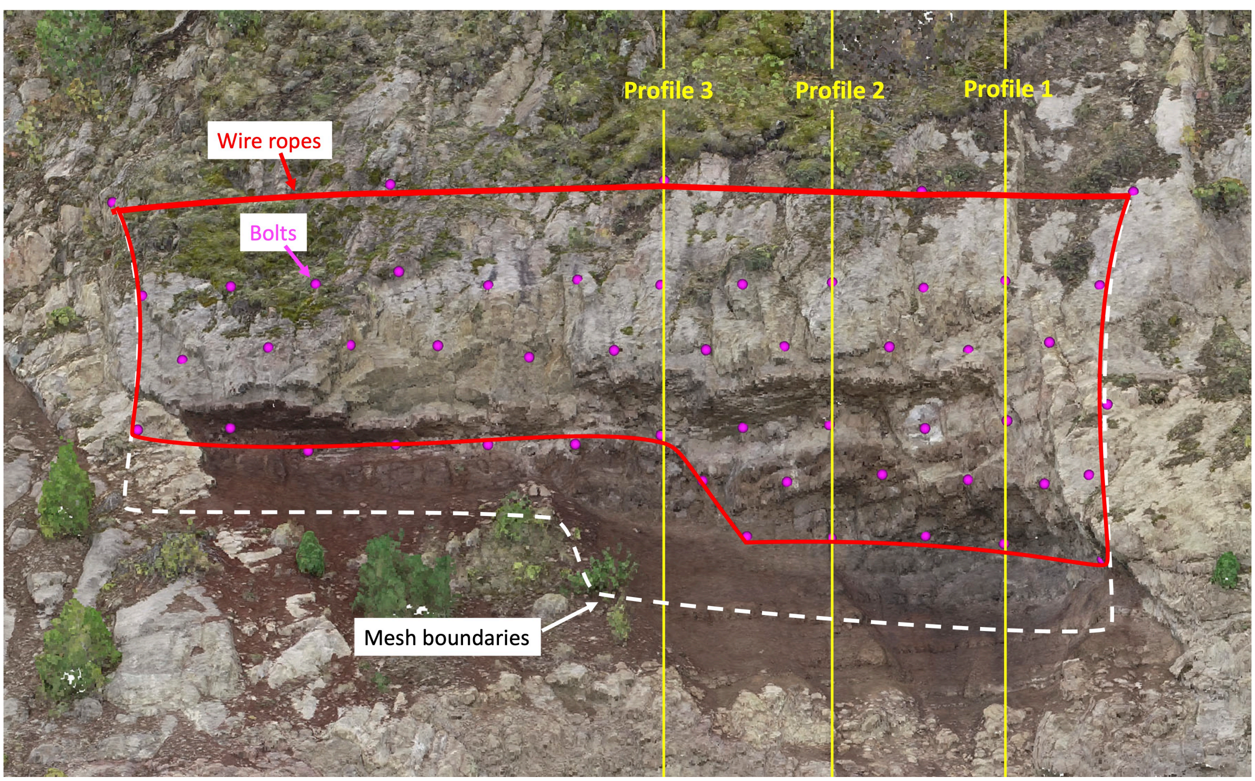

Figure 7.15 Design for rock slope stabilization

The design uses TECCO G65/3 high-tensile steel wire mesh. The measured mesh area is about 280 m^2. The results from Chapter 4 suggest that the mesh area between bolts in a pattern needs to be less than 7-8 m^2 to make the mesh more efficient. Chapter 6 suggests that bolt pattern B works better for preventing rocks from sliding between the bolts. For bolt pattern B, reducing the vertical spacing between bolts can make the steel wire mesh more efficient at providing a higher resistance force at lower displacement (Chapter 4). Thus, the design uses bolt pattern B with an average horizontal bolt spacing of 2 m, and a vertical bolt spacing from 1.5 to 2 m. The bolt spacing varies slightly depending on the slope geometry. The total number of bolts is 51. Figure 7.16 shows the three profiles with the bolts. The recommended bolt length is 6 m to ensure at least 3 m of bolt length goes beyond the potential sliding surface for the large-scale block. Five bolts with a 6 m length are designed to hang the wire mesh at the top. These top bolts are 6 m apart. All bolts plunge 15° with respect to the horizontal direction based on engineering experience.

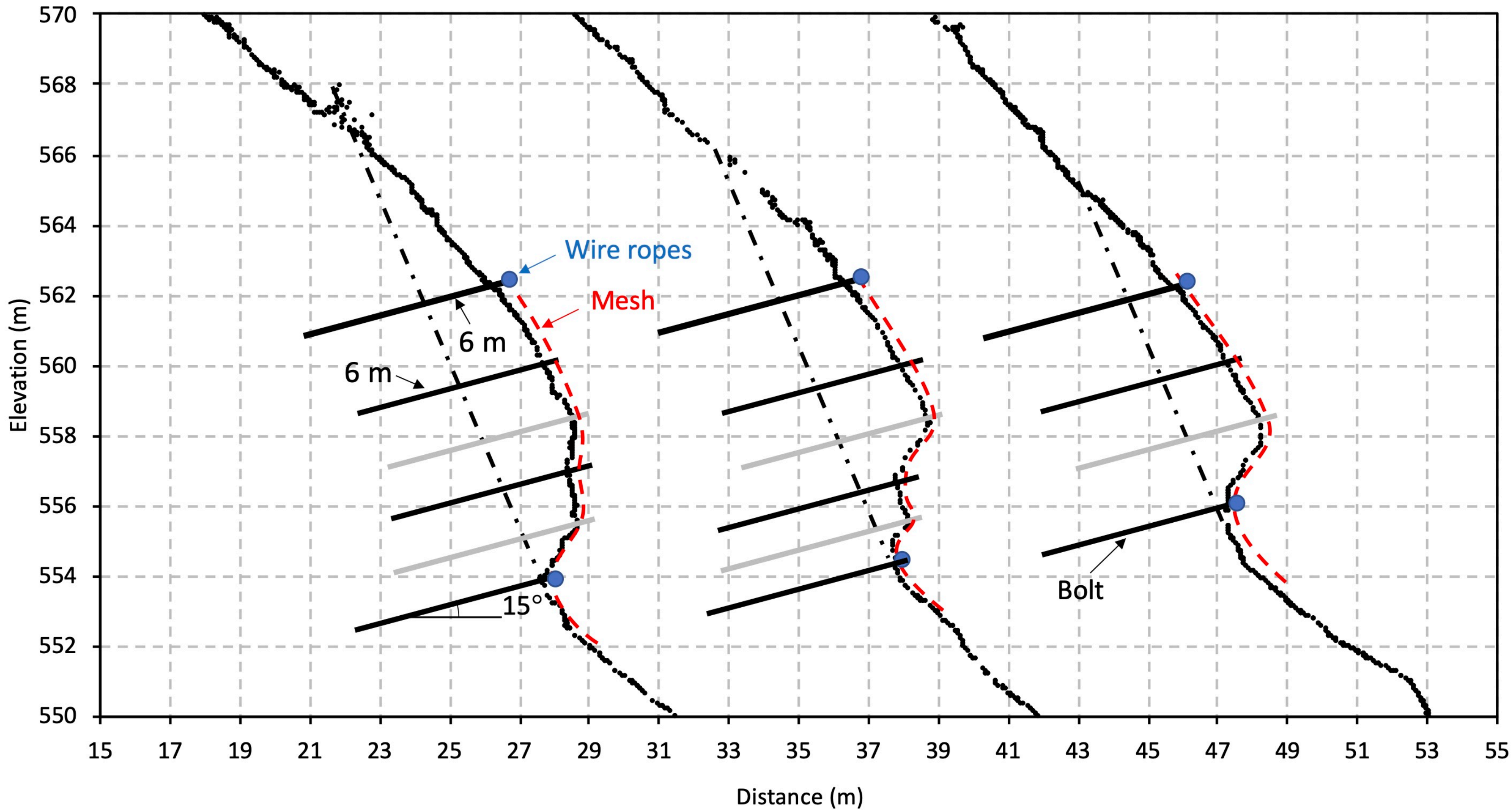

Figure 7.16 Bolted mesh design on cross-section 1, 2 and 3 (black bolts are on the current profile; grey bolts are on either side)

A wire rope goes through the eye nuts used on the top row of bolts. The top edge of the mesh is attached to this wire rope. There are two wire ropes to secure the mesh edges at each lateral side. Another one wire rope goes through the lowest row of bolts to make the mesh wrap the overhanging rock.

7.4.3 Estimation of mesh performance

The design applied the prediction model developed in Section 5.4 to estimate the mesh performance. The design criterion was that the mesh bulge needs to be less than 0.5 m without breaking wires.

The estimated average size of a single rock is $0.5 \times 0.5 \times 0.5 = 0.125$ m^3 based on the measurements in Section 7.3. The slope face angle of the overhanging rock is over 90°. Because the slope face angle is greater than the upper limit of the input values used in the prediction model, a slope face angle of 85° is used. The sliding angle for the rock block (67°) is also larger than the upper bound of the prediction model (50°). The friction angle is set to 25° because it is the base friction angle used in Barton's shear strength criterion, as well as the lower bound in the prediction model. Both horizontal and vertical bolt spacing is set to 2 m. The mesh response is checked for a rock position ranging from -0.5 to 0.5 m with respect to the centre in a bolt pattern.

The predicted mesh performance shown in Table 7.2 is found after applying the prediction model from Section 5.4. The predicted mesh bulge is less than 0.5 m without breaking the mesh wires for all cases where the rock volume is less than 0.625 m^3 (volume equivalent to 5 blocks). If the rock volume is 0.75 and 0.875 m^3 (volume equivalent to 6 - 7 blocks), a mixed mesh behaviour is predicted. The mesh bulge is less than 0.5 m if the rock is close to the lower bolt (-0.5 m rock position), while the mesh wires may rupture if the rock is at or above the centre in a bolt pattern. When the rock block is greater than 1 m^3 (volume equivalent to 8 blocks), the mesh wires may break for all situations. Based on the field investigation, approximately 2 m^3 of rock per year has fallen from the rock cut over the past seven years. This equates to an average volume of unstable rock in one pattern of bolts of less than 0.625 m^3. Thus, the design is acceptable.

Table 7.2 Predictions of mesh performance

Rock volume (m^3)	Rock position (m)	Mesh response
0.125	-0.5 to 0.5	< 0.5 m
0.25	-0.5 to 0.5	< 0.5 m
0.325	-0.5 to 0.5	< 0.5 m
0.5	-0.5 to 0.5	< 0.5 m
0.625	-0.5 to 0.5	< 0.5 m
	-0.5	< 0.5 m
0.75	0	Wire rupture
	0.5	Wire rupture
	-0.5	< 0.5 m
0.875	0	Wire rupture
	0.5	Wire rupture
1	-0.5 to 0.5	Wire rupture

7.4.4 Design of rockbolts

This section takes the rock block on cross-section 1 as an example to demonstrate the design of the rockbolts. The same approach is also used at cross-sections 2 and 3. Figure 7.17 shows a free-body diagram for calculating the net tensile force of rockbolts on cross-section 1. The design assumes that the water fills the fissure to be conservative. Eq. (7.6) shows the calculation of water force U at the block bottom. A force equilibrium analysis is used based on the concept of active bolts by Hoek and Bray (1981). Assuming all forces are through the centroid of the rock block. The factor of safety F_s is calculated as

$$F_s = \frac{(\gamma_{\text{rock}} \cdot V \cdot \cos\varphi - U + T \cdot \sin(\beta + \varphi)) \cdot \tan\phi + c \cdot A}{\gamma_{\text{rock}} \cdot V \cdot \sin\varphi - T \cdot \cos(\beta + \varphi)} \tag{7.9}$$

where β is the bolting angle with respect to the horizontal plane.

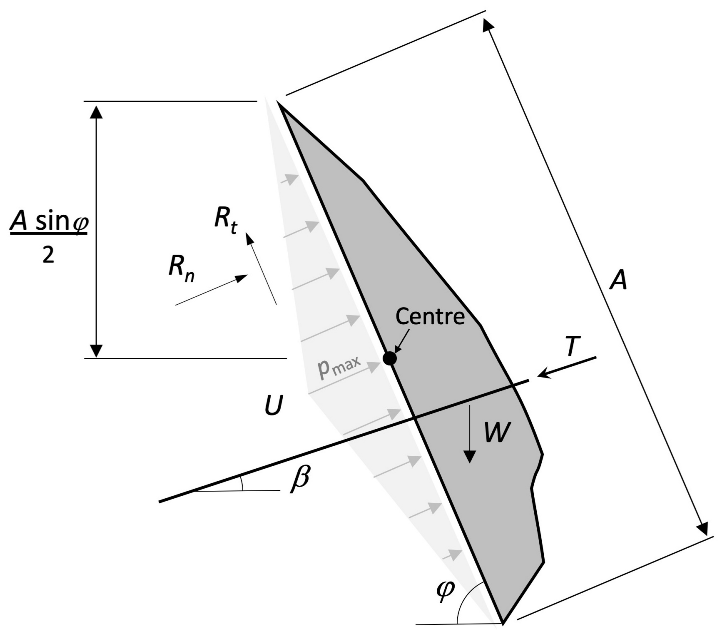

Figure 7.17 Free-body diagram for block on cross-section 1

From Eq. (7.9), the net tension force T of the bolts can be calculated by

$$T = \frac{\gamma_{\text{rock}} \cdot V \cdot (F_s \cdot \sin\varphi - \cos\varphi \cdot \tan\phi) - c \cdot A + U \cdot \tan\phi}{\sin(\beta + \varphi) \cdot \tan\phi + F_s \cdot \cos(\beta + \varphi)} \tag{7.10}$$

Thus, the tensile force on each bolt can be obtained by

$$T_{\text{bolt}} = \frac{T \cdot S_{\text{H}}}{n} \tag{7.11}$$

where S_H is the horizontal bolt spacing, n is the number of bolt rows per cross-section.

Table 7.3 shows the parameters for the rockbolt design. The dimensions of the rock block are based on Figure 7.12. The estimated parameters of joint shear strength in Section 7.4.1 are used. The cohesion c is reduced 54/2 = 27 kPa considering the effect of weathering. The bolting angle is set to 15° based on engineering experience. The horizontal bolt spacing is 2 m. Five rows of bolts are used at cross-section 1 besides the short bolts at the top, as shown in Figure 7.15. The same approach is also used to analyze the rock block at cross-sections 2 and 3.

Table 7.3 Parameters for the rockbolt design

Properties	Cross-section 1	Cross-section 2	Cross-section 3
Unit weight of rock γ_{rock} (kN/m^3)	25.5	25.5	25.5
Rock volume V (m^3/m)	22.9	19.2	12.4
Sliding face area A (m^2/m)	13.8	12.5	10
Critical joint dip φ (°)	67	67	67
Friction angle ϕ (°)	46	46	46
Cohesion c (kPa)	27	27	27
Bolt horizontal spacing S_H (m)	2	2	2
Bolting angle β (°)	15	15	15
Number of bolt rows n	5	5	3

If the rock blocks are at a limit equilibrium state (F_S = 1), from Eq. (7.10) to (7.11), the tensile forces on each bolt for cross-section 1, 2 and 3 are 129, 97, and 73 kN, respectively. If the F_S increases to 3, the tensile forces of each bolt on cross-section 1, 2 and 3 are 402, 328 and 328 kN, respectively. For these loads, the recommended rockbolts are #10 Grade 517 MPa Dywidag threadbar or equivalent (diameter 32 mm, yield load 424 kN), which gives a factor of safety of 3.

The measured mesh area is about 280 m^2. The mesh weighs 1.65 kg/m^2 (Geobrugg 2014). Thus, the total mesh weight is 1.65 × 280 × 9.81/1000 = ~5 kN. Considering a 0.2 m thick layer snow/ice accumulates on the mesh during winter. According to Muhunthan et al. (2005), the mesh weight plus snow load on the five rockbolts at the top can be expressed as

$$F_{\text{mesh+snow}} = (W_{\text{mesh}} + \rho_{\text{snow}} \cdot g \cdot A_{\text{mesh}} \cdot z) \cdot (\sin \alpha_f - \cos \alpha_f \cdot \tan \psi) \quad (7.12)$$

where W_{mesh} is the total mesh weight, ρ_{snow} is the density of the snowpack (919 kg/m^3), A_{mesh} is the mesh area, z is the thickness of the snowpack, α_f is the slope angle, ψ is the friction angle between mesh and slope face.

The dip angle of slope face α_f above the notch is 56°. Gratchev et al. (2015) suggest that the friction angle between the rock face and mesh is between 25 to 30°, thus ψ = 25° to be conservative. From Eq. (7.12), the calculated load of mesh plus snow is 290 kN. The load on each of the five rockbolts at the top to hang the mesh is 290/5 = ~58 kN. The recommended rockbolts are #14 Grade 517 MPa Dywidag threadbar or equivalent (43 mm diameter, yield load 801 kN). These bolts are strong enough to carry the load of mesh and also can contribute to stabilizing the rock cut.

7.4.5 Design of wire ropes

Figure 7.18 shows an equilibrium analysis for the wire rope at the top between two rockbolts. The load on the wire rope is the weight of wire mesh plus a 0.2 m thick snow/ice between two bolts 287/4 = ~72 kN. Assuming the load on the wire rope is a uniformly distributed load. The distance between the two bolts is L = 6 m. The sag of the wire rope is h. The maximum tensile force in the wire rope T_{max} occurs at the two ends (Hibbeler 2012). The T_{max} can be expressed as

$$T_{\max} = \frac{F_{\text{mesh+snow}}}{2}\sqrt{1 + (\frac{L}{4 \cdot h})^2} \tag{7.13}$$

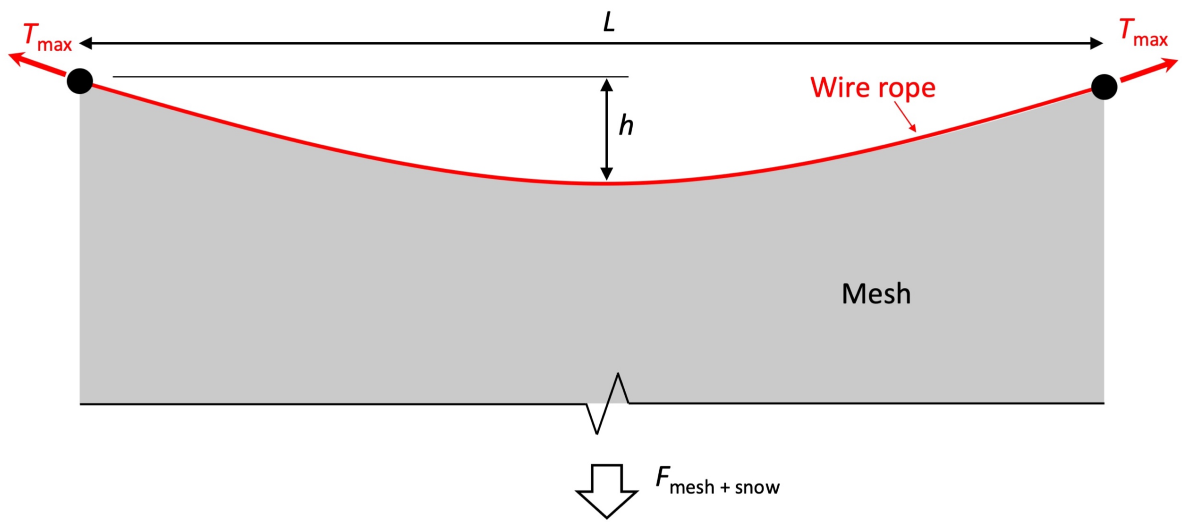

Figure 7.18 Equilibrium analysis on top wire rope between two bolts

Because the wire rope will be tensioned, h should be small. The calculated T_{max} using Eq. (7.13) when h is 0.2, 0.4, 0.6, 0.8, 1 m are shown in Table 7.4. The maximum tensile force in the wire rope is 274 kN when the h is 0.2 m. Note that this is an extreme case where only the wire rope carries all the load, and the sag is only 0.2 m over a span of 6 m. The five rockbolts at the top will also carry a portion of the load from mesh and snow.

The recommended wire rope is the 3/4 inch diameter EIPS IWRC 6 × 36 or equivalent (19 mm diameter, 288 kN breaking load). The wire rope is strong enough to hang the mesh. The other mesh edges will also use the same type of wire rope.

Table 7.4 T_{max} with various h

h (m)	0.2	0.4	0.6	0.8	1
T_{max} (kN)	274	141	98	77	65

7.5 Construction guideline

The recommended construction sequence for the bolts and mesh is outlined below.

(1) Scale the rock slope before the installation of the rockbolts and mesh. The loose rocks and vegetation on the slope surface must be removed.

(2) Mark the positions of all the bolts using dots of paint on the rock surface. The bolts should be placed at local concave surfaces within the tolerance range of the bolt pattern.

(3) Drill boreholes for the first row of threadbars. The recommended borehole diameter is 50 mm.

(4) Install #14 threadbars using a fast setting epoxy resin at the toe of the boreholes followed by cement grouting. Install eye nuts on the top row of shorter threadbars.

(5) Run a wire rope through the eye nuts. Tension and clamp the wire rope to the eye nuts at the two ends with wire rope clips. According to the manufacturer's manual (https://www.geobrugg.com/en/TECCO-System-101216.html), use at least four wire rope clips to clamp the wire rope at a spacing of 19 mm. The first wire rope clip must be placed immediately next to the eye. The required tightening torque must be at least 36 N·m.

(6) Cut the mesh rolls to the proper lengths.

(7) Unroll the mesh and fix the top edge of the mesh to the wire rope using TECCO press claws type 2 or steel shackles. The overlap between two mesh sheets must be greater than two diamond mesh units. The press claws or shackles must be used at every third mesh diamond.

(8) Connect the different mesh sheets together using TECCO connection clips T3. Each mesh diamond at the edge must be clipped to the neighbouring mesh with a single connection clip.

(9) Drill the holes for the remaining bolts through the mesh openings based on the marked points. A TECCO drilling device can be used to protect the mesh during the drilling.

(10) Install the bolts one row after another. The bolt heads above the rock face must stick out at least 0.3 m. The bolt heads below the overhanging rock must stick out at least 0.5 m.

(11) Install P33 spike plates to pin the mesh to the rock surface. Stretch the mesh if possible when installing the plates. Preload the bolts to approximately 150 kN by tightening the nuts on the bolts.

(12) Conduct pull-out tests on at least four bolts. The results of the proof tests should be submitted for quality assurance purposes.

(13) Install the eye nuts on the bolt heads at the two bottom corners.

(14) Install two wire ropes between the eye nuts to secure the two lateral and bottom mesh edges. Run the wire ropes through the eyes on the bolts and fasten the wire ropes by clamping them to the eye nuts with wire rope clips.

(15) Use type 2 press claws or shackles to attach the wire ropes to the mesh. These must be positioned every second mesh unit for the lateral edges, and every third mesh unit for the bottom edge.

Chapter 8: Conclusions and Discussions

8.1 Conclusions

The work presented in this dissertation includes extensive numerical simulations of steel mesh and steel mesh pinned by rockbolts. The results contribute a better understanding of the force and displacement behaviour of steel mesh with various bolt patterns and bolt spacing. The performance of bolted mesh loaded by a sliding or a toppling rock block is also studied. The knowledge gained from this research on the response of bolted steel mesh can help improve the design of bolted mesh for rock slopes.

The force-displacement behaviour of steel wire mesh was simulated using the DEM approach. An open-source DEM code, YADE, was used to perform the simulations. Two modelling approaches, a particle-based mesh model and a cylinder-based mesh model, were tested in terms of the predicted force-displacement response and computational cost. Results show that the particle-based modelling approach is not only less computationally intensive than the cylinder-based approach but it also provides an equivalent force-displacement response for steel mesh when the mesh interacts with other objects. Thus, the particle-based modelling approach was used for all subsequent modelling in this thesis. The bending resistance of wires is not considered in the particle-based mesh model. However, the use of the wire's tensile stress-strain curve and calibration of shift parameters allows the mesh model to capture the behaviour of the physical steel mesh. The mesh model in the tensile tests behaved more linearly than the real steel mesh in the experimental tests. The response of the mesh models had a good match with experimental punch tests when the loading is perpendicular to the mesh panel, which is consistent with the common loading direction in the field.

Simulations of mesh punch tests were conducted with two boundary conditions. One boundary condition fixed the movement of mesh edges in all directions to simulate a rigid supporting frame. The other boundary condition simulated fixed particles representing the locations of rockbolt plates. Results show that punch tests conducted with a rigid supporting frame underestimate the deformation and overestimate the load capacity of the steel mesh. These testing conditions differ from field conditions. In the field, the steel mesh is usually anchored by bolts and plates installed with various patterns.

A proper bolt arrangement will significantly increase the mesh resistance force, which helps to restrain rock blocks. Different bolt patterns generate different load transfer mechanisms in the mesh resulting in different force-displacement responses of steel mesh. Two commonly used bolt patterns were tested using DEM punch tests. In pattern A, the bolts are aligned with each other in rows and columns. In pattern B, the bolts in alternating rows are offset one half of the separation distance between the bolts. For bolt pattern A, a vertical to horizontal bolt spacing ratio that matches the mesh opening aspect ratio (1.72 ratio) makes the mesh more effective at carrying loads and limiting deformations. However, a V/H ratio that matches the mesh opening aspect ratio for bolt pattern B does not help to optimize the mesh effectiveness. Reducing the vertical bolt spacing in pattern B is more important than the horizontal spacing in achieving the mobilization of a higher mesh resistance force. For both bolt patterns, the mobilized mesh resistance force decreases as the distance from the nearest bolt to the loaded area increases. If the mesh is loaded at the centre within a pattern of bolts, and the bolt spacing geometry is close to the mesh opening aspect ratio, the mesh performance for pattern A is better compared to pattern B.

Existing design methods for bolted steel mesh use the ultimate load capacity of steel wire mesh and ignore mesh displacements. However, a mesh may experience an unacceptable displacement when it reaches its ultimate load capacity. This research developed the design curves plotted in Figure 4.18 for TECCO G65/3 steel mesh. These design curves show the mobilized mesh resistance force at different bolt densities, mesh deformations, and bolt patterns. These curves can help engineers choose the bolt spacing and they provide a lower-bound estimate of the mesh resistance force at the desired deformation limit for a given bolt pattern. An ideal bolt arrangement will help the steel mesh mobilize load quickly at lower deformations. A mesh area less than 7 to 8 m^2 between the nearest bolts will provide a higher resistance force. A mesh area of 7 to 8 m^2 is equivalent to an average bolt spacing of 2.7 m. Thus, the bolt spacing should be less than 2.7 m to obtain a more effective mesh in practice.

A parametric DEM study was conducted on the response of bolted mesh to the load created by a moving rock. Results show that the TECCO G65/3 steel wire mesh typically experienced a bulge of 0.4 to 0.8 m if the rock volume is less than 3 m^3 for a bolt spacing of 2 to 3 m. The mesh bulge increased as the rock volume, sliding angle, slope angle and bolt spacing increased. The mesh bulge is smaller if the unstable rock is located closer to the bottom bolt. The rock volume and sliding angle have the largest influence on the rupture of mesh wires. Slope angle and rock position have a minor influence on wire rupture. The bolted steel mesh was unlikely to experience wire ruptures if the net load from the rock block was less than 8 kN, but wire ruptures were likely if the load was larger than 13 kN. For loads between 8 and 13 kN, wires may or may not rupture in the mesh depending on the other influence factors.

The DEM simulation results in Chapter 5 were used to create mesh performance prediction models by using a support vector machine (SVM) learning approach. The SVM models can predict the behaviour of bolted steel mesh loaded by a sliding rock block for a range of input conditions. Different mesh performance criteria, such as the mesh bulge, can be selected to define classes in an SVM model. Three classes of mesh performance were used: (1) mesh bulge < 0.5 m without breaking a wire, (2) mesh bulge > 0.5 m without breaking a wire, and (3) > 1 wire in the mesh ruptures. The predictive ability of the SVM models with a polynomial or a radial basis function kernel was good. The SVM models provide a tool to determine the displacement of bolted steel mesh. Engineers can use the existing methods to design the bolted steel mesh, then apply the SVM model to check whether the predicted mesh displacement is acceptable.

A series of DEM simulations were conducted to investigate the response and load transfer between bolted steel mesh and a sliding or a topping rock block. For a sliding rock, the results show that the steel mesh can provide a sufficient support force to retain the rock block on the slope face if the installation of the rockbolts properly stresses the mesh. It is noted that the rock block may slide between the bolts if the bolts are aligned vertically in columns. The force is mainly carried by the wires that run diagonally from one rockbolt location to another. The rockbolt above and below the rock block (longitudinal restraint) carries much more load than the rockbolts on either side of the rock block (transverse restraint). Also, the percentage of load carried by longitudinal restraint in the mesh increases as the sliding angle increases. The load on the rockbolts below the rock block is slightly larger than the load on the bolts above the rock block at steep sliding angles.

The use of rockbolts to secure the steel mesh on the slope face will improve the performance of the steel mesh in preventing the toppling of the rock blocks. A proper tension on the steel mesh can hold to rock block at its original position. Results show that even if the mesh is not stressed during rock bolt installation, the mesh still can prevent the toppling rock from falling from the slope face, but a large displacement may occur. Rockbolts installed at locally concave locations on the slope face generate higher preloads in the mesh and better control the rock block displacement. A top-to-bottom bolting sequence is recommended because this sequence generates a larger support force in the mesh.

A case study was presented on the design of bolted steel mesh to support an overhanging rock cut. The rockbolts were designed to support potential large-scale planar sliding and the steel wire mesh was designed to hold jointed rock blocks between the bolts. A mesh bulge less than 0.5 m was used as the design criterion. TECCO G65/3 steel wire mesh with a bolt pattern B was designed to support the rock using the results of Chapter 4 and Chapter 6. The horizontal bolt spacing was approximately 2 m, and the vertical bolt spacing was 1.5 to 2 m. The bolt spacing varied slightly depending on the rock face geometry. The SVM model from Chapter 5 estimated that the maximum mesh bulge before wire rupture was less than 0.5 m for the chosen bolt arrangement, which was acceptable for the design.

8.2 Limitations and recommendations

There are limitations to the work presented in this dissertation. This section summarizes four key limitations and provides recommendations for future improvements.

(1) The research was focussed on one type of widely used steel mesh: TECCO G65/3 high-tensile steel wire mesh. Although this research focused on one mesh type, the same research methodologies can be used on other types of wire mesh.

(2) This research used a particle-based mesh model. A limitation is that this modelling method lacks the ability to simulate the physical mesh wires and bending in the wires. However, the calibrated and validated mesh models are still able to capture the mechanical response of the physical wire mesh when interacting with rock blocks.

(3) This research presented a detailed analysis of the effectiveness of wire mesh with two commonly used bolt patterns. However, the bolt locations can vary significantly depending on the actual rock slope conditions. The analysis approach can be used for any bolt layout.

(4) The analysis of the response of bolted mesh to an unstable rock covered a wide range of influence factors. The prediction model was created based on these results and had a good prediction accuracy. However, it is difficult to consider every possible situation in the field. Some values of the input parameters may still fall outside the current range, such as the slope face angle.

Recommendations for further research are:

(1) Laboratory tests should consider the use of a punch device to load the steel mesh pinned by bolts with patterns A and B, or other bolt arrangements. Field tests should evaluate bolted steel mesh holding various sized rock blocks on a rock slope. Although experimental tests are

expensive, the results would be valuable for making comparisons with numerical tests to validate the predicted load-displacement behaviour and load transfer mechanisms in the bolted steel mesh.

(2) Future work is recommended to include more mesh types to expand the knowledge on the response of wire mesh, such as the spider mesh and double-twisted wire mesh. The analysis can also include the influence of various types and sizes of bolt plates, such as spike plates, flat plates, and dome plates. Both numerical simulations and experimental tests can be involved in the analysis.

(3) Future work is recommended to develop design software for bolted steel mesh that integrates machine learning based on a database of the bolted mesh response from current simulations, as well as the results from future simulations.

(4) Future work is recommended to create a database of existing bolted mesh projects including information of mesh type, bolt pattern and spacing, mesh performance, slope geometry and geological conditions, etc.

References

Albaba, A., Lambert, S., Kneib, F., Chareyre, B., and Nicot, F. 2017. DEM modeling of a flexible barrier impacted by a dry granular flow. Rock Mechanics and Rock Engineering, **50**(11): 3029–3048. doi:10.1007/s00603-017-1286-z.

Amini, M., Majdi, A., and Aydan, Ö. 2009. Stability analysis and the stabilisation of flexural toppling failure. Rock Mechanics and Rock Engineering, **42**(5): 751–782. doi:10.1007/s00603-008-0020-2.

Amini, M., Majdi, A., and Veshadi, M.A. 2012. Stability analysis of rock slopes against block-flexure toppling failure. Rock Mechanics and Rock Engineering, **45**(4): 519–532. doi:10.1007/s00603-012-0220-7.

Awad, M., and Khanna, R. 2015. Efficient Learning Machines: Theories, Concepts, and Applications for Engineers and System Designers. Apress, Berkeley, CA. doi:10.1007/978-1-4302-5990-9.

Baek, B.S. 2018. Behaviour of welded steel wire mesh as surface support. University of Toronto.

Barton, N. 1973. Review of a new shear-strength criterion for rock joints. Engineering Geology, **7**(4): 287–332. doi:10.1016/0013-7952(73)90013-6.

Barton, N., and Choubey, V. 1977. The shear strength of rock joints in theory and practice. Rock Mechanics, **10**(1–2): 1–54. doi:10.1007/BF01261801.

Bergstra, J., and Bengio, Y. 2012. Random search for hyper-parameter optimization. The Journal of Machine Learning Research, **13**(1): 281–305.

Bertolo, P., Oggeri, C., and Peila, D. 2009. Full-scale testing of draped nets for rock fall protection. Canadian Geotechnical Journal, **46**(3): 306–317. doi:10.1139/T08-126.

Bertrand, D., Nicot, F., Gotteland, P., and Lambert, S. 2008. Discrete element method (DEM) numerical modeling of double-twisted hexagonal mesh. Canadian Geotechnical Journal, **45**(8): 1104–1117. doi:10.1139/T08-036.

Bertrand, D., Trad, A., Limam, A., and Silvani, C. 2012. Full-scale dynamic analysis of an innovative rockfall fence under impact using the discrete element method: from the local scale to the structure scale. Rock Mechanics and Rock Engineering, **45**(5): 885–900. doi:10.1007/s00603-012-0222-5.

Blanco-Fernandez, E., Castro-Fresno, D., del Coz Diaz, J.J., Navarro-Manso, A., and Alonso-Martinez, M. 2016. Flexible membranes anchored to the ground for slope stabilisation: numerical modelling of soil slopes using SPH. Computers and Geotechnics, **78**: 1–10. doi:10.1016/j.compgeo.2016.04.014.

Blanco-Fernandez, E., Castro-Fresno, D., Diaz, J.J.D., and Diaz, J. 2013. Field measurements of anchored flexible systems for slope stabilisation: Evidence of passive behaviour. Engineering Geology, **153**: 95–104. doi:10.1016/j.enggeo.2012.11.015.

Blanco-Fernandez, E., Castro-Fresno, D., Díaz, J.J.D.C., and Lopez-Quijada, L. 2011. Flexible systems anchored to the ground for slope stabilisation: Critical review of existing design methods. Engineering Geology, **122**(3–4): 129–145. doi:10.1016/j.enggeo.2011.05.014.

von Boetticher, A., and Volkwein, A. 2019. Numerical modelling of chain-link steel wire nets with discrete elements. Canadian Geotechnical Journal, **56**(3): 398–419. doi:10.1139/cgj-2017-0540.

Bourrier, F., Kneib, F., Chareyre, B., and Fourcaud, T. 2013. Discrete modeling of granular soils reinforcement by plant roots. Ecological Engineering, **61**: 646–657. doi:10.1016/j.ecoleng.2013.05.002.

Bourrier, F., Lambert, S., and Baroth, J. 2015. A reliability-based approach for the design of rockfall protection fences. Rock Mechanics and Rock Engineering, **48**(1): 247–259. doi:10.1007/s00603-013-0540-2.

Brereton, R.G., and Lloyd, G.R. 2010. Support Vector Machines for classification and regression. Analyst, **135**(2): 230–267. doi:10.1039/b918972f.

Brideau, M.-A., Yan, M., and Stead, D. 2009. The role of tectonic damage and brittle rock fracture in the development of large rock slope failures. Geomorphology, **103**(1): 30–49.

doi:http://dx.doi.org/10.1016/j.geomorph.2008.04.010.

Buzzi, O., Leonarduzzi, E., Krummenacher, B., Volkwein, A., and Giacomini, A. 2015. Performance of high strength rock fall meshes: Effect of block size and mesh geometry. Rock Mechanics and Rock Engineering, **48**(3): 1221–1231. doi:10.1007/s00603-014-0640-7.

Buzzi, O., Spadari, M., Giacomini, A., Fityus, S., and Sloan, S.W. 2012. Experimental testing of rockfall barriers designed for the low range of impact energy. Rock Mechanics and Rock Engineering, **46**(4): 701–712. doi:10.1007/s00603-012-0295-1.

Cala, M., Flum, D., Rüegger, R., Roduner, A., and Wartmann, S. 2012. TECCO® slope stabilization system and RUVOLUM® dimensioning method. Geobrugg.

Cala, M., Roth, A., and Roduner, A. 2013a. Large scale field tests of rock bolts and high-tensile steel wire mesh subjected to dynamic loading. *In* Eurock 2013–Rock mechanics for resources, energy and environment. *Edited by* M. Kwaśniewski and D. Łydżba. International Society for Rock Mechanics and Rock Engineering, Wroclaw, Poland. pp. 721–726.

Cala, M., Stolz, M., Baraniak, P., Rist, A., and Roduner, A. 2013b. Large scale field tests for slope stabilizations made with flexible facings. *In* Eurock 2013–Rock mechanics for resources, energy and environment. *Edited by* M. Kwaśniewski and D. Łydżba. International Society for Rock Mechanics and Rock Engineering, Wroclaw, Poland. pp. 659–662.

Castro-Fresno, D. 2000. Estudio y análisis de las membranas flexibles como elemento de soporte para la estabilización de taludes y laderas de suelos y/o materiales sueltos. Universidad De Cantabria. Available under a Creative Commons Attribution 3.0 Spain licence. Available from https://repositorio.unican.es/xmlui/handle/10902/1114.

Castro-Fresno, D., del Coz Diaz, J.J., López, L.A., and García Nieto, P.J. 2008. Evaluation of the resistant capacity of cable nets using the finite element method and experimental validation. Engineering Geology, **100**(1–2): 1–10. doi:10.1016/j.enggeo.2008.02.007.

Castro-Fresno, D., López Q., L., Blanco Fernandez, E., and Zamora Barraza, D. 2009. Design and evaluation of two laboratory tests for the nets of a flexible anchored slope stabilization system. Geotechnical Testing Journal, **32**(4): 101218. doi:10.1520/GTJ101218.

Cavers, D.S. 1981. Simple methods to analyze buckling of rock slopes. Rock Mechanics, **14**(2): 87–104. doi:10.1007/BF01239857.

Cazzani, A., Mongiovì, L., and Frenez, T. 2002. Dynamic finite element analysis of interceptive devices for falling rocks. International Journal of Rock Mechanics and Mining Sciences, **39**(3): 303–321. doi:10.1016/S1365-1609(02)00037-0.

Cho, S.E. 2009. Probabilistic stability analyses of slopes using the ANN-based response surface. Computers and Geotechnics, **36**(5): 787–797. doi:10.1016/j.compgeo.2009.01.003.

Da Costa, A., and Sagaseta, C. 2010. Analysis of shallow instabilities in soil slopes reinforced with nailed steel wire meshes. Engineering Geology, **113**(1–4): 53–61. doi:10.1016/j.enggeo.2010.02.005.

Coulibaly, J.B., Chanut, M.-A., Lambert, S., and Nicot, F. 2019. Toward a generic computational approach for flexible rockfall barrier modeling. Rock Mechanics and Rock Engineering, **52**(11): 4475–4496. doi:10.1007/s00603-019-01878-6.

del Coz Díaz, J.J., Nieto, P.J.G., Fresno, D.C., and Fernández, E.B. 2009. Non-linear analysis of cable networks by FEM and experimental validation. International Journal of Computer Mathematics, **86**(2): 301–313. doi:10.1080/00207160801965339.

Cundall, P.A., and Strack, O.D.L. 1979. Discrete numerical-model for granular assemblies. Geotechnique, **29**(1): 47–65.

Effeindzourou, A., Chareyre, B., Thoeni, K., Giacomini, A., and Kneib, F. 2016. Modelling of deformable structures in the general framework of the discrete element method. Geotextiles and Geomembranes, **44**(2): 143–156. doi:10.1016/j.geotexmem.2015.07.015.

Effeindzourou, A., Thoeni, K., Giacomini, A., and Wendeler, C. 2017. Efficient discrete modelling of composite structures for rockfall protection. Computers and Geotechnics, **87**: 99–114. doi:10.1016/j.compgeo.2017.02.005.

Eliáš, J. 2014. Simulation of railway ballast using crushable polyhedral particles. Powder Technology, **264**: 458–465. doi:10.1016/j.powtec.2014.05.052.

Escallon, J.P., Boetticher, V., Wendeler, C., Chatzi, E., and Bartelt, P. 2015. Mechanics of chain-link wire nets with loose connections. Engineering Structures, **101**: 68–87. doi:10.1016/j.engstruct.2015.07.005.

Escallon, J.P., Wendeler, C., and Mrozik, M. 2013. Numerical simulation of the impact of a rock fall impact on a flexible barrier using Abaqus/Explicit 6.12. *In* Eurock 2013–Rock mechanics for resources, energy and environment. *Edited by* M. Kwaśniewski and D. Łydżba. International Society for Rock Mechanics and Rock Engineering, Wroclaw, Poland. pp. 417–423.

Fang, K., Li, R., and Sudjianto, A. 2006. Design and modeling for computer experiments. Chapman and Hall/CRC, New York.

Flum, D., and Roduner, A. 2010. Findings from large-scale field tests of spiral rope nets for rock protection. *In* Eurock 2010-Rock Mechanics in Civil and Environmental Engineering. *Edited by* Zhao, Labiouse, Dudt, and Mathier. International Society for Rock Mechanics and Rock Engineering, Lausanne, Switzerland. pp. 625–628.

Flum, D., Wartmann, S., Rüegger, R., and Rorem, E. 2008. New generation of spiral rope nets for rock protection - tests, design, application. *In* 59th Highway Geology Symposium. Santa Fe, New Mexico. p. 23.

Frayssines, M., and Hantz, D. 2006. Failure mechanisms and triggering factors in calcareous cliffs of the Subalpine Ranges (French Alps). Engineering Geology, **86**(4): 256–270. doi:10.1016/j.enggeo.2006.05.009.

Gao, Z., Al-Budairi, H., and Steel, A. 2018. Experimental testing of low-energy rockfall catch fence meshes. Journal of Rock Mechanics and Geotechnical Engineering, **10**(4): 798–804. doi:10.1016/j.jrmge.2018.01.004.

Gentilini, C., Gottardi, G., Govoni, L., Mentani, A., and Ubertini, F. 2013. Design of falling rock protection barriers using numerical models. Engineering Structures, **50**: 96–106. doi:10.1016/j.engstruct.2012.07.008.

Gentilini, C., Govoni, L., de Miranda, S., Gottardi, G., and Ubertini, F. 2012. Three-dimensional numerical modelling of falling rock protection barriers. Computers and Geotechnics, **44**: 58–72. doi:10.1016/j.compgeo.2012.03.011.

Geobrugg. 2014. High-tensile steel wire mesh TECCO G65/3. Technical Data Sheet.

Geobrugg AG. 2017. Software manual: SPIDER Single block protection. Available from https://www.geobrugg.com/datei.php?src=download/L2_SPIDER-S3_130-ONLINE-TOOL-Manual-E_170428.pdf.

Giacomini, A., Thoeni, K., Lambert, C., Booth, S., and Sloan, S.W. 2012. Experimental study on rockfall drapery systems for open pit highwalls. International Journal of Rock Mechanics and Mining Sciences, **56**: 171–181. doi:10.1016/j.ijrmms.2012.07.030.

Gobbin, L., Giacchetti, G., Grimod, A., and Brunet, G. 2017. Results of tests to evaluate the tensile strength and the load bearing capacity of rockfall nets according to new ISO standards. *In* 68th Highway Geology Symposium. Marietta, Georgia. p. 12.

Goodman, R.E., and Kieffer, D.S. 2002. Behavior of rock in slopes. Journal of Geotechnical and Geoenvironmental Engineering, **126**(8): 675–684. doi:10.1061/(asce)1090-0241(2000)126:8(675).

Gottardi, G., and Govoni, L. 2010. Full-scale modelling of falling rock protection barriers. Rock Mechanics and Rock Engineering, **43**(3): 261–274. doi:10.1007/s00603-009-0046-0.

Gratchev, I., Kim, D.H., and Chung, M. 2015. Study of the interface friction between mesh and rock surface in drapery systems for rock fall hazard control. Engineering Geology, **199**: 12–18. doi:10.1016/j.enggeo.2015.10.005.

Grimod, A., and Giacchetti, G. 2014. Design approach for secured drapery systems. *In* Landslide Science for a Safer Geoenvironment. *Edited by* K. Sassa, P. Canuti, and Y. Yin. , Cham. pp. 99–105.

Hibbeler, R.C. 2012. Structural analysis. *In* 8th edition. Prentice Hall, Boston.

Hoek, E., and Bray, J.D. 1981. Rock slope engineering. *In* 3rd edition. Taylor and Francis, London and New York.

Huang, R.Q., Wu, L.Z., He, Q., and Li, J.H. 2017. Stress intensity factor analysis and the stability of overhanging rock. Rock Mechanics and Rock Engineering, **50**(8): 2135–2142. doi:10.1007/s00603-017-1209-z.

IberoTalud, and Universidad de Cantabria. 2005. DRET®. Programa de dimensionamiento de redes para estabilización de taludes. Manual de ayuda. Universidad de Cantabria.

International Organization for Standardization. 2016a. Steel wire rope net panels and rolls - Definitions and specifications. ISO 17746:2016. Available from https://www.iso.org/obp/ui/#iso:std:iso:17746:ed-1:v1:en.

International Organization for Standardization. 2016b. Steel wire ring net panels - Definitions and specifications. ISO 17745:2016. Available from https://www.iso.org/obp/ui/#iso:std:iso:17745:ed-1:v1:en.

International Society for Rock Mechanics and Rock Engineering. 1981. Rock characterization, testing and monitoring - ISRM suggested methods. Oxford: Pergamon.

Jiang, Q., Liu, X., Wei, W., and Zhou, C. 2013. A new method for analyzing the stability of rock wedges. International Journal of Rock Mechanics and Mining Sciences, **60**: 413–422. doi:10.1016/j.ijrmms.2013.01.008.

Justo, J.L., Castro, D., Azañón, J.M., Saura, J., Durand, P., Romero, E., Vázquez-Carretero, N., Morales-Esteban, A., Vázquez-Boza, M., and Justo, E. 2014. Environmental and mechanical aspects of an anchored mesh for stabilisation of a cliff at La Alhambra. Bulletin of Engineering Geology and the Environment, **73**(2): 667–685. doi:10.1007/s10064-013-0507-2.

Kogure, T., and Matsukura, Y. 2010. Critical notch depths for failure of coastal limestone cliffs: case study at Kuro-shima Island, Okinawa, Japan. Earth Surface Processes and Landforms, **35**(9): 1044–1056. doi:10.1002/esp.1940.

Li, X., and Zhao, J. 2018. A unified CFD-DEM approach for modeling of debris flow impacts on flexible barriers. International Journal for Numerical and Analytical Methods in Geomechanics, **42**(14): 1643–1670. doi:10.1002/nag.2806.

Liu, C.H., Jaksa, M.B., and Meyers, A.G. 2010. Toppling mechanisms of rock slopes considering stabilization from the underlying rock mass. International Journal of Rock Mechanics and Mining Sciences, **47**(2): 348–354. doi:10.1016/j.ijrmms.2009.11.008.

Liu, K., Liu, B., and Fang, Y. 2019. An intelligent model based on statistical learning theory for engineering rock mass classification. Bulletin of Engineering Geology and the Environment, **78**(6): 4533–4548. Bulletin of Engineering Geology and the Environment. doi:10.1007/s10064-018-1419-y.

Lu, P., and Rosenbaum, M.S. 2003. Artificial neural networks and grey systems for the prediction of slope stability. Natural Hazards, **30**(3): 383–398. doi:10.1023/B:NHAZ.0000007168.00673.27.

Maccaferri. 2019. MACRO1 Theory and Background.

Majdi, A., and Amini, M. 2011. Analysis of geo-structural defects in flexural toppling failure. International Journal of Rock Mechanics and Mining Sciences, **48**(2): 175–186. doi:10.1016/j.ijrmms.2010.11.007.

Makedon, T., and Chatzigogos, N. 2012. Failure mechanism of overhanging slopes in sedimentary rocks with dissimilar mechanical properties. Bulletin of Engineering Geology and the Environment, **71**(4): 703–708. doi:10.1007/s10064-012-0441-8.

Matsukura, Y. 2001. Rockfall at Toyohama Tunnel, Japan, in 1996: effect of notch growth on instability of a coastal cliff. Bulletin of Engineering Geology and the Environment, **60**(4): 285–289. doi:10.1007/s100640100123.

Mentani, A., Govoni, L., Giacomini, A., Gottardi, G., and Buzzi, O. 2018. An equivalent continuum approach to efficiently model the response of steel wire meshes to rockfall impacts. Rock Mechanics and Rock Engineering, **51**(9): 2825–2838. doi:10.1007/s00603-018-1490-5.

Mentani, A., Govoni, L., Gottardi, G., Lambert, S., Bourrier, F., and Toe, D. 2016. A new approach to evaluate the effectiveness of rockfall barriers. Procedia Engineering, **158**: 398–403. doi:10.1016/j.proeng.2016.08.462.

de Miranda, S., Gentilini, C., Gottardi, G., Govoni, L., Mentani, A., and Ubertini, F. 2015. Virtual testing of existing semi-rigid rockfall protection barriers. Engineering Structures, **85**: 83–94. doi:10.1016/j.engstruct.2014.12.022.

Mollon, G., Dias, D., and Soubra, A.-H. 2011. Probabilistic analysis of pressurized tunnels against face stability using collocation-based stochastic response surface method. Journal of Geotechnical and Geoenvironmental Engineering, **137**(4): 385–397. doi:10.1061/(ASCE)GT.1943-5606.0000443.

Montgomery, D.C. 2017. Design and analysis of experiments. John Wiley & Sons.

Muhunthan, B., Shu, S., Sasiharan, N., Hattamleh, O.A., Badger, T.C., Lowell, S.M., and Duffy, J.D. 2005. Analysis and design of wire mesh/cable net slope protection. Washington State Transportation Center (TRAC), Seattle, Washington.

Muller, B.J., Dahlhaus, P.G., and Miner, A.S. 2006. Coastal rockfall hazard identification, Barwon Heads, Victoria. Australian Geomechanics, **41**(3): 85–92.

Nicot, F., Gotteland, P., Bertrand, D., and Lambert, S. 2007. Multiscale approach to geo-composite cellular structures subjected to rock impacts. International Journal for Numerical and Analytical Methods in Geomechanics, **31**(13): 1477–1515. John Wiley & Sons, Ltd. doi:10.1002/nag.604.

Paronuzzi, P., Bolla, A., and Rigo, E. 2016. 3D stress–strain analysis of a failed limestone wedge influenced by an intact rock bridge. Rock Mechanics and Rock Engineering, **49**(8): 3223–3242. doi:10.1007/s00603-016-0963-7.

Paronuzzi, P., and Serafini, W. 2009. Stress state analysis of a collapsed overhanging rock slab: A case study. Engineering Geology, **108**(1–2): 65–75. doi:10.1016/j.enggeo.2009.06.019.

Pedregosa, F., Varoquaux, G., Gramfort, A., Michel, V., Thirion, B., Grisel, O., Blondel, M., Prettenhofer, P., Weiss, R., Dubourg, V., Vanderplas, J., Passos, A., Cournapeau, D., Brucher, M., Perrot, M., and Duchesnay, E. 2011. Scikit-learn: machine learning in Python. Journal of Machine Learning Research, **12**: 2825–2830.

Qi, X., Pei, X., Han, R., Yang, Y., Meng, Q., and Yu, Z. 2018. Analysis of the effects of a rotating rock on rockfall protection barriers. Geotechnical and Geological Engineering, **36**(5): 3255–3267. doi:10.1007/s10706-018-0535-6.

Qin, S., Wang, S., and Jiao, J.J. 2001. A cusp catastrophe model of instability of slip-buckling slope. Rock Mechanics and Rock Engineering, **34**(2): 119–134. doi:10.1007/s006030170018.

Roth, A., and Ranta-Korpi, R. 2007. Numerical modeling and dynamic simulation of high-tensile steel wire mesh for ground support under rockburst loading. *In* Proceedings of the 1st Canada-US Rock Mechanics Symposium. American Rock Mechanics Association, Vancouver, Canada. pp. 1505–1509. doi:10.1201/NOE0415444019-c187.

Sasiharan, N., Muhunthan, B., Badger, T.C., Shu, S., and Carradine, D.M. 2006. Numerical analysis of the performance of wire mesh and cable net rockfall protection systems. Engineering Geology, **88**(1–2): 121–132. doi:10.1016/j.enggeo.2006.09.005.

Scholtès, L., and Donzé, F. V. 2015. A DEM analysis of step-path failure in jointed rock slopes. Comptes Rendus Mécanique, **343**(2): 155–165. doi:http://dx.doi.org/10.1016/j.crme.2014.11.002.

Shamekhi, E., and Tannant, D.D. 2015. Probabilistic assessment of rock slope stability using response surfaces determined from finite element models of geometric realizations. Computers and Geotechnics, **69**: 70–81. doi:10.1016/j.compgeo.2015.04.014.

Shu, S., Muhunthan, B., and Badger, T.C. 2005a. Snow loads on wire mesh and cable net rockfall slope protection systems. Engineering Geology, **81**(1): 15–31. doi:10.1016/j.enggeo.2005.06.007.

Shu, S., Muhunthan, B., Badger, T.C., and Grandorff, R. 2005b. Load testing of anchors for wire mesh and cable net rockfall slope protection systems. Engineering Geology, **79**(3–4): 162–176. doi:10.1016/j.enggeo.2005.01.008.

Šmilauer, V., Catalano, E., Chareyre, B., Dorofeenko, S., Duriez, J., Gladky, A., Kozicki, J., Modenese, C., Scholtès, L., Sibille, L., Stránský, J., and Thoeni, K. 2015. Yade Documentation 2nd ed. The Yade Project. doi:10.5281/zenodo.34073.

Spadari, M., Giacomini, A., Buzzi, O., and Hambleton, J.P. 2012. Prediction of the bullet effect for rockfall barriers: a scaling approach. Rock Mechanics and Rock Engineering, **45**(2): 131–144. doi:10.1007/s00603-011-0203-0.

Tannant, D.D., Giordan, D., and Morgenroth, J. 2017. Characterization and analysis of a translational rockslide on a stepped-planar slip surface. Engineering Geology, **220**: 144–151. doi:10.1016/j.enggeo.2017.02.004.

Tempelman-Kluit, D.J. 1989. Geology, Pentiction, British Columbia; Geological Survey of Canada, Map 1736A, scale 1:250,000.

Thiele, S.T., Grose, L., Samsu, A., Micklethwaite, S., Vollgger, S.A., and Cruden, A.R. 2017. Rapid, semi-automatic fracture and contact mapping for point clouds, images and geophysical data. Solid Earth, **8**(6): 1241–1253. doi:10.5194/se-8-1241-2017.

Thoeni, K., Giacomini, A., Lambert, C., and Sloan, S.W. 2015. Rockfall trajectory analysis with drapery systems. *In* Engineering Geology for Society and Territory - Volume 2. *Edited by* G. Lollino, D. Giordan, G.B. Crosta, J. Corominas, R. Azzam, J. Wasowski, and N. Sciarra. International Publishing, Cham. pp. 2007–2011. doi:10.1007/978-3-319-09057-3_356.

Thoeni, K., Giacomini, A., Lambert, C., Sloan, S.W., and Carter, J.P. 2014. A 3D discrete element modelling approach for rockfall analysis with drapery systems. International Journal of Rock Mechanics and Mining Sciences, **68**: 107–119. doi:10.1016/j.ijrmms.2014.02.008.

Thoeni, K., Lambert, C., Giacomini, A., and Sloan, S.W. 2013. Discrete modelling of hexagonal wire meshes with a stochastically distorted contact model. Computers and Geotechnics, **49**: 158–169. doi:10.1016/j.compgeo.2012.10.014.

Toe, D., Mentani, A., Govoni, L., Bourrier, F., Gottardi, G., and Lambert, S. 2018. Introducing meta-models for a more efficient hazard mitigation strategy with rockfall protection barriers. Rock Mechanics and Rock Engineering, **51**(4): 1097–1109. doi:10.1007/s00603-017-1394-

9.

Tran, P. Van, Maegawa, K., and Fukada, S. 2013. Experiments and dynamic finite element analysis of a wire-rope rockfall protective fence. Rock Mechanics and Rock Engineering, **46**(5): 1183–1198. doi:10.1007/s00603-012-0340-0.

Vapnik, V. 2000. The nature of statistical learning theory. *In* 2nd edition. , New York.

Volkwein, A. 2005. Numerical simulation of flexible rockfall protection systems. *In* Computing in Civil Engineering (2005). American Society of Civil Engineers, Reston. pp. 1–11. doi:10.1061/40794(179)122.

Wyllie, D.C., and Mah, C. 2004. Rock slope engineering. *In* 4th edition. Taylor and Francis, London.

Xu, C., and Tannant, D.D. 2016. Discrete element modelling of steel wire mesh and rockbolt plate. *In* Proceedings of the 8th International Symposium on Ground Support in Mining and Underground Construction. Luleå University of Technology, Luleå, Sweden. p. 14.

Xu, C., and Tannant, D.D. 2018. Investigation of bolted steel mesh to support a sliding rock block using DEM. *In* CIM 2018 Convention. Vancouver, Canada. p. 9.

Xu, C., Tannant, D.D., and Zheng, W. 2019. Discrete element analysis of the influence of bolt pattern and spacing on the force-displacement response of bolted steel mesh. International Journal for Numerical and Analytical Methods in Geomechanics, **43**(12): 2106–2125. doi:10.1002/nag.2974.

Xu, H., Gentilini, C., Yu, Z., Qi, X., and Zhao, S. 2018. An energy allocation based design approach for flexible rockfall protection barriers. Engineering Structures, **173**: 831–852. doi:10.1016/j.engstruct.2018.07.018.

Zhang, K., Tan, P., Ma, G., and Cao, P. 2016. Modeling of the progressive failure of an overhang slope subject to differential weathering in Three Gorges Reservoir, China. Landslides, **13**(5): 1303–1313. doi:10.1007/s10346-015-0672-4.

Zhao, H. 2008. Slope reliability analysis using a support vector machine. Computers and Geotechnics, **35**(3): 459–467. doi:10.1016/j.compgeo.2007.08.002.